INERTIAL CONFINEMENT FUSION

Lawrence Livermore National Laboratory

ICF Quarterly Report January—March 1998, Volume 8, Number 2

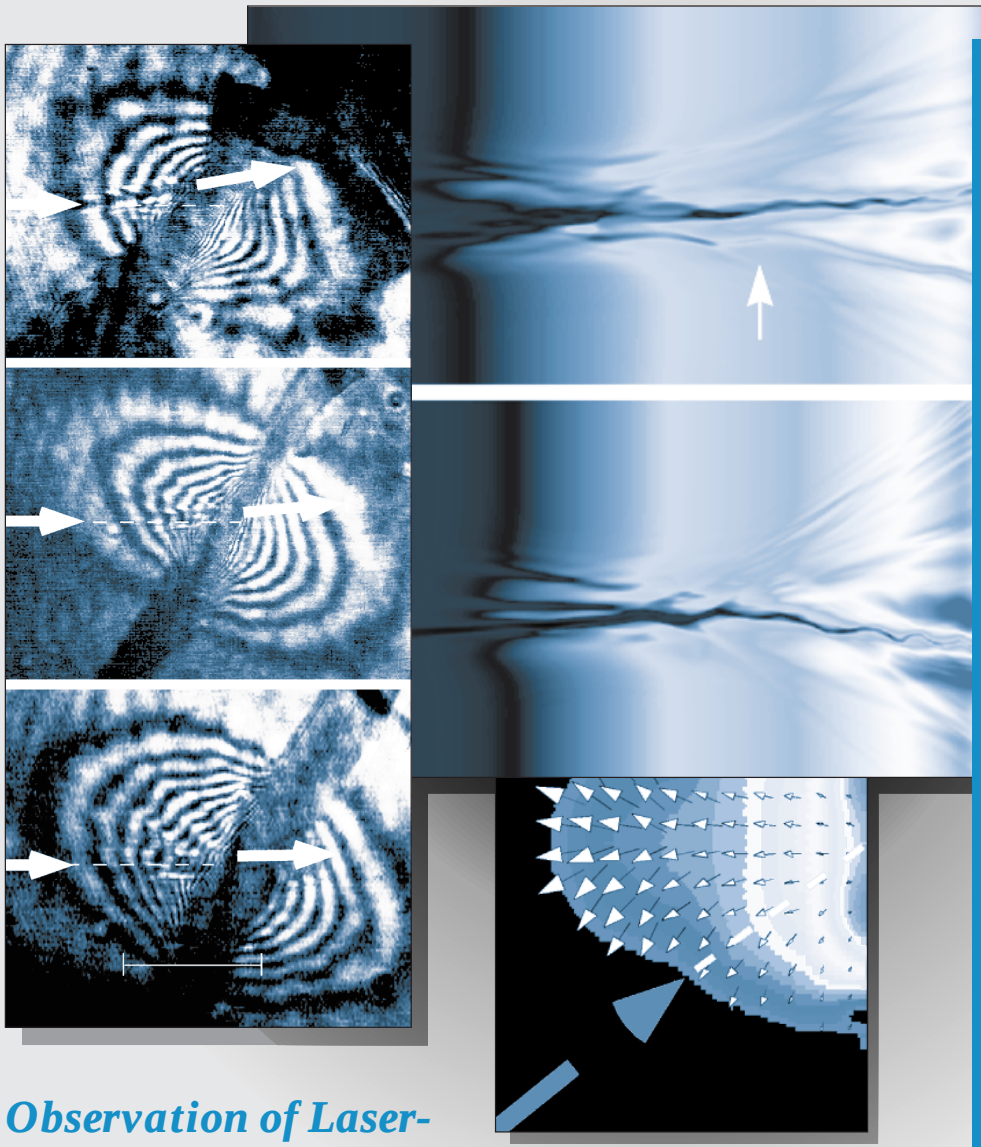

Observation of Laser-Beam Bending due to Transverse Plasma Flow

Special Issue: Laser-Plasma Interaction

UCRL-LR-105821-98-2

The Cover: A laser beam can be deflected substantially when plasma flows across it with a velocity approximately equal to the plasma sound speed. This has been demonstrated experimentally with interferograms of exploding foil plasmas in which the density channel formed by the laser is observed (three images at left). The target is oriented so that the plasma flows upward across the beam, causing an upward deflection; the amount of the deflection decreases as the laser intensity of the interaction beam decreases (from top to bottom in the three left-hand figures), as expected.

In order to substantially improve the understanding of laser propagation in plasmas, as much experimental data as possible is provided to the models, so both the density distribution and the flow velocity distribution (lower right image) are derived from the interferogram. The experiment is simulated using the F3D hydrodynamic code (top right images); comparison to the case where the flow is artificially turned off shows that the plasma flow deflects the beam by an amount equal to that seen in the experiment (10°). This experiment is described more fully in the article "Observation of Laser-Beam Bending due to Transverse Plasma Flow" on p. 46.

On the Web:

http://lasers.llnl.gov/lasers/pubs/icfq.html

UCRL-LR-105821-98-2
January–March 1998

Printed in the United States of America
Available from
National Technical Information Service
U.S. Department of Commerce
5285 Port Royal Road
Springfield, Virginia 22161
Price codes: printed copy A03, microfiche A01.

The *ICF Quarterly Report* is published four times each fiscal year by the Inertial Confinement Fusion / National Ignition Facility and High-Energy-Density Experimental Science (ICF / NIF / HEDES) Program at the Lawrence Livermore National Laboratory. The *ICF Quarterly Report* is also on the Web at http: / / lasers.llnl.gov / lasers / pubs / icfq.html. The journal summarizes selected current research achievements of the LLNL ICF / NIF / HEDES Program. The underlying theme for this program's research is defined within DOE's Defense Programs missions and goals. In support of these missions and goals, the ICF / NIF / HEDES Program advances research and technology development in major interrelated areas that include fusion target theory and design, target fabrication, target experiments, and laser and optical science and technology.

While in pursuit of its goal of demonstrating thermonuclear fusion ignition and energy gain in the laboratory, the ICF / NIF / HEDES Program provides research and development opportunities in fundamental high-energy-density physics and supports the necessary research base for the possible long-term application of inertial fusion energy for civilian power production. ICF technologies continue to have spin-off applications for additional government and industrial use. In addition to these topics, the *ICF Quarterly Report* covers non-ICF funded, but related, laser research and development and associated applications. We also provide a short summary of the quarterly activities within Nova laser operations, Beamlet laser operations, and the NIF laser design and construction.

LLNL's ICF / NIF / HEDES Program falls within DOE's national ICF Program, which includes the Nova and Beamlet (LLNL), OMEGA (University of Rochester Laboratory for Laser Energetics), Nike (Naval Research Laboratory), and Trident (Los Alamos National Laboratory) laser facilities. The Particle Beam Fusion Accelerator and Saturn pulsed-power facilities are at Sandia National Laboratories. General Atomics, Inc., develops and provides many of the targets for the above experimental facilities. Many of the *Quarterly Report* articles are co-authored with our colleagues from these other ICF institutions.

Questions and comments relating to the technical content of the journal should be addressed to the ICF / NIF / HEDES Program Office, Lawrence Livermore National Laboratory, P.O. Box 808, Livermore, CA, 94551.

Work performed under the auspices of the U.S. Department of Energy by Lawrence Livermore National Laboratory under Contract W–7405–Eng–48.

INERTIAL CONFINEMENT FUSION

ICF Quarterly Report *January–March 1998, Volume 8, Number 2*

In this issue:

FOREWORD

The coupling of laser light with plasmas is one of the key physics issues for the use of high-power lasers for inertial fusion, high-energy-density physics, and scientific stockpile stewardship. The coupling physics is extremely rich and challenging, particularly in the large plasmas to be accessed on the National Ignition Facility (NIF). The coupling mechanisms span the gamut from classical inverse bremsstrahlung absorption to a variety of nonlinear optical processes. These include stimulated Raman scattering (SRS) from electron plasma waves, stimulated Brillouin scattering (SBS) from ion sound waves, resonant decay into electron plasma and ion sound waves, and laser beam filamentation. These processes depend on laser intensity and produce effects such as changes in the efficiency and location of the energy deposition or generation of a component of very energetic electrons, which can preheat capsules. Coupling physics issues have an extremely high leverage. The coupling models are clearly very important ingredients for detailed calculations of laser-irradiated target behavior. Improved understanding and models enable a more efficient use of laser facilities, which becomes even more important as these facilities become larger and more expensive. Advances in the understanding also allow a more timely and cost-effective identification of new applications of high-power lasers, such as for generation of high-temperature hohlraums and compact x-ray sources, or for discovery of advanced fusion schemes. Finally, the interaction of intense electromagnetic waves with ionized media is a fundamental topic of interest to numerous areas of applied science and is an excellent test bed for advancing plasma science and computational modeling of complex phenomena.

This issue of the *ICF Quarterly Report* is dedicated to laser–plasma interactions. The eight articles present a cross section of the broad progress in understanding the key interaction issues, such as laser beam bending, spraying, and scattering, as well as scaling the Nova results to NIF. Each of these articles represents a very productive and timely collaboration with other parts of the Lawrence Livermore National Laboratory (A Division, V Division, the Magnetic Fusion Program, and the Institute for Laser Science and Applications) or with other institutions (such as the Naval Research Laboratory, the University of Rochester's Laboratory for Laser Energetics, Centre d'Etudes Atomique at Bruyeres, Laboratoire pour Utilization des Lasers Intenses, University of California at Los Angeles, University of California at Davis, and INRS Energie-Materiaux). Such strong collaborations with the broader laser–plasma community are extremely important given the complexity of laser–plasma interactions and their importance to timely success with the NIF. Other recent progress in laser–matter interactions ranges from the experimental demonstration of strong instability reduction by laser beam smoothing to characterization of ultraintense interactions for fast ignition and laser radiography. This progress will be covered in future *Quarterly* issues.

Four of the articles in this issue discuss advances in the diagnosis of laser plasmas and in the characterization of the interaction processes. In "Thomson Scattering from Inertial Confinement Fusion Plasmas" (p. 59), a direct and accurate diagnostic is used to measure the electron and ion temperatures. These measurements provide an important benchmark for hydrodynamic calculations using LASNEX. An important mechanism for limiting stimulated Raman scattering is characterized in "Observation of the Nonlinear Saturation of Langmuir Waves Driven by Ponderomotive Force in a Large-Scale Plasma" (p. 73). In Nova experiments using crossed laser beams, a nonlinear saturation of driven Langmuir waves is demonstrated. These observations are consistent with saturation by the excitation of secondary instabilities involving ion waves, an effect that accounts for an observed dependence of the SRS on ion wave damping.

The next two experimental articles discuss effects that impact radiation symmetry in hohlraums: energy transfer between crossing laser beams and nonlinear beam

bending. In "Observation of Energy Transfer between Identical-Frequency Laser Beams in a Flowing Plasma" (p. 69), energy transfer between crossing laser beams with the same frequency is shown to occur when the plasma flow velocity is nearly sonic. This energy transfer occurs via an ion wave that becomes resonant due to a Doppler-shift in frequency by the plasma flow. In "Observation of Laser-Beam Bending due to Transverse Plasma Flow" (p. 46), the nonlinear beam bending is directly observed via interferometric measurements of the laser-generated plasma channel. The bending is shown to be intensity-dependent and to occur where the transverse flow is nearly sonic, in agreement with predictions. The detailed measurements are used to benchmark F3D, a 3D code for light wave propagation in plasma.

The other four articles describe advances in the theory and simulation of laser–plasma coupling. In two articles, techniques to control laser-driven instabilities are discussed. In "Reduction of Laser Self-Focusing in Plasma by Polarization Smoothing" (p. 83), a significant reduction in the filamentation of an intense, speckled laser beam by polarization smoothing is demonstrated in F3D simulations. Even greater reduction is found when this smoothing is combined with temporal smoothing using smoothing by spectral dispersion. A process to reduce SBS is discussed in "Suppression of Stimulated Brillouin Scattering by Mode Coupling Induced with Seeded Ion Waves" (p. 51). Particle simulations and theory are used to show that the mode coupling of a Brillouin-generated ion wave with a secondary, obliquely propagating ion wave can reduce the backscatter. These calculations are consistent with recent experiments.

The last two laser–plasma coupling articles report advances in the models for laser–plasma interactions. The first simulations of stimulated scattering to allow for ion–ion collisions are discussed in "Hybrid Particle-in-Cell Simulations of Stimulated Brillouin Scattering Including Ion–Ion Collisions" (p. 78). It is shown that these collisions can have an important effect on SBS in high-Z plasmas, such as those near the wall of a laser-irradiated hohlraum. Finally, in "Kinetic Theory of Electron-Plasma and Ion-Acoustic Waves in Nonuniformly Heated Laser Plasmas" (p. 41), it is shown that modifications of the electron velocity distributions by heat transport and non-Maxwellian inverse bremsstrahlung absorption can strongly impact the behavior of laser-driven instabilities in underdense plasmas illuminated by structured laser beams. A detailed exposition of the changes in the behavior of plasma modes is given, and the implications of this work to the onset of SRS in underdense plasmas, the saturation of SRS via the Langmuir decay instability, and its natural anticorrelation with SBS are examined for random-phase-plate beams.

William Kruer
Scientific Editor

KINETIC THEORY OF ELECTRON-PLASMA AND ION-ACOUSTIC WAVES IN NONUNIFORMLY HEATED LASER PLASMAS

*B. B. Afeyan** *R. P. J. Town*††*

A. E. Chou† *W. L. Kruer*

*J. P. Matt***

Introduction

When a high-intensity laser illuminates a plasma, large-scale nonuniformities in the laser spatial profile will cause differential heating in the plasma giving rise to steep temperature gradients, nonlocal heat transport, heat flux inhibition,[1] and non-Maxwellian inverse bremsstrahlung heating especially in laser hot spots.[2,3] Laser-spatial-profile nonuniformities can contribute to the dephasing of three-wave-parametric instabilities in the usual way.[4] However, the effect of these nonuniformities on the *background plasma* and kinetic characteristics of waves, which then affect instabilities in a fundamental way, has in the past been largely ignored.[5] We begin to address that in this article by examining the behavior of plasma waves using velocity distribution functions (VDFs) obtained from Fokker–Planck (FP) simulations of nonuniformly heated, large-scale plasmas. Laser speckle patterns are taken into account, the resulting nonuniform heating is simulated, and their consequences on electron-plasma wave (EPW) and ion-acoustic wave (IAW) properties are calculated by solving the appropriate kinetic dispersion relations. Significant changes in the properties of these waves are uncovered that shed light on some key puzzles in recent laser–plasma interaction experiments. One concerns the stimulated Raman scattering instability (SRS), which involves light scattering off EPWs.[6] SRS is observed from densities that are too low were the VDFs to have been Maxwellian at the measured temperature.[7] Similarly, instabilities involving ion waves[8] seem to be suppressed at high densities in the strong ion-wave damping limit, and stimulated Brillouin scattering (SBS) is observed to be anticorrelated with SRS.[9] In addition, high-Z plasmas have been observed to exhibit SRS levels that depend strongly on ion wave characteristics.[10] In those experiments, the potential for Langmuir decay instability (LDI) to saturate SRS was brought into question and resolved by invoking reduced damping rates of EPWs via the mechanism discussed in this article.[10,5] Moreover, crossed beam SBS and SRS gains have been shown to be anomalously low with randomly displaced frequency peaks.[11] We will show that this is to be expected whenever the instabilities occur in laser hot spots where the frequencies and damping rates of the waves are modified due to non-Maxwellian VDF effects.

Description of Simulations

The use of random phase plates (RPPs) was pioneered over a decade ago in laser–plasma interaction experiments,[12] and they have been used ever since. RPPs are meant to replace unpredictable and unwarranted large-scale variations in laser intensity with a statistically well defined spiky interference or speckle pattern.[13] Given any such nonuniform laser illumination profile, it is important to obtain the resulting electron VDFs from an FP calculation as the plasma is heated to inertial confinement fusion (ICF) relevant temperatures of 2 or 3 keV. We have done this with both the FPI[3] and SPARK[14] codes in large 1D simulations and smaller 2D boxes for comparison. We will concentrate on the set of comprehensive 1D runs using FPI in this article and report on 2D results elsewhere. These simulations used a lateral cut across a 0.35-μm-wavelength RPP beam, which was 211-μm wide. The plasma had two side (or "moat") regions of the same width as the beam, all held at a density of tenth critical. The ionization states were low to moderate ($\bar{Z} = \langle Z^2 \rangle / \langle Z \rangle = 5, 10, 20$). The angular dependence of the VDF is expanded in Legendre polynomials in FPI up to order 3. Inspection of the values showed that the $|f_2| / f_0$ ratio was below 1 in all regions where f_0 was not vanishingly small. Only f_0 is used in the present

*University of California, Davis-Livermore, Livermore, CA
†University of California, Los Angeles, Los Angeles, CA
**INRS Energie-Materiaux, Varennes, Quebec, Canada
††LLE, University of Rochester, Rochester, NY

analysis. Beyond each edge of the 211-μm-wide beam, the intensity was allowed to fall off linearly over 73 μm, and then there was a 139-μm unheated region before reaching the simulation box boundaries which were maintained at the initial temperature of 300 eV. These large, unheated regions essentially eliminate the effects of boundaries on the transport physics within the beam because hot electrons generated in hot spots are quickly transported into the large cooler regions surrounding the beam before being absorbed at the boundaries and reemitted with an equivalent flux at the prescribed wall temperature.

Simulation Results and Interpretation

To show the resulting VDFs, we resort to the shorthand of a set of super-Gaussian functions, which were first introduced by Dum in a number of different plasma physics contexts,[15] and that were found to be ideal for the description of quasi-steady-state, uniform-intensity-illumination, laser–plasma-heating, and transport simulations by Matte using his FPI code.[2,3] These Dum–Langdon–Matte (DLM) VDFs may be written in the form

$$f_e = C(n)\frac{N_{e_0}}{v_e^3}\exp-\left(\frac{|v|}{\alpha_e v_e}\right)^n \qquad (1)$$

where $v_e^2 = T_e/m_e$ and the constant

$$\alpha_e = \left(\frac{3\Gamma(3/n)}{\Gamma(5/n)}\right)^{1/2} \qquad (2)$$

is chosen to ensure the proper definition of temperature in terms of the second moment of the 3D distribution function:

$$\langle v^2\rangle = 3v_{th}^2 \quad . \qquad (3)$$

The normalization prefactor is

$$C(n) = \left(\frac{1}{4\pi\alpha_e^3}\right)\left(\frac{n}{\Gamma(3/n)}\right), \qquad (4)$$

which ensures that the zeroth moment of the 3D distribution function is the density N_{e0}. In the standard theory of non-Maxwellian inverse bremsstrahlung heating,[2,3] as the laser intensity is increased, the exponent n increases from the Maxwellian limit of $n = 2$ to the limit where electron–electron collisions are entirely negligible, $n = 5$. These distribution functions will have increasingly more flattened cores and depleted tails. For uniform laser illumination cases, Matte[3] has obtained the connection between the exponent n and parameters that characterize the laser–plasma system. With the laser intensity I defined in units of 10^{15} W/cm^2, laser wavelength λ_0 in units of 0.35 μm, and the electron temperature T_e in keV, the conversion is

$$\bar{Z}I_{15,\mathrm{W/cm^2}}\lambda_0^2, 0.35\,\mu\mathrm{m}/T_{e,\mathrm{keV}} = 44.29\left[(n-2)/(5-n)\right]^{1.381}. \qquad (5)$$

Because this result neglects the nonlocal heat transport that accompanies spatially nonuniform non-Maxwellian inverse bremsstrahlung heating, we would expect the Matte formula to slightly overestimate the proper DLM exponent n at the very centers of the hot spots and to severely underestimate the non-Maxwellianness everywhere else in the illuminated region. New FP simulations using RPP beam patterns were performed precisely to overcome these limitations, which a direct reliance on DLMs and the Matte formula would cause.[16,5] The resulting inferred DLM exponents n from the Ca simulations and those predicted by Matte's formula are shown in Figure 1 together with the laser intensity distribution and the FP-simulation-obtained temperature profile normalized to the average temperature in the illuminated region. Figure 2 shows the damping rate of EPWs in plasmas, whose e^- VDFs are given by the FP codes

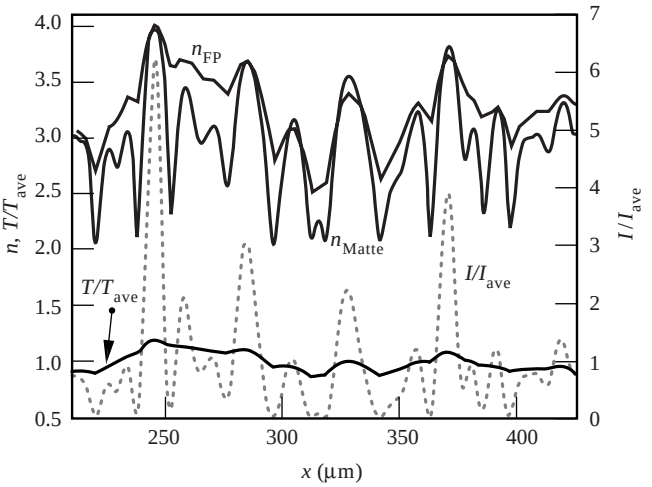

FIGURE 1. The DLM exponent n and the temperature (normalized to the average temperature in the illuminated region, T_{ave} = 2.26 keV) extracted from FPI simulations of a Ca plasma at a tenth critical density vs lateral position x in an $f/4$ RPP laser beam whose intensity distribution is plotted as I/I_{ave}, where $I_{ave} = 2\times10^{15}$ W/cm^2. Also shown are DLM exponents inferred from the Matte formula, which underestimates the degree of non-Maxwellianness everywhere except at the centers of the hot spots. (50-00-0698-1408pb01)

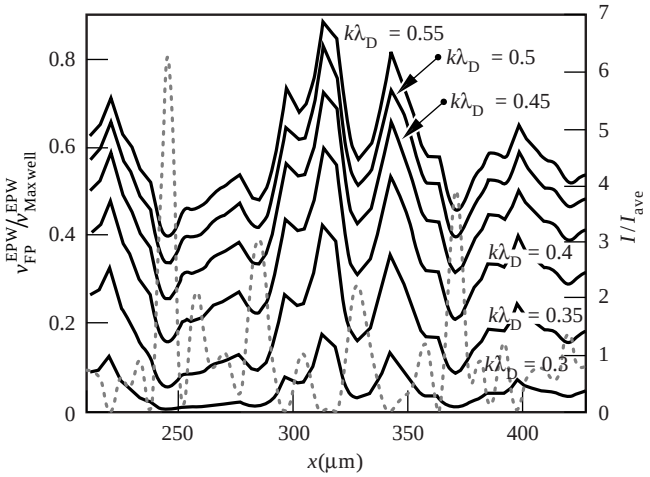

FIGURE 2. EPW damping rates which are solutions of the kinetic dispersion relation using the distribution function obtained from Fokker–Planck simulations, normalized to Maxwellian plasma damping rates at the same average temperature vs lateral position x for $k\lambda_{De}$ = 0.35 – 0.55, in steps of 0.05. (50-00-0698-1409pb01)

directly, normalized to that of EPWs in a Maxwellian plasma at the same density and at the same average temperature (inside the illuminated region). The electron susceptibility is given by[6]

$$\chi_e = \frac{\omega_{p_e}^2}{N_{e_0} k^2 \bar{f}_e} \int \frac{\mathbf{k}\cdot\partial f_e/\partial v}{\omega - \mathbf{k}\cdot\mathbf{v}}\, dv \tag{6}$$

$$= \frac{1}{A}\frac{1}{k^2\lambda_{De}^2}\left[1+\zeta_0 I(\zeta_0)\right] , \tag{7}$$

where

$$\zeta_0 = \left(\omega/\omega_{p_e}\right)\Big/\left(k\lambda_{De}\right) , \tag{8}$$

$$A = N_{e_0}\Big/\left(2\pi\bar{f}_e\right) . \tag{9}$$

N_{e_0} is the 3D average of the e⁻ VDF, and $\bar{f}_e$ is its 1D average. The Hilbert transform of the normalized VDF is defined via the integral

$$I(\zeta_0) = \int \frac{d\zeta\, f_e(\zeta)}{\left(\zeta-\zeta_0\right)/\bar{f}_e} . \tag{10}$$

Solving $1 + \chi_e = 0$ gives us the complex frequencies of EPWs. The resulting damping rates for a Ca plasma at an average temperature of 2.26 keV are shown in Figure 2. Note the order of magnitude reduction in EPW damping rates compared to those in a Maxwellian plasma at the values of $k\lambda_{De} \approx 0.35$ that typically arise in experiments.

The Effects of Modified Distribution Functions on IAWs and SBS

The impact of non-Maxwellian e⁻ VDFs on IAWs can be seen by noting the factor A which renormalizes $k^2\lambda_{De}^2$ in Eq. (7). It boosts the effective electron temperature that enters the definition of the frequency of an IAW: $\omega_{IAW}^2 = Ac_s^2k^2$. The reduced number of slow electrons available to shield the ions causes this IAW frequency increase over that of a Maxwellian plasma. For DLMs, we have calculated this boosting factor analytically to be

$$A(n) = \frac{3\left[\Gamma\left(3/n\right)\right]^2}{\Gamma\left(1/n\right)\Gamma\left(5/n\right)} . \tag{11}$$

In Figure 3 we plot the actual A factor calculated using the VDFs obtained from the FP simulations multiplied by the ratio of the spatially varying temperature, obtained from the FP runs, divided by the average temperature vs lateral position inside the RPP beam for CH, Ne, and Ca plasmas at one-tenth critical density and an average laser intensity of 2×10^{15} W/cm^2. RMS fluctuations exceeding 20% are obtained via this ion-acoustic frequency spatial modulation effect due to spatially nonuniform and non-Maxwellian inverse bremsstrahlung heating. Such modulations can help explain the recent crossed beam SBS results of Kirkwood et al.,[11] where anomalously low

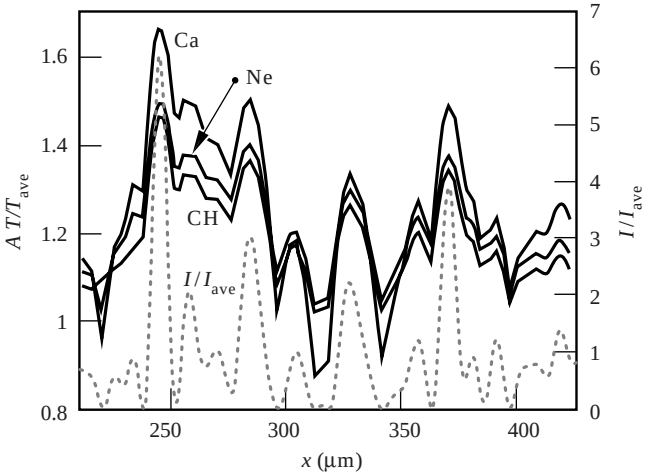

FIGURE 3. The ratio of the sound speed squared using the distribution function from Fokker–Planck simulations to that of a Maxwellian plasma at the same average temperature vs lateral position x for CH, Ne, and Ca plasmas at a tenth critical density and with an average temperature of 2.26 keV. This is the A factor which boosts the IAW temperature with respect to the energy temperature, multiplied by the spatially varying temperature normalized to the average temperature: $A\,T_e(x)/T_{ave}$. Typically, 20% or more RMS spatial variation in sound speed can be attained due to this kinetic effect. (50-00-0698-1410pb01)

crossed beam gains were found with seemingly random peaks in the frequency-tuning curves in the strongly damped IAW limit. Details of the interplay between this kinetic effect and that of velocity fluctuations, which conspire to detune the instability, will be given elsewhere.[17] Because the two effects are complementary, this kinetic frequency shift reduces the size of velocity fluctuations required to produce an order of magnitude lower SBS gain than in a uniform plasma illuminated by a uniform laser beam to around 10%.

The Effects of Modified Distribution Functions on EPWs and SRS

To show the effects of EPW damping reduction on parametric instabilities (PIs) driven by RPP laser beams, we solved the kinetic dispersion relation of SRS[18] using the FP-generated VDFs. The results are shown in Figure 4 where we plot the ratio of SRS spatial gain rate κ_{FP}, using VDFs obtained via FP simulations, to those of a Maxwellian at the same temperature $\kappa_{Maxwell}$ for the Ca and Ne plasma cases. Note that more than an order-of-magnitude increase in SRS gain rates is obtained inside hot spots even with nonlocal heat transport, which tends to smooth out the differences between the high-energy portions of the e^- VDFs at different positions. In any case, the e^- VDFs remain highly non-Maxwellian. These large gain-enhancement factors allow the occurrence of SRS at low densities and at high temperatures, which could simply not occur in a Maxwellian plasma. Elsewhere, non-Maxwellian VDFs will turn otherwise convective SRS into absolute instabilities, which would require nonlinear mechanisms to reach saturation.

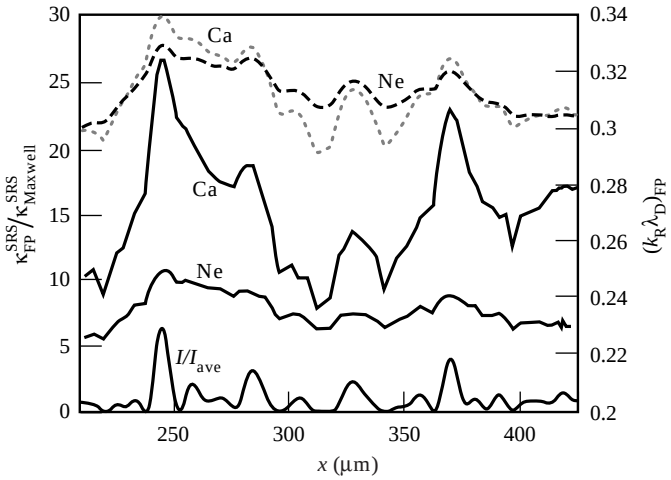

FIGURE 4. The spatial gain coefficient for stimulated Raman backscattering, using the distribution functions generated by Fokker–Planck simulations, normalized to that of a Maxwellian plasma at the same temperature vs lateral position x for Ca ($\bar{Z}$ = 20), and Ne ($\bar{Z}$ = 10), plasmas at a tenth critical density and with an average temperature of 2.26 keV. Also plotted are the real frequencies of the most unstable modes (dotted and dashed curves) and the intensity profile of the RPP beam. Order-of-magnitude increases in gain rates over Maxwellian plasmas are obtained. (50-00-0698-1411pb01)

Conclusion

We have shown in this article that an order-of-magnitude or more increase in SRS gain rates may be expected from low-density and high-temperature plasmas whenever high-intensity RPP beams nonuniformly heat a plasma. This suggests that Raman can grow at densities lower than expected and at temperatures higher than expected by relying on Maxwellian assumptions. We have also noted that parametric instabilities that rely on the properties of IAWs, such as SBS, LDI and EDI, will be significantly detuned in the strong IAW damping limit because IAW frequencies were shown to be spatially modulated by 20% or more over length scales that are short compared to the interaction lengths required for significant gain.[17] It follows that in the presence of non-Maxwellian VDFs SRS and SBS will be highly collimated and their reflectivities naturally anti-correlated for two reasons. First, the reduction of EPW damping increases SRS gain while simultaneously detuning SBS in the strong IAW damping limit and second, in that same limit, LDI and EDI gains are reduced to the same extent as SBS. But since the former are meant to saturate SRS, their inefficiency leads to additional unhindered SRS growth. We plan to report on extensions of this work next by using filamentation-generated intensity profiles[19] and not just RPP ones. We have seen that in the former case, the axial extent of hot spots will be so shortened that dephasing will be substantial even for backscattering instabilities. This suggests that filamentation could potentially suppress SBS backscatter (SBBS) especially in the strong IAW damping limit, making SBBS more likely at lower densities (where hot-spot lengths would be long) than at higher densities where filamentation would be rampant and the correlation lengths of hot spots would be much shorter, making the concomitant modulations of the frequency of IAWs ever more effective in suppressing SBBS and LDI.

Acknowledgments

We gratefully acknowledge discussions with D. Montgomery, J. Fernandez, J. Moody, S. Glenzer, R. Kirkwood, T. Johnston, and V. Tikhonchuk. The work of R. P. J. Town was supported by the U. S. Department of Energy Office of Inertial Confinement Fusion under Cooperative Agreement No. DE-FC03-92SF19460 and the University of Rochester.

Notes and References

1. A. R. Bell et al., *Phys. Rev. Lett.* **46**, 243, (1981); P. Mora and H. Yahi, *Phys. Rev.* **A26**, 2259 (1982); J. A. Albritton, *Phys. Rev. Lett.* **50**, 2078 (1983) and **57**, 1887 (1986).
2. A. B. Langdon, *Phys. Rev. Lett.* **44**, 575 (1980); R. D. Jones, and K. Lee, *Phys. Fluids* **25**, 2307 (1982); P. Alaterre, J.-P. Matte, and M. Lamoureux, *Phys. Rev.*, **A34**, 1578 (1986); J. M. Liu et al., *Phys. Plasmas* **1**, 3570 (1994).
3. J. P. Matte et al., *Plasma Phys. Cont. Fusion* **30**, 1665 (1988).
4. K. Nishikawa and C. S. Liu, *Advances in Plasma Physics*, Vol. 16, (A. Simon and W. Thompson, eds.) p. 3-81, 1976.
5. B. B. Afeyan, A. E. Chou, and W. L. Kruer, *Effects of Non-Maxwellian Velocity Distribution Functions on Parametric Instabilities*, *ICF Quarterly Report* **7**(2), 78, Lawrence Livermore National Laboratory, Livermore, CA, UCRL-LR-105821-97-2 (1997), and to be submitted to *Phys. Rev. E.*
6. W. L. Kruer, *The Physics of Laser Plasma Interactions*, Frontiers in Physics series, number 73. (Addison-Wesley Publishing Company, 1988).
7. D. S. Montgomery et al., *Phys. Plasmas* **3**, 1728, (1996).
8. Such as stimulated Brillouin scattering (SBS), which involves light scattering off IAWs; the Langmuir decay instability, which involves an EPW decaying into another EPW and an IAW; and the electromagnetic decay instability, which involves an EPW decaying into an electromagnetic wave and an IAW.
9. D. S. Montgomery et al., *Phys. Plasmas* **5**, 1973 (1998).
10. R. K. Kirkwood et al., *Phys. Rev. Lett.* **77**, 2706, (1996); J.C. Fernandez et al., *ibid* 2702.
11. R. K. Kirkwood et al., *Phys. Rev. Lett.* **76**, 2065, (1996).
12. Y. Kato et al., *Phys. Rev. Lett.* **5**, 1057 (1984).
13. S. M. Dixit et al., *Appl. Optics* **32**, 2543 (1993).
14. E. M. Epperlein, *Lasers and Particle Beams* **12**, 257, (1994).
15. C. T. Dum, *Phys. Fluids* **21**, 945 and 956 (1978).
16. C. Rousseaux et al., *Phys. Fluids* **B5**, 920 (1993) ; V. Yu. Bychenkov, W. Rozmus, and V. T. Tickonchuk, *Phys. Plasmas* **4**, 1481 (1997); J. Zheng, C. X. Yu, and Z. J. Zheng, *Phys. Plasmas* **4**, 2736 (1997).
17. B. B. Afeyan et al., "Effects of Fluctuations in Ambient Flow and in the Laser Intensity on the Stimulated Brillouin Scattering Instablilitiy," *Bull. Amer. Phys. Soc.*, 7R.08, Nov. 1995 and manuscript in preparation.
18. J. F. Drake et al., *Phys. Fluids* **17**, 778 (1974).
19. A. J. Schmitt and B. B. Afeyan, *Phys. Plasmas*, **5**, 503, 1998.

OBSERVATION OF LASER-BEAM BENDING DUE TO TRANSVERSE PLASMA FLOW

P. E. Young *E. A. Williams*

C. H. Still *R. L. Berger*

D. E. Hinkel *K. G. Estabrook*

W. L. Kruer

Introduction

The propagation of intense laser pulses through fully ionized plasmas can be affected by a number of processes that can be linear, such as refraction due to transverse density gradients, or nonlinear in the case of the filamentation instability. While laser-beam propagation in the direction normal to the density gradient and plasma flow have been studied thoroughly, transverse flow introduces new considerations and can, for example, influence the growth rate of filamentation [1]. This is an important consideration for hohlraum targets used in inertial confinement fusion applications where plasma flowing across the beam near the entrance hole can steer the beam. As a result, the symmetry of the intended x-ray drive can change because the position of the laser spot on the hohlraum wall is moved. Transverse flow steers the beam when the laser is sufficiently intense that the ponderomotive force causes the plasma to pile up against the beam, which produces a density gradient that refracts the beam towards the downstream direction. This effect is particularly strong when the transverse flow velocity equals the sound speed of the plasma.[1,2] Although some evidence of this effect has recently been reported,[3] quantitative comparison to theoretical predictions requires a well characterized background plasma and knowledge of the laser beam path through the plasma.

In this article, we describe the results of an experiment in which we interferometrically observe the density channel produced by an intense laser beam propagating through a preformed plasma. We observe beam bending in the presence of transverse plasma flow that increases as the laser intensity is increased, which rules out refractive effects due to the unperturbed density profile. An important point is that the beam bending occurs at a very low density ($\sim 0.05 n_c$) where the filamentation threshold is not exceeded. For a laser intensity of 1.5×10^{15} W/cm^2, we observe beam deflections of 10 degrees, which is in quantitative agreement with the calculations of the F3D hydrodynamic code.[4] The code uses the experimentally measured density and flow velocity profiles and a laser electric field reconstructed from the measured near-field phase profile of the experimental laser beam.

Some simple estimates illustrate the physics of beam bending. Consider a beam propagating through a flowing plasma with electron density n_e. Its ponderomotive pressure creates a density depression of magnitude $\Delta n / n \approx (v_o / v_e)^2 / (1 - M^2)$, where v_o is the electron quiver velocity in the laser field, v_e is the electron thermal velocity, and M is the Mach number of the flow component transverse to the direction of propagation. The density perturbation is swept downstream of the intensity maximum so that the light sees a refracting gradient $\nabla_\perp \Delta n \sim (n_e / L_T)(v_o / v_e)^2 (1 - M^2)^{-1}$, where L_T is the characteristic transverse dimension of the laser beam. The light is deflected by ray optics through an angle, θ, given by

$$\theta \approx (1/2n_c)\int \nabla_\perp \Delta n \, dz$$
$$= (1/2)(n_e / n_c)(v_o / v_e)^2 L_T^{-1} \int dz \, [1 - M(z)^2]^{-1}. \quad (1)$$

As $M \Rightarrow 1$, the simple linear estimate for Δn, above, fails. Within some range, ΔM of the sonic point at M = 1, the density perturbation saturates, either nonlinearly ($\Delta M \sim v_o / v_e$) (Ref. 5) or from finite ion acoustic damping ($\Delta M \sim \nu_{ia} / \omega_{ia}$, where ν_{ia} / ω_{ia} is the ion acoustic damping decrement).[6,7]

Independent of the saturation mechanism and of the magnitude of ΔM ($<< 1$), we can estimate the integral in Eq. 1 by $L_v / 2$, where L_v is the scalelength of the transverse velocity variation at the sonic point, giving

$$\theta \approx (1/4)\,(n_e / n_c)(v_o / v_e)^2 (L_v / L_T). \quad (2)$$

For a beam with internal structure, L_T can be expected to be characteristic of the typical hot spot

dimensions, ~$f\lambda$, rather than the total beam width. In this experiment, the beam phase was measured, making quantitative comparison with numerical calculation well motivated.

Note that the mechanism for beam bending is independent of filamentation. With increasing intensity, however, existing hot spots in the laser beam will be intensified by self-focusing. One anticipates from Eq. 2 that the increasing intensity and reduced lateral dimension of self-focused hot spots should increase beam bending. Strong filamentation, however, can be expected to cause beam breakup and the lack of identifiable channels.

An important point is that in this experiment, the observed beam bending occurs at a very low density before filamentation can occur, so filamentation is decoupled from the beam bending process. Filamentation results in the spraying of the beam and produces the termination of the channel near the peak of the plasma density, as observed by the interferometer. The imaginary wave number for ponderomotive filamentation is given by:[8]

$$k_I = (k_R / 2k_0)\,(1/2)[(\omega_0{}^2 / c^2)(n_e / n_c)\,(v_0 / v_e)^2 - k_R{}^2]^{1/2}, \quad (3)$$

where k_R is the transverse size of the filaments. Since the beam width is only 20 μm, the filaments must be less than 10 μm in size to grow. For exponential growth, $2k_I L \cong 1$. For the conditions $k_R / k_0 = 5$, $n / n_c = 0.05$, $T_{keV} = 0.5$, $L_\mu = 50$, and $\lambda_\mu = 1.064$, we find that $I_p = 4.5 \times 10^{15}$ W/cm^2 is required for exponential growth, which is three times the vacuum intensity. This analysis neglects the lowering of the background density in the beam channel, which would further raise the threshold intensity. In fact, both the experiments and the simulations show a well-defined channel all the way to the peak of the density profile (~$0.3n_c$), indicating that filamentation is not important at the lower densities.

Experimental Description

The present experiment was conducted using the Janus laser at Lawrence Livermore National Laboratory where we have developed a test bed for studying the propagation of moderately intense laser pulses through well-characterized underdense plasmas.[9] A 1.064-μm wavelength, 100-ps full-width at half-maximum (FWHM) Gaussian pulse interacted with an underdense plasma formed by the irradiation of a 0.35-μm-thick parylene [$(CH)_n$] foil by a 1-ns, 0.532-μm wavelength, 400-μm-diam, 2×10^{13} W/cm^2 laser pulse. Both a line focus and a circular focus were used for the interaction beam at various points in the experiment. A line focus (20 μm × 400 μm, peak intensity = 1.5×10^{15} W/cm^2) was used because the long path length through the channel makes the observed phase change due to the density depression easy to see.[10] To observe the behavior of the channel at higher intensities, we used a circular focus to achieve a peak intensity of 5×10^{16} W/cm^2. The best focus of the interaction beam in all cases is located at the target plane, and its vacuum properties[10] are constant as the laser intensity is varied by changing the amplifier gain, which changes the laser energy. Varying the relative timing between the plasma formation and interaction pulses (1.5- to 2.5-ns delay from the end of the plasma-forming pulse) determined the peak density (0.25 to $0.1n_c$) seen by the interaction pulse. The background density profile was measured using a folded-wave interferometer. The 50-ps, 0.35-μm wavelength interferometer probe pulse arrived at the target at the same time as the peak of the 100-ps interaction pulse.

To introduce a component of the plasma flow that is transverse to the propagation direction of the interaction beam, the target foils are tilted at angles up to 45 degrees. Since the plasma flow is normal to the target surface, the target angle determines the transverse flow velocity seen by the interaction pulse.

Results and Analysis

The main experimental results are summarized in Figure 1. At the highest intensity (for a line focus), we see obvious beam bending (~10 degrees) at the outer edge of the plasma where the density is low (~$0.05n_c$), but the flow velocity is high (~1×10^8 cm/s) compared to the sound speed, c_s (~3×10^7 cm/s). The bending is localized, and the channel stays well-defined up to the peak plasma density (~$0.3n_c$), after which it disappears; this is because of beam breakup and spreading due to filamentation.[10,11]

As we vary the incident laser intensity, the amount of bending becomes substantially less (see Figure 1) until there is a 1 degree deflection for an intensity of 2×10^{14} W/cm^2, clearly showing that this is an intensity-dependent effect and not due to linear refraction in the inhomogeneous plasma distribution. We observe a similar reduction in bending angle as we decrease the target angle, as expected.

The deflection predicted by the simple analytic model of Eq. 2 agrees well with that observed in the experiment. For the line focus, we take $n / n_c \cong 0.05$, $I = 1 \times 10^{15}$ W/cm^2, $T_e = 500$ eV, $L_v \cong 200$ μm, and $L_T \cong 10$ μm, and find $\theta \cong 13^o$, close to what is observed in the experiment. Of course, quantitative calculations need to account for detailed beam structure, laser-beam filamentation, and various 3D effects. For example, when a circular focus is used to obtain a very high intensity (5×10^{16} W/cm^2), no beam deflection is detected. This result is in agreement with the nonlinear model of Rose,[6,12] who has discussed a regime in which the plasma can simply flow around a small beam, an effect which clearly decreases the deflection.

We will next show experimentally that the location of the beam bending occurs where the transverse flow

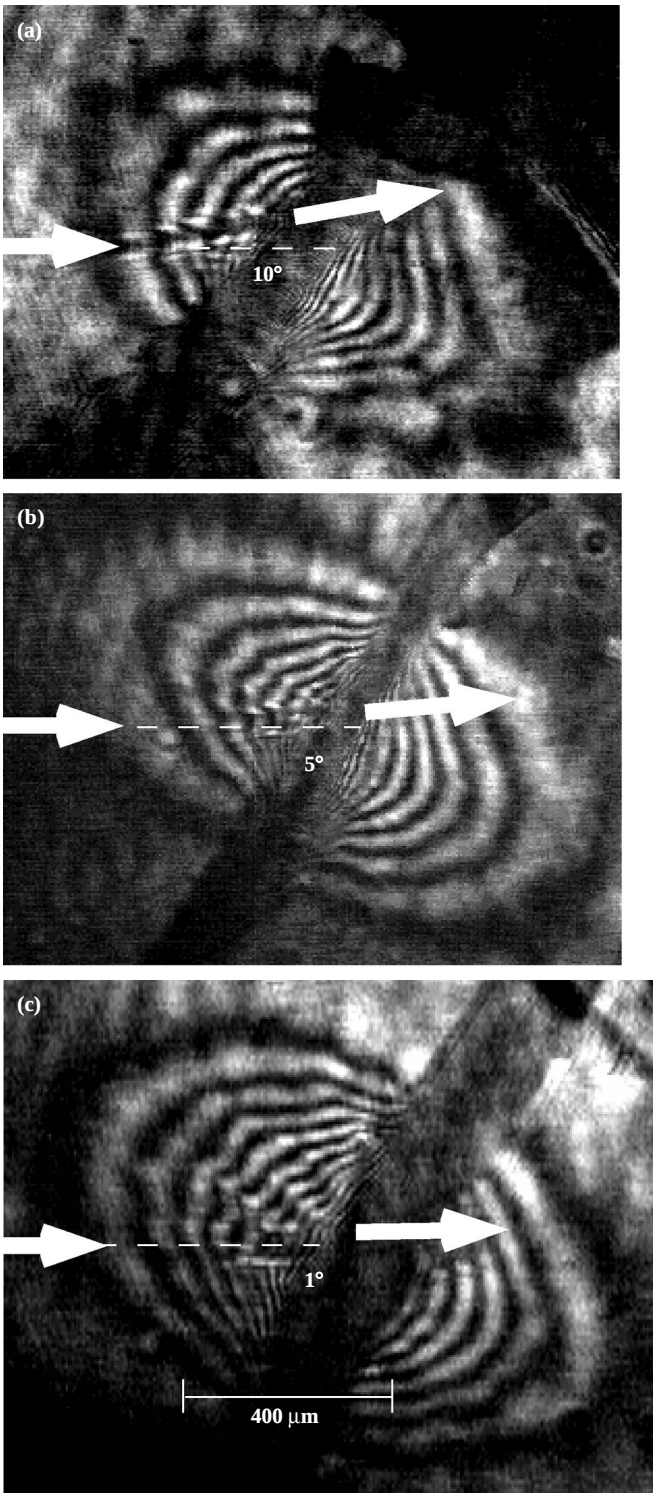

FIGURE 1. Interferograms that show variation in channel bending for peak laser intensities of (a) 1.5×10^{15}, (b) 1×10^{15}, and (c) 5×10^{14} W / cm^2. (50-00-0598-1155pb01)

velocity equals the inferred sound speed c_s. We do this by obtaining plasma interferograms at different times (100-ps steps) relative to the end of the plasma-forming pulse on sequential irradiations of the target. We then Abel invert the interferograms to obtain the plasma density distribution. By using the continuity equation, $\partial n_e / \partial t = \nabla \bullet (n_e \mathbf{v})$, where $\mathbf{v}$ is the flow velocity, we can recover the velocity distribution of the plasma, using the boundary condition, $v = 0$, at the peak of the density profile. We also assume that $\mathbf{v}$ is parallel to ∇n_e. Test calculations with 1D analytic expansion profiles and 2D LASNEX hydrodynamic simulations show that our calculations underestimate the flow velocity at the outer edge of the plasma by ~20%, mainly due to the approximation of calculating dn / dt from the difference of two plasma profiles separated by 100 ps. The outer edge expansion can be corrected, however, by measuring the propagation speed of the outermost fringe in the interferograms. The results are shown in Figure 2 for the conditions of Figure 1; we find a transverse flow velocity of 2×10^7 cm / s, which is close to both the sound speed inferred from earlier Thomson scattering measurements (T_e = 700 eV) on solid carbon targets[13] and the prediction of 2D LASNEX simulations (T_e = 300 eV).

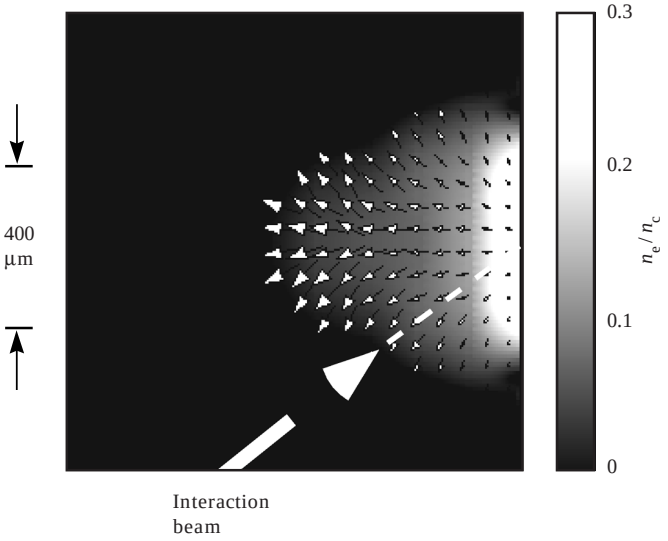

FIGURE 2. Density and flow velocity distributions calculated from the experimental data. The longest arrow corresponds to a flow velocity of 1.4×10^8 cm / sec. (50-00-0598-1156pb01)

Comparison to Numerical Simulations

To understand the laser propagation behavior, the experimental results are compared to numerical simulations. Such simulations will be used predict the performance of NIF-scale targets, so it is important to have a detailed experimental benchmark for the code. To model the experiment, we used a version of the F3D code[4] that incorporated a fully 3D nonlinear Eulerian hydrodynamics package (NH3) in Cartesian

coordinates. F3D is a fully nonlinear, time-dependent code in which the hydrodynamic and heat transport are coupled to the light wave propagation.

The experiment was duplicated in the simulation as much as possible. We modeled the electric field and phase distributions of the interaction beam by using an input phase profile that was experimentally measured using radial shear interferometry and numerically propagating the beam through the lenses used in the experiment (aspheric lens, 20-cm focal length, and two 3.94-m focal length cylindrical lenses that were crossed at a 45° angle to produce the appropriate line focus length). The calculated intensity distribution agrees well with equivalent plane images that were obtained from the experiment (see Figure 3).

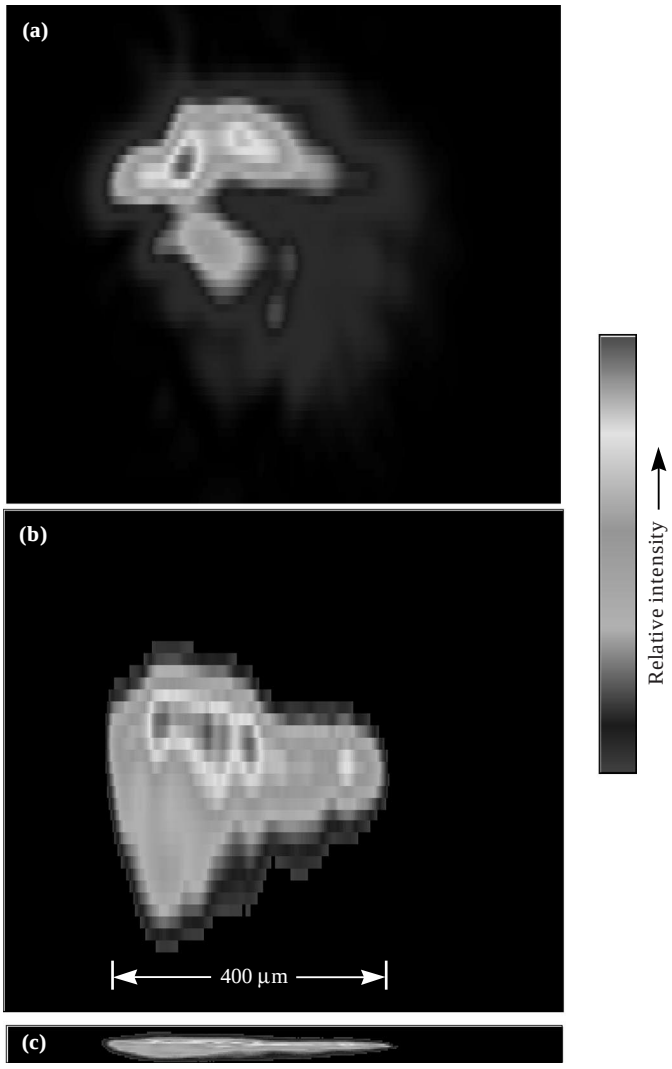

FIGURE 3. Comparison of (a) the calculated intensity using the measured near-field phase-front profile, and (b) the equivalent target plane image of the line focus. The vertical scales of (a) and (b) have been expanded (box heights are 40 μm versus 500 μm for the width of the boxes) to facilitate comparison of the detailed intensity structure. The measured spot in normal aspect ratio is shown in (c). (50-00-0598-1157pb01)

The measured density and flow velocity profiles were used as the starting conditions for the simulation. The 100-ps Gaussian pulse shape used in the experiment is modeled in the simulations by a smoothly rising ramp, $S(t) = 1 - [1 - (t/tp)^2]^2$, where t_p = 100 ps. The measured electron density and flow velocity profiles were used as the initial conditions for the simulation. Because of the narrow cross section of the laser beam, it is only necessary to model a region with transverse dimension of 120 μm and axial dimension of 350 μm. Over this transverse scale, the density and flow can be taken as uniform along the transverse direction initially, but both vary along the axial laser propagation direction. Even after the beam deflects at low density and filaments at higher density, the beam stayed away from the simulation edges as shown in the example in Figure 4. The electron temperature is initially uniform with values taken between 300 and 700 eV to bracket the LASNEX predictions and the Thomson scattering measurements; best agreement with the experiment is found for T_e = 500 eV. The ponderomotive force acts locally to modify the density with nearly 100% modulation at the higher density where the beam breaks up.

Figure 4 shows the calculated density channels, averaged over 50 ps, centered on the peak of the laser pulse, that are formed in the background density profile. The calculations with the experimental flow profile (see Figure 4a) clearly shows a bend of about 10 degrees, in agreement with the experiment. No deflection occurs if the transverse flow is intentionally turned off (see Figure 4b). The initial bend is at the sonic point for an initial temperature of 500 eV. The channel persists for 200 μm past the sonic point, in good agreement with the

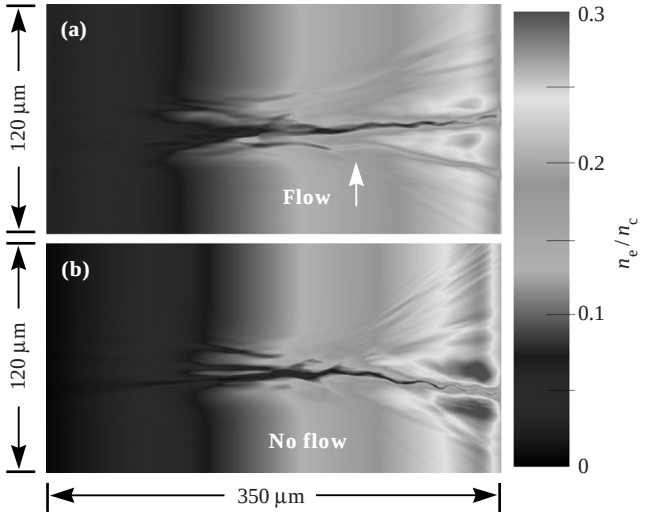

FIGURE 4. Density distributions calculated by F3D using the experimental density profile (a) with the experiment flow velocity profile and (b) with no plasma flow. The simulation has been averaged over 50 ps centered on the peak of the pulse. The laser enters from the left side of the box and propagates to the right. (50-00-0598-1158pb01)

experiment. We performed a number of simulations at different intensities bracketing the nominal laser intensity of the interaction beam. When the simulation intensity is increased by a factor of 5 or greater, the beam breaks up near focus, leaving no clearly defined density channel readily observable by interferometry. Decreasing the simulation intensity results in a decrease in the deflection angle, as expected, with no deflection observed when the intensity is a factor of 100 smaller than the nominal intensity. The scaling of the deflection angle with the laser intensity is in rough agreement with the prediction of Eq. 2.

Conclusion

We have quantitatively measured the beam deflection in a plasma due to transverse plasma flow. The deflection at moderate intensities is predicted well by a simple analytic model. A nonlinear hydrodynamic model using the experimental laser-beam electric field profile, plasma density, and flow velocity distributions shows excellent agreement with the experiment.

Acknowledgments

We thank W. Seka for valuable discussions concerning the near-field phase-front measurement of the laser beam. We would like to thank J. Hunter, G. London, B. Sellick, and J. Foy for technical assistance during the experiment.

Notes and References

1. R. W. Short, R. Bingham, and E. A. Williams, *Phys. Fluids* **25**, 2302 (1982).
2. D. E. Hinkel, E. A. Williams, and C. H. Still, *Phys. Rev. Lett.* **77**, 1298 (1996).
3. J. D. Moody et al., *Phys. Rev. Lett.* **77**, 1294 (1996).
4. R. L. Berger et al., *Phys. Fluids B* **5**, 2243 (1993).
5. W. L. Kruer and J. H. Hammer, *Comments Plasma Phys. Cont. Fusion* **18**, 85 (1997).
6. H. A. Rose, *Phys. Plasmas* **3**, 1709 (1996).
7. D. E. Hinkel et al., *Phys. Plasmas* (in press).
8. W. L. Kruer, *Comments Plasma Phys. Controlled Fusion* **9**, 63 (1985).
9. P. E. Young, M. E. Foord, J. H. Hammer, W. L. Kruer, M. Tabak, and S. C. Wilks, *Phys. Rev. Lett.* **75**, 1082 (1995).
10. P. E. Young, J. H. Hammer, S. C. Wilks, and W. L. Kruer, *Phys. Plasmas* **2**, 2825 (1995).
11. S. C. Wilks, P. E. Young, J. Hammer, M. Tabak, and W.L. Kruer *Phys. Rev. Lett.* **73**, 2994 (1994).
12. S. Ghosal and H. A. Rose, *Phys. Plasmas* **4**, 2376 (1997).
13. P. E. Young, *Phys. Rev. Lett.* **73**, 1939 (1994).

SUPPRESSION OF STIMULATED BRILLOUIN SCATTERING BY MODE COUPLING INDUCED WITH SEEDED ION WAVES

B. I. Cohen *A. B. Langdon*

H. A. Baldis *B. F. Lasinski*

E. A. Williams *C. Labaune**

Introduction

Results from recent laser-plasma experiments conducted at the Laboratoire pour L'Utilisation des Lasers Intenses (LULI)[1] have direct relevance to our laser fusion research and to proposed experiments at the National Ignition Facility (NIF). The LULI researchers observed that the primary ion-acoustic wave (IAW) produced by stimulated Brillouin backscattering (SBBS) of one pump laser beam could be substantially reduced in amplitude in the presence of a secondary SBBS process. The secondary process involved a seed laser beam propagating at a relative angle of 22.5°.

The LULI observation and its elucidation are of significant interest for several reasons. First, the study and control of SBBS have been the object of ongoing theoretical and experimental research for many years because of the importance of SBBS in laser fusion.[2–13] The symmetric compression of fusion targets in either direct drive or indirect drive can be affected by SBBS and other parametric instabilities unless such instabilities are controlled. Second, the NIF will have multiple crossing laser beams and require careful control over the timing and relative amplitudes of the crossing beams.[14] To optimize the fusion performance of experiments proposed for the NIF, the interaction of simultaneous SBBS events in crossing laser beams should be understood. Finally, the nonlinear interaction of driven waves in a plasma is of fundamental interest.

Using model simulations and a mode-coupling analysis, we propose a mechanism that can explain some of the LULI observations. Our research makes use of the BZOHAR, 2D, hybrid (particle ions and Boltzmann fluid electrons) simulation code. The BZOHAR code was introduced and described in more detail in Cohen et al.[15] In brief, Poisson's equation with a nonlinear Boltzmann electron response is solved in two spatial dimensions for the self-consistent, scalar electric potential with the ion density collected from particle ion positions. The Maxwell curl equations are reduced via a temporal envelope approximation to a Schroedinger-like equation for the high-frequency, transverse-wave amplitude. The electron ponderomotive potential arising from the transverse waves is included in the electron Boltzmann response.

Our simulations and analysis indicate that mode coupling of ion waves in the primary and secondary SBBS processes leads to enhanced damping of ion waves. Such mode coupling reduces the ion-wave amplitudes and SBBS reflectivities, as observed in the LULI experiments. Our work is also a logical extension of the earlier work of Maximov et al., which addressed the effects of long-wavelength velocity and density perturbations in detuning stimulated Brillouin scattering (SBS).[16]

Simulations and Analysis

Figures 1 and 2 show the results of 2D, doubly periodic, electrostatic simulations of ponderomotively driven ion waves. The results in Figure 1 are from three simulations in which a primary IAW was resonantly excited by an imposed electron ponderomotive potential. In these simulations, the driver amplitude $e\phi_0 / T_e = 0.05$, $k_s\lambda_{De} = 0.1$ for the driven wave, and $T_e / T_i = 10.27$ in a CH plasma, where the plasma parameters were motivated by the LULI experiments. Here, k_s is the wave number of the driven acoustic wave, λ_{De} is the electron Debye length, and T_e and T_i are the electron and ion temperatures, respectively.

In the first simulation, shown on the left in Figure 1, there was no seeded secondary IAW. The primary IAW relaxed via a decay instability[15] after being driven to a large amplitude. In the second and third simulations shown in Figure 1, a secondary IAW was excited at nearly the same frequency, but at a relative angle of 18°

*Laboratoire pour L'Utilisation des Lasers Intenses, Centre National de la Recherche Scientifique, Cedex, France

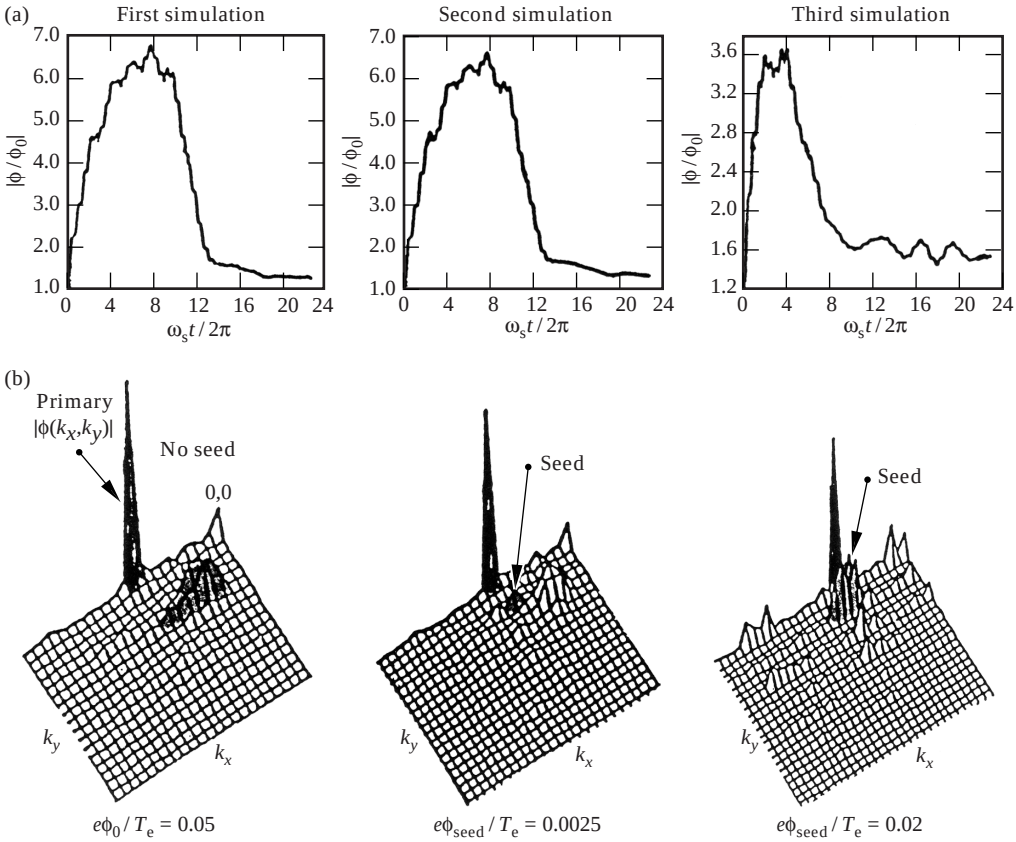

FIGURE 1. (a) Ratio of Fourier amplitudes at the driving frequency and wave number of the plasma electric potential and electron ponderomotive potential $|\phi/\phi_0|$ as a function of time for $e\phi_0/T_e = 0.05$. No seeded secondary IAW was used in the first simulation. In the second simulation, $e\phi_{seed}/T_e = 0.0025$. In the third simulation, $e\phi_{seed}/T_e = 0.02$. (b) The corresponding $|\phi(k_x, k_y)|$ versus k_x and k_y at $\omega_s t/2\pi = 12$ with a $128\Delta x \times 128\Delta y$ domain, 64 particles per species per cell, $k_s\lambda_{De} = 0.1$ for the driven wave, and acoustic driving frequency $\omega_s = k_s c_s/(1 + k_s^2\lambda_{De}^2)^{1/2}$, where c_s is the sound speed, and the seed wave is at an angle of 18° with respect to the primary laser beam.
(50-00-0898-1681pb01)

and with driver amplitudes $e\phi_{seed}/T_e = 0.0025$ and 0.02, respectively. The primary and secondary wave-driving amplitudes were turned on smoothly over two acoustic periods and then left on. The collapse of the primary IAW in the first simulation is caused by the parametric decay into two ion waves at the half-harmonic of the primary IAW k_x wave number and with finite, but generally smaller, k_y. The two-ion-wave parametric decay has been described in Ref. 15 and elsewhere.[17] The primary ion-wave response to its driving potential as a function of time was only minimally reduced by secondary seeding with $e\phi_{seed}/T_e = 0.0025$. However, the primary IAW was reduced substantially for $e\phi_{seed}/T_e = 0.02$, so that the primary IAW did not exceed the threshold for the decay instability.[15] The seed IAW amplitudes were never large enough to exceed this threshold.

Figure 2 shows time histories of the amplitudes of the primary, seed, and beat waves of the primary and seed in the strongly seeded case. The beats of the primary and strong seed grew at the expense of the primary and the seed, and all of the modes ultimately were damped by heating the ions. The decay modes of the primary IAW were observed to grow to amplitudes of $|e\phi/T_e| \approx 0.05$ for the weakly driven seed. In the strongly seeded case, however, the decay modes of the primary IAW achieved amplitudes of $|e\phi_k/T_e| \leq 2 \times 10^{-3}$, which were typical of the simulation noise level in these driven plasmas. The amplitudes of the second and third harmonics of the primary wave tracked the growth and relaxation of the primary in this strongly seeded case. Significant ion trapping and acceleration of a fast ion tail resulted from the action of the primary wave.[5,7,15]

For the simulations shown in Figure 1, the peak amplitudes of the primary ion-wave were $|e\phi_k/T_e| \approx 0.15$ to 0.3. The amplitudes then relaxed to $|e\phi_k/T_e| \approx 0.05$ on a time scale of 5 to 10 acoustic periods. The relaxation is due to the action of ion-wave parametric decay or mode coupling and damping on the ion velocity distribution function. This relatively fast time scale is shorter than the 50-ps temporal resolution of the Thomson scattering used to diagnose the ion-wave amplitudes in the LULI experiments. The LULI measurements suggested ion-wave amplitudes no larger than $|\delta n_e/n_0| \approx |e\phi/T_e| \approx 0.1$. The strength of the mode coupling depends on the product of the primary and secondary IAW amplitudes. With $|e\phi_0/T_e| = 0.01$, which led with no secondary seeding to a peak response $|\delta n_e/n_0| \approx 0.1$, as in the LULI observations, and seeding with $e\phi_{seed}/T_e = 0.003$, we observed in our simulation a peak primary wave amplitude $|\delta n_e/n_0| = 0.08$. This value represents a 20% reduction due to mode coupling with the seed IAW.

Our electrostatic simulations show that mode coupling with the seed IAW provides an additional loss

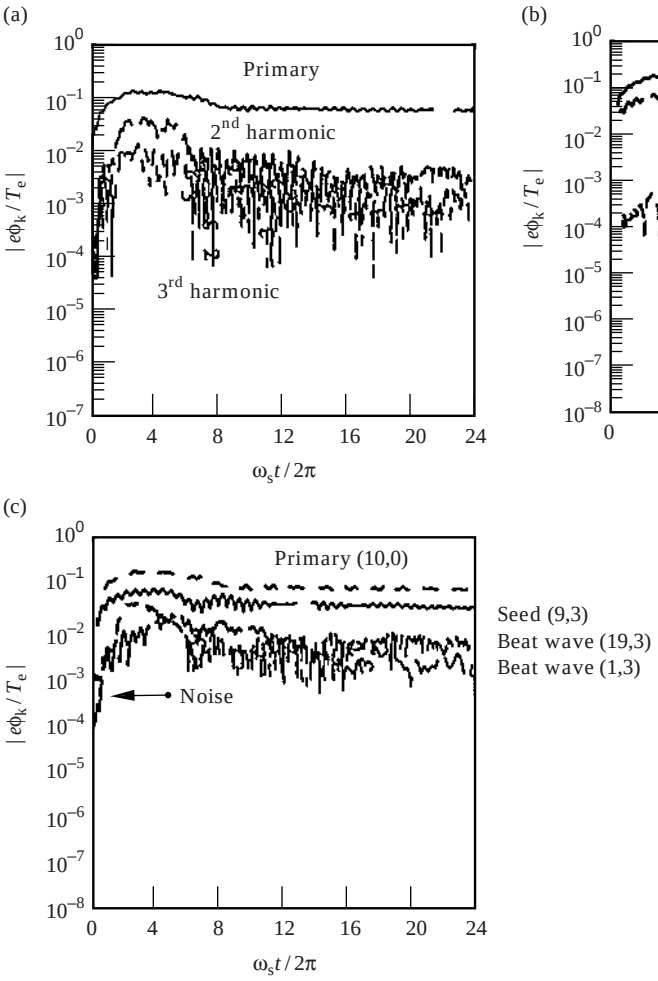

FIGURE 2. Time histories of amplitudes $|e\phi_k/T_e|$ of (a) the primary IAW and its second and third harmonics, (b) the seed wave and a decay mode of the primary, and (c) the beats of the seed and primary IAW for the strongly seeded case in Figure 1. The number pairs in parentheses indicate the *x* and *y* mode numbers of the waves.
(50-00-0898-1682pb01)

channel for the primary IAW, and for the seed as well. The following mode-coupling analysis illustrates how the coupling of ion waves leads to additional dissipation for the primary IAW that reduces its amplification by SBBS and reduces the SBBS reflectivity. Consider the following simplified set of coupled-mode equations for modeling resonant SBBS and heavily damped ion waves in a uniform plasma in steady state:

$$-v_g \frac{\partial a_1}{\partial x} = c_1 a_0^* a_{s1} \tag{1a}$$

for a backscattered transverse wave,

$$\frac{da_{s1}}{dt} = c_2 a_0 a_1 - \gamma_{s1} a_{s1} - c_3 a_{s2} a_{s3} = 0 \tag{1b}$$

for a primary IAW, and

$$\frac{da_{s3}}{dt} = c_4 a_{s1} a_{s2}^* - (\gamma_{s3} + i\Delta_{s3}) a_{s3} = 0 \tag{1c}$$

for a beat-wave IAW.

Here,

- c_1, c_2, c_3, and c_4 are coupling coefficients that can be identified in the analyses of SBBS [2–4,6,7] and the two-ion-wave parametric decay.[15]
- v_g is the group velocity of the backscattered electromagnetic wave.
- *da/dt* is a convective time derivative on a wave amplitude *a*.
- γ_{s1} and γ_{s2} are linear dissipation rates for the ion waves.
- a_0 and a_1 are the amplitudes of the pump and backscattered electromagnetic waves.
- a_{s1}, a_{s2}, and a_{s3} are the ion-wave amplitudes for the primary, seed, and beat waves.
- Δ_{s3} is a frequency mismatch.

The mode-coupling equations are readily solved in steady state when the seed amplitude a_{s2} is a fixed parameter. From Eqs. 1b and 1c,

$$a_{s3} = \frac{c_4 a_{s1} a_{s2}^*}{\gamma_{s3} + i\Delta_{s3}} , \tag{2a}$$

and

$$a_{s1} = \frac{c_2 a_0 a_1}{\gamma_{s1}^{nl}} \ , \tag{2b}$$

where Re γ_{s1}^{nl} is the effective damping of the primary IAW, and

$$\gamma_{s1}^{nl} = \gamma_{s1} + \frac{c_3 c_4 |a_{s2}|^2}{\gamma_{s3} + i\Delta_{s3}} \ . \tag{3}$$

The second term in Eq. 3 represents the enhancement of the damping of the primary IAW arising from mode coupling induced by the seed. A spatial growth rate for SBBS is obtained from Eqs. 1a and 2, as follows:

$$\kappa = -\frac{\partial \ln(a_1)}{\partial x} = \frac{c_1 c_2 |a_0|^2}{v_g \gamma_{s1}^{nl}} = \frac{\gamma_{SBS}^2}{v_g \gamma_{s1}^{nl}} \ , \tag{4}$$

where γ_{SBS} is the homogeneous-medium temporal growth rate for weakly coupled Brillouin backscatter.[2–4,6,7] The exponential amplification of both the backscattered electromagnetic wave amplitude and the primary IAW amplitude in the backward direction over a length L is given by κL. The gain exponent $G \equiv \kappa L$ has been altered by the mode coupling induced by the seed IAW from the gain exponent in the absence of the seed, $G_0 \equiv \gamma_{SBS}{}^2 L / v_g \gamma_{s1}$:

$$G = \frac{\gamma_{s1}}{\gamma_{s1}^{nl}} G_0 \ . \tag{5}$$

The mode coupling leads to enhanced damping of the primary ion wave if $|\gamma_{s1}{}^{nl}/\gamma_{s1}| > 1$, and the gain exponent is reduced correspondingly. A 20% enhancement of the effective dissipation is suggested by the 20% reduction of the primary IAW from our ponderomotively driven electrostatic simulations using parameters appropriate to the LULI experiment. Then, for $G_0 = 5$, which is a typical value for the LULI experiment with laser intensity $I_0 = 10^{14}$ W / cm^2 (Ref. 18), the square of the relative density perturbation in the primary IAW is expected to be reduced by $[\exp(-5 \times 0.2)]^2 = 0.14$. This estimate is in rough agreement with the LULI observations.[1]

If the seed IAW leads to enhanced damping of the primary IAW via mode coupling, we would expect a similar effect on the seed because of the action of the primary IAW. This result is observed in the time histories in Figure 2. After the primary and seed IAW amplitudes are driven to finite amplitudes, they both decay accompanying and following the growth of the beat waves of the seed and primary IAWs. This effect can be understood by augmenting the coupled-mode equations, Eqs. 1a, 1b, and 1c, to include a dynamical equation for the seed IAW of the same form as Eq. 1b. The seed IAW then acquires an enhanced damping rate arising from the mode coupling induced by the primary and the seed of the same form as that in Eq. 3.

The seed IAW in the LULI experiments is excited by the interaction of a seed laser beam propagating at a finite relative angle with respect to the primary laser beam. In our simulations, we considered only the effects of a single, specific seed IAW with the backscatter IAW of the primary laser beam. Dubois, Bezzerides, and Rose[19] analyzed the collective parametric instabilities of many overlapping and converging laser beams. Their formulation is a useful reference for understanding the following qualitative arguments. The Thomson scattering diagnostics in the LULI experiments reveal that, for a weak seed laser strength, the backscatter IAW is the dominant IAW.[1] Therefore, we focused on the mode coupling of the backscatter IAWs of both the primary and the secondary laser beams in this work. However, in the LULI experiments, there was also the mutually resonant IAW propagating at an angle that bisected the angle between the propagation directions of the two laser beams. This mutually resonant IAW was jointly driven by the SBS ponderomotive forces of the primary and seed laser beam. Thus, it was not surprising that its amplitude was enhanced as the seed laser strength was increased. The square of the mutually resonant IAW amplitude scaled approximately linearly with seed laser intensity, suggesting that the seed and primary SBS ponderomotive forces added incoherently.[19] Figures 2, 3, and 4 of Ref. 1 indicate that the primary backscatter IAW amplitude for zero seed laser intensity was larger over a greater volume than was the amplitude of the mutually resonant IAW, which was enhanced over only a very narrow cone of angles. In addition, the suppression effect of the backscatter IAW was more dramatic than was the enhancement effect of the mutually resonant IAW. The overall reflectivities in the LULI experiment were relatively low, ~5%. Pump depletion was not believed to be significant, except perhaps over a short-lived, transient time scale that the diagnostics could not resolve in the experiments.[18]

Our simulations considered only a single seed and primary IAW, rather than a spectrum of IAWs propagating at various angles. We present quantitative arguments for the efficacy of the seed IAW associated with the backscatter of the seed laser in suppressing the backscatter of the primary laser via mode coupling of the IAWs. We expect that the mutually resonant IAW also mode couples with the primary IAW and aids in the suppression effect, because the physics of the mode coupling with the primary IAW is qualitatively the same for both the mutually resonant and nonresonant seed IAWs. Thus, our model calculations likely underestimate the suppression effects of mode coupling on the backscatter of the primary by omitting the mutually resonant IAW. The inclusion of the mutually

resonant IAW in our simulations and a quantitative analysis are beyond the scope of this paper and will be the subject of future research.

To corroborate the suppression of SBBS by mode coupling induced with a seed IAW, we performed electromagnetic simulations of SBBS with a ponderomotively driven, plane-wave seed IAW propagating at 30° with respect to the primary IAW excited by SBBS. These simulations allowed only exactly forward and backward scattered electromagnetic waves ($k_y = 0$) with radiative (outgoing-wave) and charge-conserving boundary conditions in x and periodicity in y. The mesh was $2600\Delta x \times 512\Delta y$, with 25 particles per ion species per cell, $\lambda_{De} \approx \Delta x$, $T_e = 0.6$ keV, $T_e / T_i = 2.4$ in a CH plasma, $L_x \approx 42\lambda_0$, and $L_y \approx 8\lambda_0$. Here, λ_0 is the laser wavelength, and $k_s\lambda_{De} = 0.2$.

Figure 3 shows the results of three electromagnetic simulations for $e\phi_{seed} / T_e = \{0.01, 0.07, 0.14\}$ and a plane-wave laser beam corresponding to 10^{14} W / cm^2 at a wavelength of 1 μm. The time histories of the instantaneous and cumulative time-averaged reflectivities, and the amplitudes $(e\phi_k / T_e)^2$ of the primary IAW in each case demonstrated a significant reduction of reflectivities for $t > 20$ ps and of the primary IAW amplitudes as $e\phi_{seed} / T_e$ was increased. We also performed an additional simulation with no seed, $e\phi_{seed} / T_e = 0$. The results for the time histories of backscatter reflectivities and primary IAW amplitudes were the same as those shown in Figure 3a for $e\phi_{seed} / T_e = 0.01$.

These results illustrate that suppression effects of the seed IAW require both finite amplitude and finite time in which to occur. The maximum observed reflectivities and IAW amplitudes for $t < 20$ ps were unaffected by IAW mode coupling, whose effects set in at a later time after the primary and seed IAWs acquired finite amplitudes. This can be understood by retaining time derivatives in Eqs. 1b and 1c and considering the dynamics. The first peak in the reflectivities and the subsequent relaxation were affected by several nonlinearities observed in the simulation diagnostics. The nonlinearities include ion trapping, transient ion-wave harmonic generation, parametric decay of the primary IAW,[15] and partial pump depletion and associated nonlinear oscillations in reflectivity.

The LULI data demonstrated that the reduction of the primary IAW amplitude was directly correlated with the intensity of the seed laser beam driving the

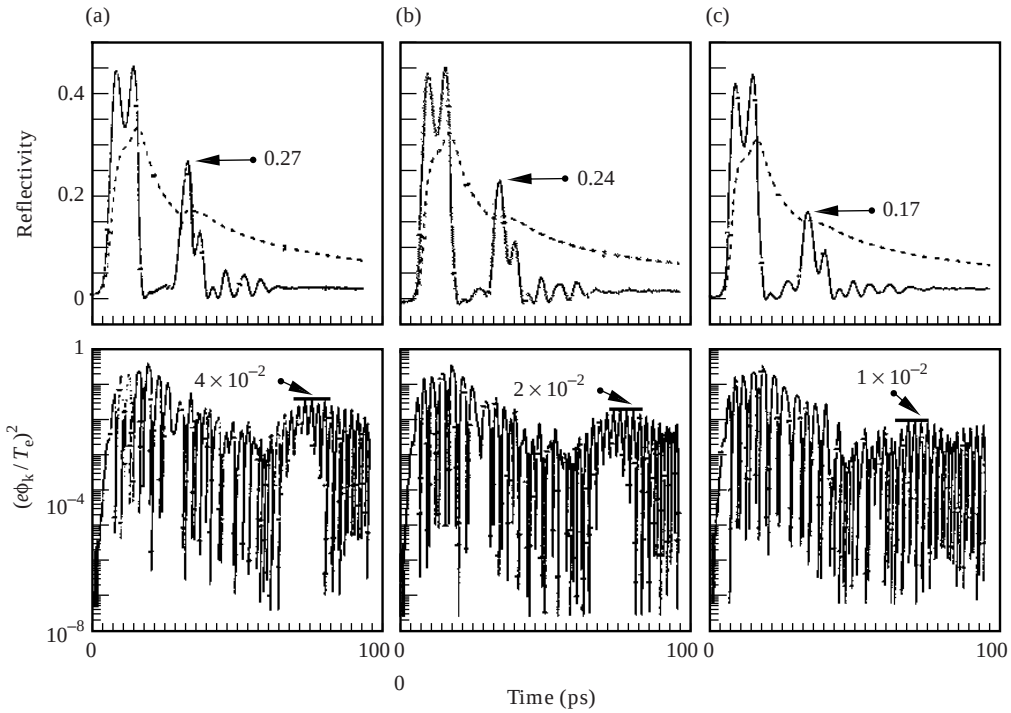

FIGURE 3. Time histories of the instantaneous (solid curve) and cumulative average (dashed curve) reflectivities and primary IAW amplitudes $|e\phi_k / T_e|^2$ as functions of time for (a) $e\phi_{seed} / T_e = 0.01$, (b) $e\phi_{seed} / T_e = 0.07$, and (c) $e\phi_{seed} / T_e = 0.14$. This simulation is in a CH plasma with hydrogen-to-electron mass ratio $m_H / m_e = 1836$, $T_e / T_i = 2.4$, and $k_s\lambda_{De} = 0.2$. The laser electron quiver velocities $v_0^L / v_e = 0.577$ for the input value of the primary laser beam incident from the left side of the simulation. For the input value of the backscatter wave at the right side of the simulation, $v_0^R / v_e = 0.0577$. Here, $v_e = (T_e / m_e)^{1/2}$, and the electron density was equal to 10% critical density. The time histories of $|e\phi_k / T_e|^2$ were computed from the Fourier transform of the electric potential with respect to y at a position $x = L_x / 4$. (50-00-0898-1683pb01)

secondary SBBS process. To more directly connect the results shown in Figure 3 with the LULI data, we performed a series of SBBS simulations with no IAW seeding, but with varying laser intensity. Keep in mind that this is not a self-consistent electromagnetic simulation of the two interacting SBS events, which is beyond the scope of our simulation model. However, mode coupling produced by both the seed and primary IAWs requires a finite time to have a damping effect after the seed and primary IAWs reach finite amplitude. Thus, the relation between the peak SBBS IAW amplitude and single pump laser intensity, and the results of Figure 3, provide a first approximation to the seed laser intensity needed to suppress the backscatter of the primary SBBS.

Figure 4 shows our results for the peak instantaneous reflectivities, the cumulative reflectivities (time-averaged over 100 ps), and peak IAW amplitude $(e\phi_k / T_e)^2$. The results are plotted as functions of the average seed laser intensity I_s / I_0, where $I_0 = 10^{14}$ W/cm^2, with no primary laser beam present. We used the same LULI plasma parameters as in Figure 3. (The seed pump laser was incident from the left side of the simulation box. The input value of the backscattered electromagnetic wave at the right side boundary for the series of simulations shown in Figure 4 was fixed at a relative intensity of 0.005 I_0. The reflectivities and concomitant peak primary IAW amplitudes were relatively insensitive to this input value.) The simulation reflectivity was 5% when averaged over 100 ps for $I_s = I_0$ (the reference LULI intensity). There was also a sharp decrease in reflectivity with decreasing laser intensity. Both of these results are in reasonable agreement with the LULI observations.[18] For $I_s / I_0 < 0.5$, no ion-wave decay instability was observed in our simulations because the peak amplitudes of the primary SBBS IAW were below threshold for the decay instability ($|e\phi_k / T_e| < 0.2$ in this case).[15] When comparing particle simulations of SBBS to experiments, it is important to take into account the temporal resolution of the experimental measurements (typically ≥50 ps). The peak reflectivities and other transient features occurring on time scales less than ~20 ps in the simulations cannot be resolved in the laboratory experiments.

The results from Figure 4 allow us to infer the corresponding seed laser intensity required to produce the seed IAW amplitude used to suppress the primary SBBS process. Figure 5 compares the LULI data on backscatter suppression to our results from the BZOHAR simulation. The primary IAW amplitude $(e\phi_k / T_e)^2$ was reduced to 1/4 its value at the inferred intensity $I_s / I_0 = 0.35$, when compared to its amplitude with no seeding in the simulation. The primary IAW was reduced to 1/6 its unseeded value at an intensity $I_s / I_0 = 0.3$ in the LULI experiments. We expect that by including in our model the other ion waves (including the mutually resonant IAW) produced by the two interacting SBS events, there would be additional mode coupling and a further enhancement of the suppression of the backscatter of the primary pump laser. However, such an inclusion is beyond the scope of our simulation model.

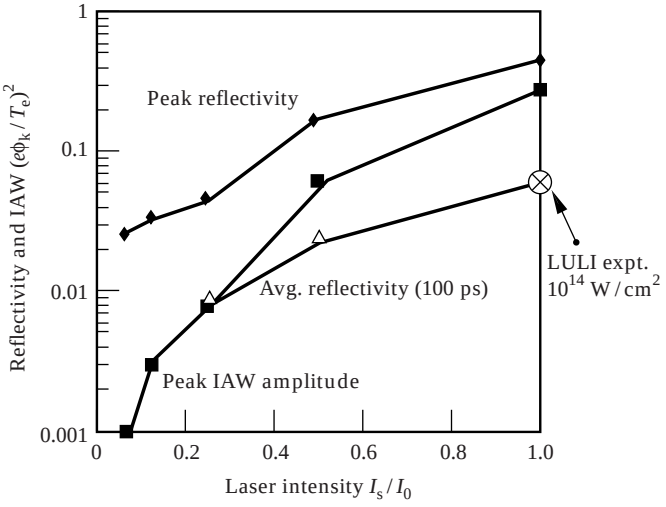

FIGURE 4. Peak and time-averaged (0- to 100-ps, Δ) reflectivities, and peak IAW amplitudes $|e\phi_k / T_e|^2$ as functions of relative seed laser intensity I_s / I_0 for $I_0 = 10^{14}$ W/cm^2. Results are from a series of 2D SBBS backscatter simulations varying v_0^L / v_e incident from the left, and using $v_0^R / v_e = 0.04$ for the backscatter incident from the right. Other parameters were the same as those in Figure 3, with no IAW seeding. (50-00-0898-1684pb01)

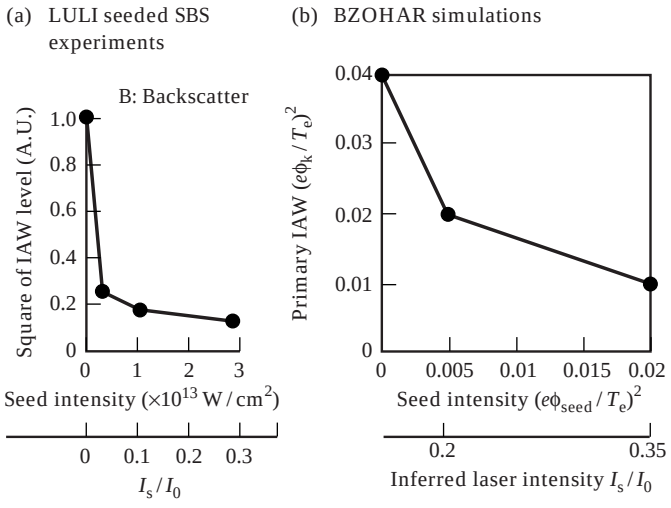

FIGURE 5. (a) Square of the primary SBBS IAW amplitude, in arbitrary units, as a function of seed laser intensity from the LULI experiment.[1] (b) Square of the primary SBBS IAW amplitude $|e\phi_k / T_e|^2$ as a function of seed IAW amplitude and the inferred laser intensity I_s / I_0 from the simulations in Figures 3 and 4. (50-00-0898-1685pb01)

The reflectivities and SBBS suppression exhibited in the simulations are in rough agreement with the LULI observations. Such agreement is somewhat remarkable, given the simplicity of the model. In addition to the omission of the angular spectrum of SBS, the actual laser intensity spatial structure was not incorporated into the simulations. Moreover, the simulation domains were smaller than a single speckle (hot spot) in the LULI beams. However, the simulations did use appropriate, spatially averaged laser intensities and plasma parameters.

The peak reflectivities and corresponding IAW amplitudes may depend on the domain (or speckle) length over which the instability amplifies initially. However, Figure 6 shows the results of an SBBS simulation that suggests that a nonlinear relaxation occurs to a much smaller length scale than the system length, over time scales less than or equal to the temporal resolution of the measurements in the experiments. The picture that emerges from our simulations and multiple-speckle fluid simulations[8] is that SBBS occurs as brief scintillations, dominantly in laser hot spots. Such scintillations give rise to bursts of reflectivity and large-amplitude ion waves. The spatial domains of activity may rapidly shrink as the ion waves and concomitant reflectivity relax with momentum and energy going from the laser to the ion waves, and ultimately into the ion velocity distribution function. The experimental diagnostics integrate in space and time over multiple SBBS scintillations.[18]

Summary

The simulations and analysis presented in this report indicate that a seeded ion wave can induce mode coupling of the seeded and SBBS ion waves (where the seed, SBBS, and beat ion waves are damped on the plasma). Such induced mode coupling substantially suppresses the SBBS reflectivity and its accompanying ion wave. These simulation results are in qualitative agreement with experimental observations by LULI researchers.[1] Such a mechanism may mitigate SBBS activity in other experiments in which intense laser beams cross at finite angles.

Acknowledgments

We are grateful to Richard Berger and other members of the scientific staff at Lawrence Livermore National Laboratory for useful discussions, insight, and encouragement. We also thank the technical groups at LULI for their support.

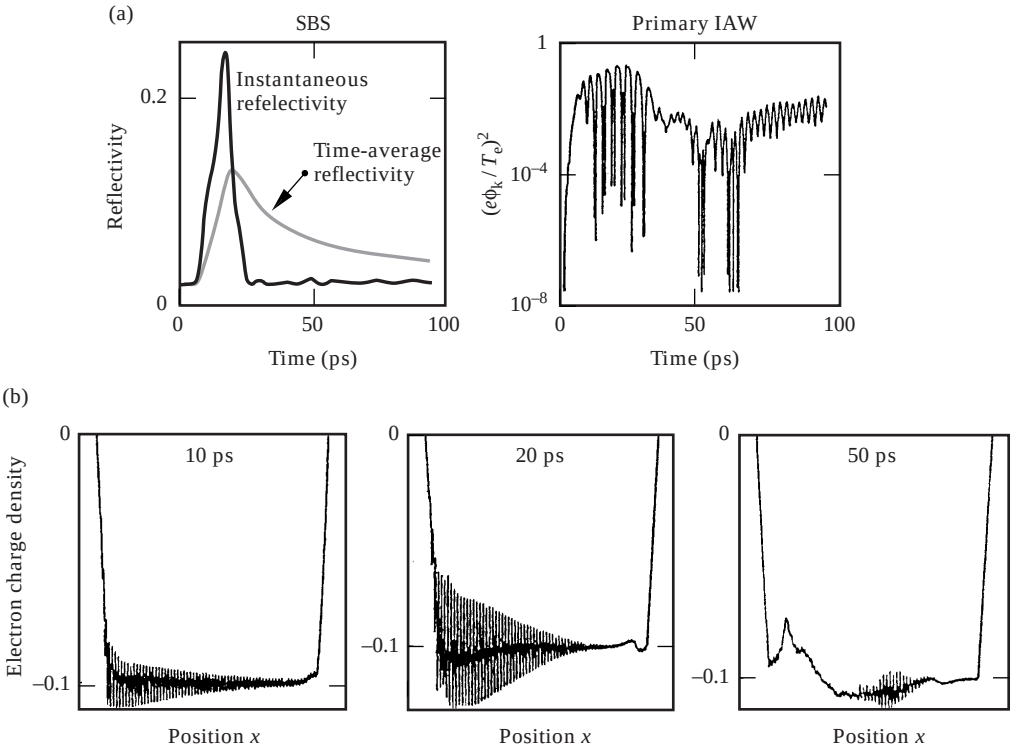

FIGURE 6. (a) Instantaneous and cumulative time-averaged reflectivities, and primary SBBS IAW amplitude $|e\phi_k / T_e|^2$. Results were computed from the Fourier transform of the electric potential with respect to y at $x = L_x / 4$ as functions of time. (b) Snapshots of the y-averaged electron charge density as a function of position x plotted over the entire x domain at 10, 20, and 50 ps. These results are from a simulation with backscatter input boundary condition $v_0^R / v_e = 0.0115$ and no IAW seeding. Other parameters were the same as those in Figure 3.
(50-00-0898-1686pb01)

Notes and References

1. H. A. Baldis, C. Labaune, E. Schifano, N. Renard, and A. Michard, *Phys. Rev. Lett.* **77**, 2957 (1996).
2. V. P. Silin, *Sov. Phys. JETP* **21**, 1127 (1965).
3. J. F. Drake, P. K. Kaw, Y. C. Lee, G. Schmidt, C. S. Liu, and M. N. Rosenbluth, *Phys. Fluids* **17**, 778 (1974).
4. D. W. Forslund, J. M. Kindel, and E. L. Lindman, *Phys. Fluids* **18**, 1002 (1975).
5. D. W. Forslund, J. M. Kindel, and E. L. Lindman, *Phys. Fluids* **18**, 1017 (1975).
6. B. I. Cohen and C. E. Max, *Phys. Fluids* **22**, 1115 (1979).
7. W. L. Kruer, *The Physics of Laser Plasma Interactions* (Addison-Wesley, Reading, MA, 1988).
8. R. L. Berger, B. F. Lasinski, A. B. Langdon, T. B. Kaiser, et al., *Phys. Rev. Lett.* **75**, 1078 (1995).
9. H. A. Baldis, D. M. Villeneuve, C. Labaune, D. Pesme, et al., *Phys. Fluids B* **3**, 2341 (1991).
10. H. A. Baldis, E. M. Campbell, and W. L. Kruer in *Handbook of Plasma Physics*, Vol. 3, A. Rubenchik, ed. (North Holland, Amsterdam, 1990).
11. H. A. Baldis, J. D. Moody, D. S. Montgomery, C. Labaune, et al., *Plasma Phys. Control. Nuc. Fusion Res.* **3**, 221 (1992).
12. L. V. Powers, R. L. Berger, R. L. Kaufman, B. J. MacGowan, et al., *Phys. Plasmas* **2**, 2473 (1995).
13. B. J. MacGowan, B. B. Afeyan, C. A. Back, R. L. Berger, et al., *Phys. Plasmas* **3**, 2019 (1996).
14. National Technical Information Service Document Nos. DE95017671-DE95017673 and DE95017676-DE95017700 (J. A. Paisner, E. M. Campbell, and W. J. Hogan, *The National Ignition Facility Project*, UCRL-JC-117397 and UCRL-PROP-117093, May 1994). Copies may be obtained from Nat. Tech. Inf. Service, Springfield, VA 22161.
15. B. I. Cohen, B. F. Lasinski, A. B. Langdon, and E. A. Williams, *Phys. Plasmas* **4**, 956 (1997).
16. A. V. Maximov, W. Rosmus, V. T. Tikhonchuk, D. F. Dubois, H. A. Rose, and A. M. Rubenchik, *Phys. Plasmas* **3**,1689 (1996).
17. J. A. Heikkinen, S. J. Karttunen, and R. R. E. Salomaa, *Phys. Fluids* **27**, 707 (1984).
18. V. T. Tikhonchuk, C. Labaune, and H. A. Baldis, *Phys. Plasmas* **3**, 3777 (1996).
19. D. F. Dubois, B. Bezzerides, and H. A. Rose, *Phys. Plasmas* **4**, 241 (1992).

THOMSON SCATTERING FROM INERTIAL CONFINEMENT FUSION PLASMAS

S. H. Glenzer *K. G. Estabrook* *J. H. Hammer* *B. J. MacGowan*

C. A. Back *J. S. De Groot*** *O. L. Landen* *S. M. Pollaine*

*M. A. Blain** *B. A. Hammel* *J. D. Lindl* *L. J. Suter*

B. H. Wilde†

Introduction

In the indirect-drive approach to inertial confinement fusion, gas-filled hohlraums are used as radiation enclosures converting high-power laser energy into a soft x-radiation field to achieve a symmetric high-convergence capsule implosion.[1] The gas fill is utilized to reduce inward motion of the Au wall plasma and to obtain high soft x-radiation symmetry. [2,3] To understand the physics of gas-filled hohlraums such as the energetics, beam deflection, or stagnation processes, we have performed collective Thomson scattering measurements[4–8] from the low-Z gas plasma. These experiments provide temporally and spatially resolved measurements of the electron temperature T_e, ion temperature T_i, and plasma flow $\mathbf{v}$ in ignition-relevant hohlraums[9–11], thus benchmarking hydrodynamic simulations.

The hohlraum plasmas were produced at the Nova laser facility using standard millimeter-size Au cavities filled with methane. A gas fill giving a two-ion-species plasma with hydrogen is used to increase ion Landau damping of the ion-acoustic-plasma waves, which reduces laser energy losses by stimulated Brillouin scattering.[12–15] It is therefore adopted in the designs of future hohlraums of the National Ignition Facility (NIF), which use a cryogenic H–He fill. For these reasons, we performed two independent Thomson scattering experiments to ensure accurate characterization of indirectly driven inertial confinement fusion plasmas.

We first performed an open-geometry experiment[16] testing the theory developed by Fejer[17,18] for Thomson scattering spectra from two-ion-species plasmas. Our experimental Thomson scattering spectra from plasmas produced by irradiating flat disks, which were coated with thin Au and Be multilayers, clearly show two ion-acoustic waves belonging to both species. The measured phase velocities are in good agreement with the theoretical predictions calculated for the relative concentrations of the two-ion species. Besides the measurement of the electron temperature, these studies show that an accurate measurement of the ion temperature can be derived from the relative damping of the two ion-acoustic waves. Moreover, plasma flow can be inferred from the Doppler shift of the whole scattering spectra, and the relative ion densities can be measured with high accuracy if the ion charge state is known independently or vice versa.

Subsequent Thomson scattering experiments to characterize methane-filled, millimeter-size hohlraums[19] provide a benchmark for 2D hydrodynamic simulations using LASNEX.[11,20] This code is presently in use to predict the performance of centimeters-size, megajoule-laser-driven hohlraums of the NIF. The measurements show a steep rise of the electron temperature to 5 keV at the peak of the drive which is consistent with calculations only by strongly inhibiting the electron heat transport late in the pulse. A temperature of T_e = 5 keV can be approximated with a flux limiter of f = 0.01 or equivalently reducing Spitzer conductivity by a factor of 10. While this finding is not presently understood, it does indicate that it is necessary to include heat transport limiting effects into the modeling, e.g., magnetic fields[21,22] or nonlocal transport.[23] In this article we will present some simulations that include the toroidal magnetic field while neglecting the axial component. These simulations show marginal improvements. 3D hydrodynamic modeling with the inclusion of magnetic fields as well as experiments quantifying magnetic fields in hohlraums will be necessary to further evaluate the importance of magnetic fields on transport in gas-filled hohlraums. LASNEX simulations of NIF hohlraums show that the symmetry of the fusion capsule is slightly affected by the details of the heat

*Centre D'Etudes de Limeil-Valenton, France

**Department of Applied Science and Plasma Research Group, University of California, Davis, Davis, CA

†Los Alamos National Laboratory, Los Alamos, NM

transport model. Although a heat transport flux limiter of $f = 0.01$ does not affect the radiation temperature in a NIF hohlraum, the x-radiation flux as a function of the incident angle on the fusion capsule differs somewhat from the standard calculations using $f = 0.05$. Although small changes to the beam power balance and pointing can be used to reoptimize symmetry, an improved understanding of heat transport in hohlraums will permit a better specification of the range of suitable ignition hohlraum designs.

The experimental data further shows that ion temperatures and plasma flow, i.e., quantities that are not sensitive to the choice of the heat transport flux limiter, agree quite well with the simulations. In particular, the ion-temperature measurements at the peak of the drive show a fast rise to 4 keV due to stagnation of the compressed plasma on the axis of the hohlraum. The experimental observations are well described by the simulations verifying that high gas pressures from stagnating plasma regions occur late, after the capsule has generated a large surrounding region of ablated material. Our data implies that there is virtually no effect of the gas-region pressure on the capsule implosion in current designs for gas-filled hohlraums.

Experiments

The experiments were performed with the Nova laser facility at the Lawrence Livermore National Laboratory.[24] This facility utilizes a Nd:glass laser operating at 1.055 μm (1ω), which can be frequency converted to 2ω or 3ω. To produce a two-ion-species plasma with a controlled amount of a light and a heavy species, a flat disk of 2 mm diameter was illuminated with a single Nova beam. It was an f/4.3 laser beam illuminating the disk at an angle of 64° to normal. We used a 1-ns square pulse and 2.9-kJ energy at 3ω (λ = 351 nm). A diverging focus resulted in an intensity of $I = 10^{15}$ W/cm^2 on target. The spot size was measured to be 350 × 800 μm by 2D plasma x-ray imaging with a temporal resolution of 80 ps. The disks were coated with Au and Be multilayers of varying thickness. For example, we used 860 layers of 0.5-nm Au and 5.6-nm Be with a total thickness of 2.6 μm on a 51-μm-thick Au or 254-μm-thick Be substrate to obtain a plasma consisting of 4% Au and 96% Be.

The hohlraums were heated with eight or nine 3ω beams with energies of 21 to 25 kJ. They were cylindrical Au enclosures 2750 μm long and with radii of 800 μm. These targets are commonly referred to as scale-1 hohlraums, which are standard targets for capsule implosions.[9] The gas fill was 1 atm of methane (CH_4) giving an initial electron density of $n_e = 2.7 \times 10^{20}$ cm^{-3} when fully ionized. The hohlraums were heated with 8 or 9 unsmoothed heater beams of the Nova laser that are arranged in cones on either side of the hohlraum so that each beam forms an angle of 50° to the hohlraum axis. The heater beams penetrate the hohlraum at both ends through laser entrance holes (LEHs) with radii of 600 μm (Figure 1), which are covered with 0.35-μm-thick polyimide membranes. The beams cross at the center of the holes and are diverging so that they produce an elliptical spot on the hohlraum wall of about 700 × 500 μm. We applied shaped laser pulses of 2.2 ns, which rise from 0.6 to 1.8 TW per beam within approximately 1 ns (see Figure 1).

The probe beam used for Thomson scattering was one of the Nova beams operating at 2ω ($\lambda_i = 526.6$ nm) in a 4-ns square pulse. For the disk experiments, a laser energy of 100 J was chosen, resulting in an intensity of $I = 8 \times 10^{13}$ W/cm^2. In the hohlraum experiments, typical energies of 500 J < E < 1 kJ were employed with three different focal spot sizes at the scattering volume. Intensities of the probe laser at the scattering volume are smaller than the nominal intensity because of absorption of the probe. The experiments show no significant

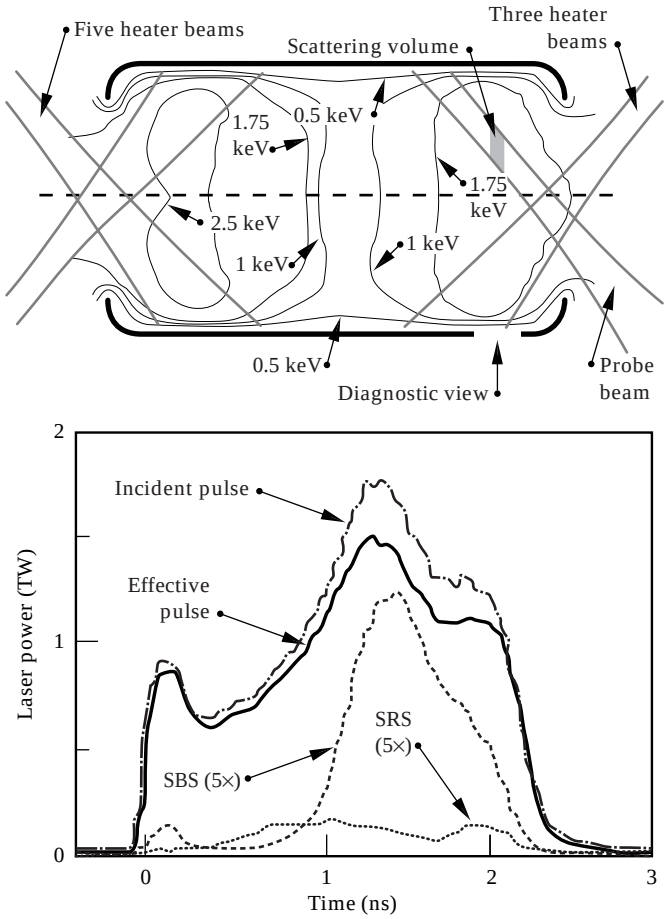

FIGURE 1. Schematic of the hohlraum setup. An electron temperature contour calculated by LASNEX for a gas-filled hohlraum without a capsule is included for $t = t_0 + 0.8$ ns. The location of the scattering volume indicated by the shaded area is in the homogeneous part of the CH-plasma. Also shown is the laser power of a single beam together with measured losses by stimulated Brillouin scattering (SBS) and stimulated Raman scattering (SRS). The total energy loss is 14%. (08-00-0798-1545pb01)

effect of the probe laser on the plasma conditions. When the probe laser intensities were varied by one order of magnitude in the hohlraum experiment, they did not affect the temperature of the plasma.

The scattered light was imaged at a scattering angle of $\theta = 104°$ with f/10 optics and a 1:1.5 magnification onto the entrance slit of a 1-m spectrometer (Spex, model 1704). An optical streak camera (S-20) was used to record spectra with 30-ps temporal resolution. High spatial discrimination of 133 μm in the vertical direction and 66 μm in the axial direction was obtained by choosing the entrance slit width of the spectrometer to be 200 μm and by employing a streak camera slit height of 100 μm. The spectrometer employed a 2,400-g/mm grating blazed at 500 nm, resulting in a reciprocal linear dispersion of 0.220 nm/mm (first order). The wavelength resolution of the measurements was 0.1 nm. Wavelength calibration and absolute calibration of the detection system were performed with a Ne spectral lamp and a W lamp.

Collective Thomson scattering is expected for the parameters of the experiments (electron density, temperature, scattering angle, and probe-laser wavelength). Typical scattering parameters are $\alpha = 1/k\lambda_D > 3$, and light is predominantly scattered into the narrow ion feature of the Thomson scattering spectrum.[25] In this regime, the spectrum of a single species plasma shows two ion-acoustic features (red and blue shift for co- and counter-propagating ion-acoustic waves). The frequency separation of the ion-acoustic features is twice the ion-acoustic frequency, and the propagation direction of the corresponding ion-acoustic waves in the plasma is determined by the scattering vector $\mathbf{k}$, $\mathbf{k} = \mathbf{k}_s - \mathbf{k}_i$. The incident wave vector is defined by $\mathbf{k}_i = (2\pi / \lambda_i)(\mathbf{e}_i)$, where λ_i is the incident probe-laser wavelength and $\mathbf{e}_i$ is the unit vector in direction of the probe laser. Similarly, $\mathbf{k}_s$ points in the direction of the detector. For a two-species plasma with two ion-acoustic waves (each with red and blue shift), the Thomson scattering will show four ion-acoustic features.

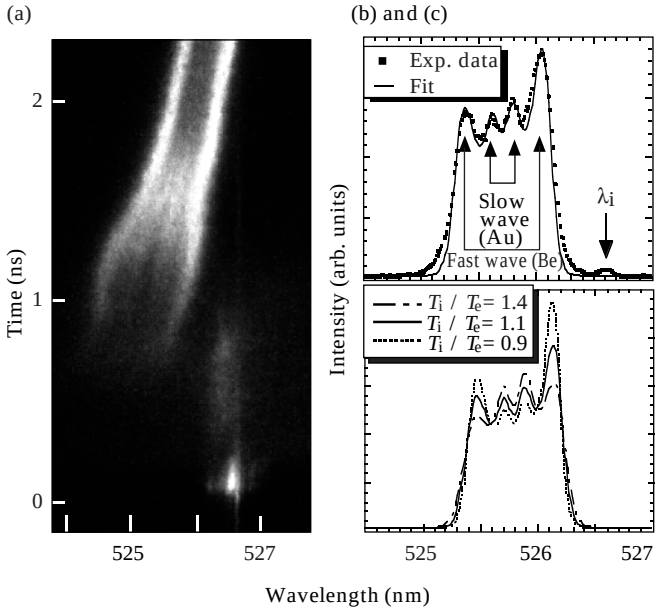

FIGURE 2. (a) Time-resolved Thomson scattering spectrum from a 4% Au, 96% Be plasma detected at a distance of 500 μm from the target. Also shown is (b) the Thomson scattering spectrum at $t = t_0 + 1.55$ ns with a theoretical fit, and (c) the variation of the scattering spectrum for various ratios of T_i / T_e. (08-00-0798-1546pb01)

Experimental Results and Discussion

Disk Experiments

Figure 2 shows the Thomson scattering data recorded from a 4% Au, 96% Be disk target with the probe laser focused at a distance of $z = 500$ μm from the disk surface. The probe laser was parallel to the disk and focused to 200 μm diameter. Four ion-acoustic features, the two outer ones belonging to Be and the two inner ones belonging to Au, can be clearly seen for $t_0 + 0.9$ ns $< t < t_0 + 1.7$ ns. The 3ω heater beam lasts from 0 to 1 ns and the 2ω probe beam from 0 to 4 ns. The Thomson scattering signal is fairly symmetric and starts at $t = t_0 + 0.8$ ns. It shows an increasing separation of the ion-acoustic features for about 0.2 ns, indicating increasing temperatures of the plasma during the heating period. After the end of the heating at $t = t_0 + 1$ ns, the separation of the ion-acoustic features decreases rapidly because the plasma cools due to radiative cooling and expansion. For the time interval shown in Figure 2, Thomson scattering gives temperatures of the plasma of 200 eV $< T_e <$ 900 eV, ensuring that the Be ions are fully ionized. The separation and damping of the ion-acoustic features belonging to the Be ions can be used directly to determine the electron temperature. In addition, electron densities with an uncertainty of about a factor of two are obtained from the calibration of the detector. This predicts a scattering parameter α well above three for our conditions, in which case scattering spectra are not sensitive to the electron density.

The signal detected about 0.8 ns before the onset of the Thomson scattering signal is due to unconverted 2ω stray light from the heater beam. This feature is not caused by the probe beam and represents a convenient timing and wavelength fiducial. The delay of 0.8 ns is due to the time needed for ablation and travel of the plasma from the disk surface to the scattering volume. When the plasma reaches the scattering volume, it is moving towards the observer, resulting in a blue shift of the Thomson scattering signal. The shift yields the instantaneous macroscopic plasma motion along the scattering vector $\mathbf{k}$. The measured blue shift of 1.7 nm

at $t = t_0 + 0.9$ ns corresponds to a velocity of 10^8 cm / s. It is obvious from Figure 2 that this is well above the sound speed because the shift of the whole Thomson scattering signal is larger than half the wavelength separation of the ion-acoustic features.

Figure 2b shows a spectrum at $t_0 + 1.5$ ns < t < $t_0 +$ 1.6 ns. Four ion-acoustic features due to the slow and the fast ion-acoustic waves are clearly identified. The small asymmetry is probably caused by the heat-flux-driven return current.[26] The experimental data are fitted with a theoretical spectrum that compensates for the asymmetry by slightly decreasing the damping of the waves on the red wing.[6,27] Apart from the slight asymmetry, analysis of the spectrum yields considerable information. Because the relative intensities of the ion-acoustic features are determined by damping of the Au and Be ion-acoustic waves, the theoretical fit to the spectrum gives $T_i / T_e = 1.1$ (see Figure 2c). From the wavelength separation of the Be ion-acoustic features, we find $T_e = 230$ eV. We can then infer $\alpha = 7$ for the electron densities from the intensity of the scattering signal and from hydrodynamic simulations. Finally, the wavelength separation of the Au features gives $Z = 40$. The theoretical spectrum fits the experimental data quite well. Small deviations are probably due to small plasma-parameter gradients within the scattering volume.

Figure 3 shows the compilation of our experiments with relative Au concentrations of 1%, 2%, 4%, and 8% for experiments using an unsmoothed Nova heater beam and for experiments using a kinoform phase plate in the heater beam. The ratio of the wavelength separation of the Au ion-acoustic features to the Be ion-acoustic features is plotted as a function of the Au concentration.

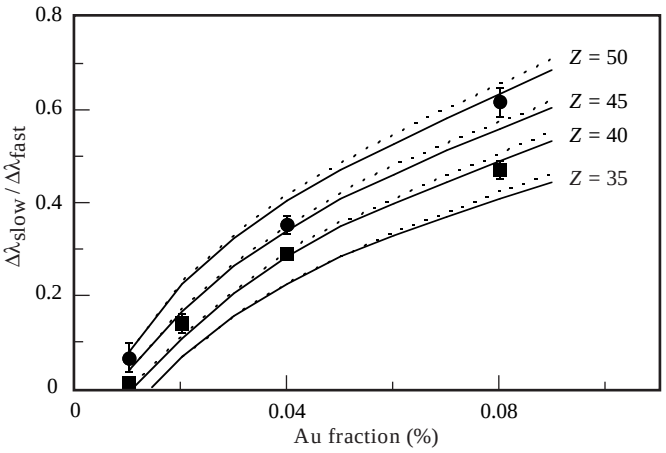

FIGURE 3. Ratio of the wavelength separations of the ion acoustic features belonging to Au to those belonging to Be on the Thomson scattering signal for different Au concentrations. Ratios are shown for unsmoothed heater beams (■) which were taken at $t = t_0 + 1.55$ ns when $T_i / T_e \sim 1.1$ and $\alpha \sim 7$. Also plotted are experimental ratios with a kinoform phase plate in the heater beam taken at $t = t_0 + 1.3$ ns when electron temperatures and Z are slightly larger giving $T_i / T_e \sim 1.3$ (•). The error bars are estimated from the noise of the data. Theoretical data after Evans[18] are shown for Z = 35, 40, 45, 50, $T_i / T_e \sim 1.1$ (full line) and $T_i / T_e \sim 1.3$(dotted line). (08-00-0798-1547pb01)

This data is taken at $t = t_0 + 1.55$ ns for the unsmoothed case and at $t = t_0 + 1.3$ ns for the smoothed case when the intensity of the Au features is at its maximum. For very small Au concentrations of 1%, the Thomson scattering signal shows a central peak belonging to the heavy Au ions in addition to the ion-acoustic waves belonging to the Be ions. The existence of a central peak was also observed in a two-species discharge plasma consisting of H and small amounts of heavy gases.[27,28] Increasing the amount of the Au species of the two-species plasma results in a larger separation of the ion-acoustic features of Au. For the 2% case the ion-acoustic waves of Au become discernible as two individual peaks on the spectrum. For a mixture of 4% Au, 96% Be two separate ion-acoustic waves were clearly observed (Figure 2). By further increasing the amount of Au to 8%, the ion-acoustic waves of Au and Be almost merge together. From the theoretical fit of the spectra we find that T_i / T_e, the scattering parameter α, and charge state Z of the Au ions are the same for all experiments to within 15%.

The experimental data clearly shows the increase of the wavelength separation of the Au ion-acoustic feature with increasing concentration. The theoretically calculated results[18] are also plotted for various Z of the Au ions. The experimental data are in excellent agreement with the theory for $Z = 40$ for the unsmoothed case and for $Z = 45$ for the smoothed case. The latter resulted in slightly larger temperatures and consequently slightly larger ionization stages. The values of Z compare quite well with hydrodynamic LASNEX calculations which give $Z = 45$ and 49, respectively.

Our experimental results are in excellent agreement with the theory of Fejer[17] and Evans.[18] Our data shows that Thomson scattering from a two-ion-species plasma is an accurate diagnostic of electron temperature and ion temperature. The observation of both the fast and the slow wave on the Thomson scattering spectra shows that they are moderately to strongly damped. In this regime, Landau damping is a strong function of the ion temperature, resulting in a highly accurate ion-temperature measurement. In addition, the relative ion densities can be measured with high accuracy if the ion charge state is known independently or vice versa.

Hohlraum Experiments

Figure 4 shows the Thomson scattering data from a gas-filled hohlraum heated with eight heater beams with a total energy of 21 kJ.

The scattering volume is 400 μm inside the hohlraum (see Figure 1 on p. 60) and the Thomson

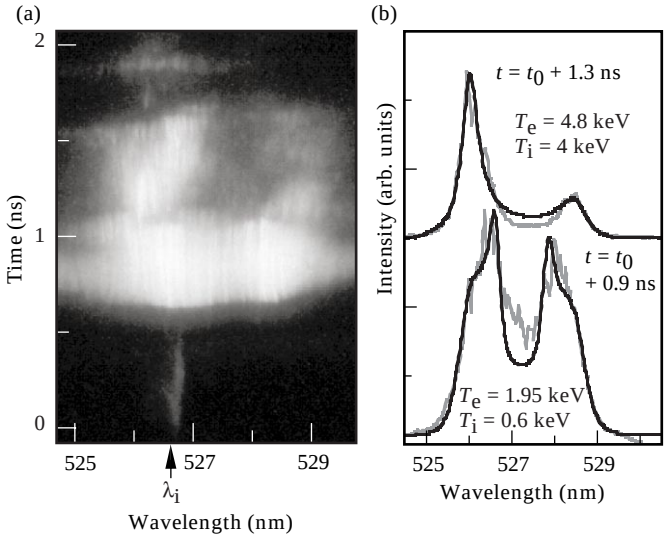

FIGURE 4. (a) Time-resolved Thomson scattering spectrum from CH_4 for eight heater beams inside the hohlraum. (b)The spectra are fitted with the form factor of Evans[18] giving electron and ion temperature of the plasma. (08-00-0798-1548pb01)

scattered light is observed through a diagnostic window (700×400 μm) cut into the hohlraum wall and covered with polyimide. For $t_0 < t < t_0 + 0.65$ ns, no Thomson scattering signal can be observed. Estimates show that during this time the polyimide foil that covers the diagnostic window produces an overdense plasma for 2ω light. During that time a faint line due to stray light or unconverted 2ω light from the heater beams can be identified on Figure 4a. Again, it is used as a timing and wavelength fiducial. For $t_0 + 0.65$ ns $< t < t_0 + 1.1$ ns, two broad, symmetric, ion-acoustic features are observed from light scattering off the CH_4 plasma. For $t_0 + 1.1$ ns $< t < t_0 + 1.6$ ns, when the heater beam power rises significantly (see Figure 1), the separation of the ion-acoustic features increases, indicating a rising electron temperature and, in addition, the width of the ion-acoustic features narrows showing an even faster increase of the plasma's ion temperature. Furthermore, the Thomson scattering spectrum shows an asymmetry probably related to electron heat flux towards the hohlraum wall, which would result in different electron Landau damping of the co- and counter-propagating ion-acoustic waves.[26,29] For $t > t_0 + 1.6$ ns, a cut-off of the Thomson scattering signal occurs because the electron density of the CH-plasma rises steadily during the heating of the hohlraum due to compression by the inward-moving wall plasma. The Thomson scattering spectra from the hohlraum experiments consist of four features: Two co- and counter-propagating ion-acoustic waves belonging to C (slow wave) and to H (fast wave).[12,16] Fitting the data with the form factor for a two-ion-species plasma, which has been tested with experiments described above, yields the separation and the relative damping of both waves, measuring accurately the electron and ion temperature of the plasma.[16]

Figure 4b shows the spectra at $t = t_0 + 0.9$ ns and $t = t_0 + 1.3$ ns averaged over 80 ps with a fit using the form factor of Evans.[18] For the data analysis, it is assumed that light scattering occurs on a fully ionized CH plasma. Our hydrodynamic simulations, as well as temporally resolved 2D x-ray images observing the Au-plasma emission at energies of $E > 2.5$ keV, show that Au ions were not present in the scattering volume for $t < t_0 + 1.7$ ns (see Figure 5). The x-ray images view the hohlraum plasma along its axis. They show a five-fold radiation pattern due to the Au blowing off the wall where the heater beams illuminate the hohlraum. Therefore, the radiation of the Au blowoff from the five heater beams on either side overlap on the images. At $t = t_0 + 1.6$ ns (see Figure 5c), the Au emission close to the scattering volume is therefore not from the side of the hohlraums where we have performed the Thomson scattering measurements and is not affecting the data.

If small amounts of highly ionized Au ions existed in the scattering volume, the Thomson scattering spectra would clearly indicate their presence by showing a central peak. For example, 5% Au can be readily detected. This is demonstrated in Figure 6, where we compare calculated Thomson scattering spectra of three-ion-species plasmas. The parameters are $T_e = 2$ keV, $T_i = 0.6$ keV, $n_e = 1.3 \times 10^{21}$ cm^{-3}, and assuming a fully ionized methane plasma with various amounts of Au impurities ionized to $Z = 50$. For a Au ion density of $N_{Au} = 10^{18}$ cm^{-3}, which corresponds to 0.8% Au ($Z = 50$) in a fully ionized methane plasma, the Thomson scattering spectrum deviates only slightly from the case without Au impurities. The assumption of a pure CH plasma has virtually no effect on the inferred plasma parameters. However, assuming larger Au impurities of $N_{Au} = 5 \times 10^{18}$ cm^{-3} (corresponding to 4.8% Au in CH) significantly enhances the center of the spectrum, and the ion-acoustic wave that belongs to H (fast wave) is significantly less than the ion-acoustic wave belonging to C (slower wave).

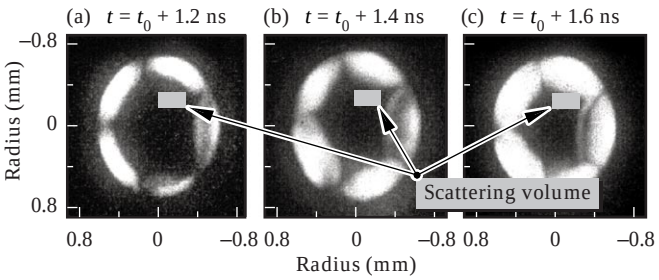

FIGURE 5. Time-resolved 2D x-ray images of the hohlraum gold emission with energies $E > 2.5$ keV observed along the hohlraum axis. (08-00-0798-1549pb01)

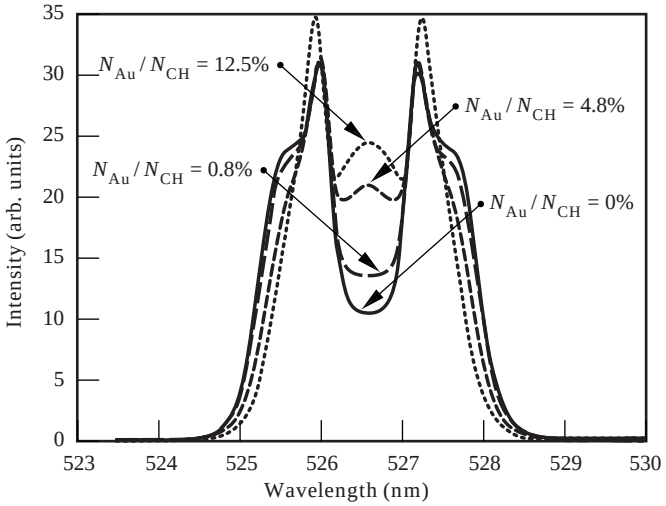

FIGURE 6. Calculated Thomson scattering spectra for a methane plasma (CH_4) with various amounts of gold impurities with Z = 50. (08-00-0798-1550pb01)

These features become even clearer for $N_{Au} = 10^{19}$ cm^{-3} (corresponding to 12.5 % Au in CH). It is obvious that neglecting the Au impurities would result in large errors for the ion temperature (throughout this article we assume that the temperatures of the ion species are equal because of fast ion–ion equilibration times[30] in the plasmas under study). On the other hand, the Thomson scattering spectrum provides us with a clear indication of the impurity concentration. Experimentally we do not observe an enhancement of the center of the Thomson scattering spectrum and conclude that Au impurities are negligible for our conditions (see Figure 4b, $t = t_0 + 1.3$ ns).

In Figure 7 we plot the temporal evolution of the electron temperature from Thomson scattering with the results of the radiation hydrodynamic LASNEX simulations. Data are shown for eight heater beams (a) and for nine heater beams (b). The experimental electron temperatures clearly scale with the number of heater beams. We observe peak values of 4.5 and 5.2 keV, respectively. The reproducibility of the measurements from 12 shots is about 20%.

Varying the probe laser focus in the range of 150 to 500 μm diameter at the scattering volume did not affect the experimental temperatures. This result is consistent with LASNEX calculations, which show a rather homogeneous electron temperature about 400 μm inside the hohlraum (see Figure 1). For the analysis, we have calculated the scattering parameter α using electron densities from LASNEX. Although for the present experiment we have $\alpha \approx 3$ so that the spectra are not density sensitive, the **k** vector was slightly corrected[31] from its vacuum value because electron densities in the scattering volume approach 0.25 n_{cr}. $k' = (1 - n_e/n_{cr})^{1/2} k$, with k from the triangle relation $k = 4\pi/\lambda_i \sin(\theta/2)$, and n_{cr} is the critical density for the 2ω probe [$n_{cr} = 1.1 \times 10^{21}/(\lambda_i)^2$]. Ignoring this effect would result in electron temperatures reduced by 10 to 20%. The density correction introduces an additional uncertainty to the experiment, resulting in a total error bar of 15% for T_e and 20% for T_i.

In Figure 7 we compare the experimental data with 2D hydrodynamic simulations, in which the hohlraum axis is chosen to be the axis of symmetry in the calculations. The calculated temperatures are taken at the location of the scattering volume, which is at a radial distance of 300 μm from the hohlraum axis and 950 μm from the center of the hohlraum (see Figure 1 on p. 60). This comparison is justified because the probe beam is not affected by beam deflection or refraction. In Hinkel[32] a deflection of 6° was calculated for scale-1 hohlraums,

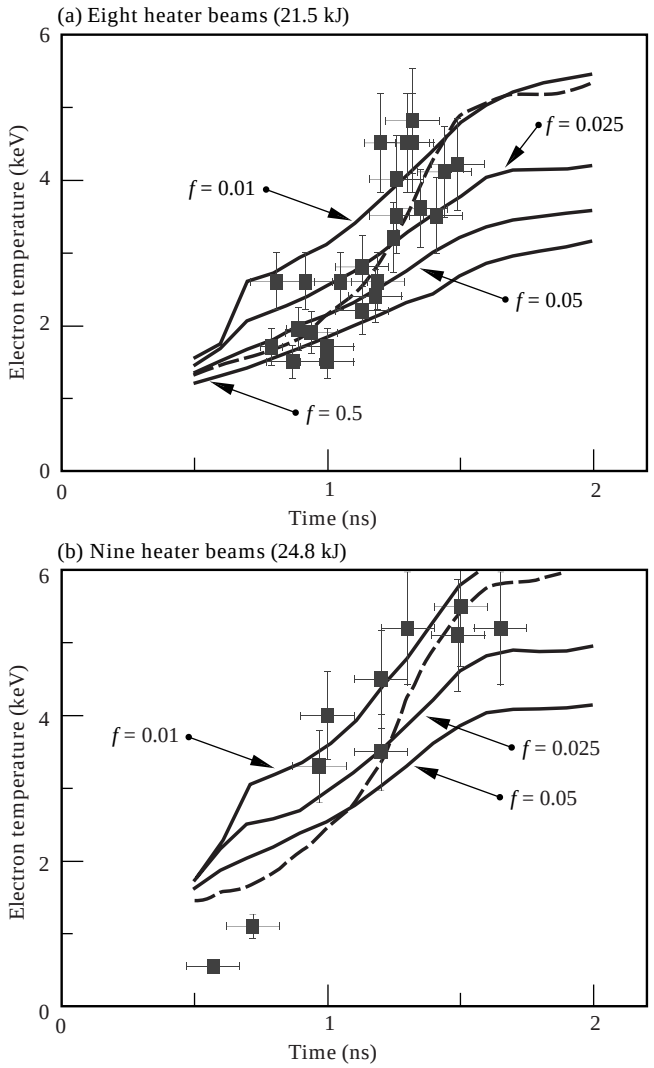

FIGURE 7. Hohlraum electron temperatures as a function of time for (a) eight and (b) nine heater beams together with hydrodynamic simulations with various electron heat flux limiters. The dashed curves employ a time-varying flux limiter and show good agreement with the experimental electron temperatures. (08-00-0798-1551pb01)

which show Mach-1 plasma flow orthogonal to the beam path. The parameters of the calculations were a 3ω beam with intensities of $I = 3 \times 10^{15}$ W/cm^2 in a 3-keV plasma with 0.1 n_e / n_{cr}. Scaling this result to our conditions via[32] $(I\lambda_i^2) / T_e \times n_e / n_{cr}$ gives a deflection angle of $\phi \leq 1°$. Refraction can be estimated with ϕ (rad) $\cong 0.5 \times (\Delta n\, L) / (n_{cr}\, \Delta y)$ where L is the path length of the laser beam through a plasma region which shows density variation Δn across the beam waist Δy. For our conditions we find $\phi \cong 1°$. Adding these numbers results in a maximum deviation of the 2ω probe beam of $\phi = 2°$ along its path from the laser entrance hole to the scattering volume (~600 μm). It corresponds to an error of 21 μm in beam pointing, which is negligible. However, more than 20% of the probe laser power is absorbed on its path to the scattering volume. This explains the decrease of the scattered light intensity with increasing time as seen in Figure 4 because the electron density increases steadily. For this reason, an electron density determination from the intensity of the ion feature cannot be made.

Our radiation hydrodynamic simulations of both NIF and Nova hohlraums are carried out with the LASNEX[20] computer code, which uses a flux-limited diffusion model for heat transport. In this approximation, heat flow per unit area in regions of large classical heat flow $-\kappa \nabla T_e$ has an upper bound of $f (n_e T_e v_e)$, where $n_e T_e v_e$ is the so-called free-streaming value of heat transport and f is the flux limit. Flux limiters of $0.01 < f < 0.1$ have been found necessary to model laser-heated disk experiments[33] in which steep temperature gradients near the disk surface cause classical heat flow to become unphysically large. In laser-heated hohlraums, however, the confined geometry results in very different temperature and density profiles so that the heat flow is flux limited over the volume of the hot plasma. For that reason, equivalent results can be obtained by merely reducing the classical transport coefficient. In Figure 7, calculations are shown for various (constant) free streaming electron heat transport flux limiters in the range of $f = 0.5 - f = 0.01$. For example, using $f = 0.025$ agrees with the experimental electron temperatures to within 35%. However, the best description of the experimental data is obtained when assuming a time-varying flux limiter of $f = 0.1$ at early times decreasing to $f = 0.01$ at the peak of the drive (dashed curve in Figure 7). Alternatively, we can model the experiment with classical transport reduced by a factor of 5 to 10. For gas-filled hohlraum plasmas, electron heat transport inhibition (due to magnetic fields) by a factor of about 20 was predicted by Bodner.[21] Also, nonlocal heat transport[23,34] could be important for the present observations. Experiments and calculational efforts[35] are presently ongoing to better understand and quantify these effects.

A variety of calculational tests were performed to verify that, besides the electron heat transport model, other approximations in the calculation are not important for the present study. An effect on the electron temperature of <5% was seen when we varied the focal spot size in the 2D code to test the approximation of the laser beam power used in the simulations, or when we included hot electrons in the simulations.

Very recently we have performed LASNEX simulations that include a preliminary model for self-consistent toroidal magnetic fields. They use $f = 0.5$ equivalent to classical heat transport, and show an increase of the electron temperature by 7% at the Thomson scattering volume. This increase is not sufficient to explain our experimental observations. However, the calculations do show localized hot spots near the center of the hohlraum. It is obvious that 3D calculations will be necessary to obtain a definitive answer on the importance of magnetic fields on electron heat transport in gas-filled hohlraums.

The Thomson scattering data also gives information about macroscopic plasma flow in hohlraums, which is an important parameter affecting beam pointing.[32,36] In Figure 2 we observe a red shift of the spectra due to plasma motion away from the heater beam spots on the hohlraum wall. The speed is subsonic ($v = 4.3 \times 10^7$ cm/s) and underestimated by the 2D simulations by a factor of 2 to 3. This Doppler shift (as well as the heat-flux-driven asymmetry) is a 3D effect and occurs when only eight heater beams are employed. When nine heater beams are applied, the red shift of the spectra decreases to about 20% of the sound speed ($v = 1.4 \times 10^7$ cm/s), and the spectra become symmetric because of the improved symmetry of the hohlraum heating. In this case, agreement of the flow velocity with the hydrodynamic simulations is obtained within 30%. Unfortunately, the Thomson scattering spectra with nine heater beams show increased stray light levels because the additional heater beam illuminates part of the diagnostic window.

Ion temperatures as a function of time for eight or nine heater beams are shown in Figure 8. They are less sensitive to the heat flux limiter. The experimental ion temperatures show a steep rise to a peak value of 4 keV. From the hydrodynamic simulations we deduce that this behavior is due to stagnation of the compressed low-Z plasma on the axis of the hohlraum. Electron–ion temperature equilibration times are too large (>1 ns) to explain the experimental data. In Figure 8 the simulated ion temperature rise is delayed compared to the experimental data by ~0.4 ns while in case of nine heater beams, a delay of ~0.2 ns occurs. These observations can be explained by the fact that the hydrodynamic simulations are 2D and assume a cylindrical symmetric heating. However, in the case of eight heater beams, the heating is fairly asymmetric so that the plasma stagnates slightly off-axis closer to the Thomson scattering volume, giving rise to an earlier ion temperature increase than seen in the simulations. In case of nine heater beams, the symmetry of the heating is improved and stagnation occurs closer to the hohlraum

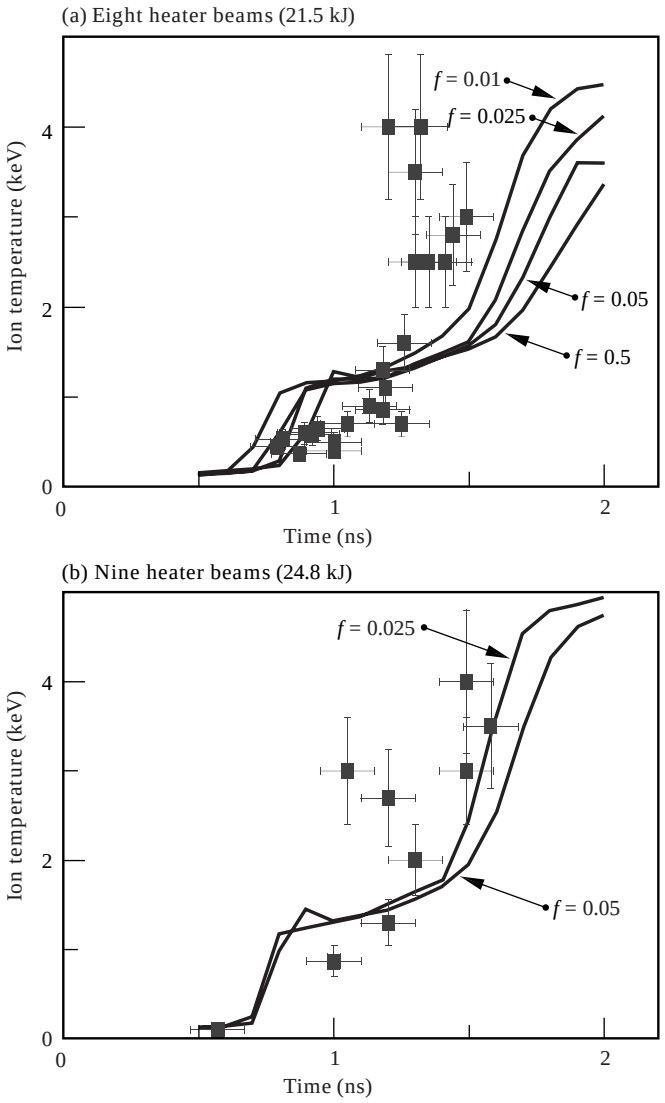

FIGURE 8. Hohlraum ion temperatures as a function of time for (a) eight and (b) nine heater beams together with hydrodynamic simulations with various electron heat flux limiters. The temperature of the hydrogen and carbon ions is assumed to be equal because of high ion–ion collision frequencies. Ion temperatures are not sensitive to the choice of the heat flux limiter. They show a steep rise because of stagnation effects. (08-00-0798-1552pb01)

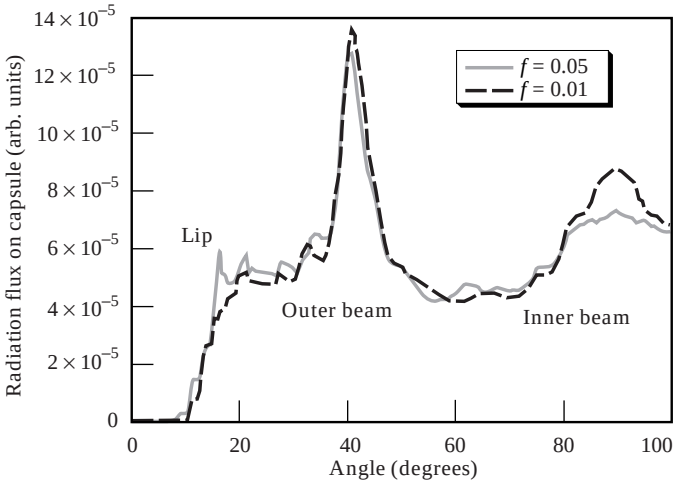

FIGURE 9. Calculated NIF antenna pattern, i.e., the x-ray flux seen by the capsule as a function of angle, at $t = t_0 + 7.5$ ns and for constant flux limiters of $f = 0.05$ and $f = 0.01$. (08-00-0798-1553pb01)

because the x-ray flux seen by the capsule as a function of angle is modified. This is shown in Figure 9, where the results of LASNEX simulations are shown for constant flux limiters of $f = 0.05$, which is the standard flux limiter, and $f = 0.01$ to estimate the maximum effect of heat transport inhibition as it is seen in Nova hohlraums on NIF simulations.

These calculations show that increasing the heat transport inhibition by going from $f = 0.05$ to $f = 0.01$ results in a slightly increased x-ray flux from the locations where the inner and outer beams illuminate the hohlraum walls, while the x-ray radiation from the lip of the laser entrance hole is reduced. The positions of these regions are shown schematically in Figure 10.

These simulations confirm that strongly inhibiting heat transport in the NIF hohlraum design results in slightly less x-ray production in wall regions that are not directly heated by the laser beams and that are axis so that the beginning of the ion temperature rise is better described by the LASNEX simulations. In particular, the reasonable agreement between the ion temperatures measured at the peak of the drive and the maximum calculated ion temperatures shows that stagnation processes in gas-filled hohlraums are rather well described by the simulations.

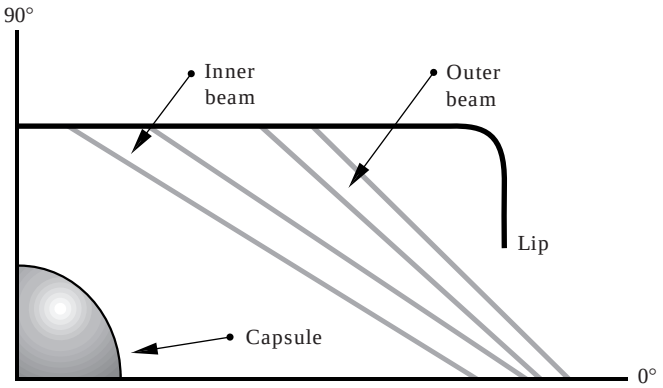

FIGURE 10. Schematic of the NIF hohlraum showing the locations of high x-ray flux production as seen by the capsule. (08-00-0798-1554pb01)

Consequences for NIF Hohlraums

When a reduced flux limiter of $f = 0.01$ is used in NIF calculations, the optimal beam power balance and the optimal beam pointing are slightly modified

partly heated by conduction. The x-ray flux produces an ablation pressure on the fusion capsule that must be very symmetric to achieve high convergence and ignition of the fusion capsule.

While the total x-ray flux is not affected by the increased heat-transport inhibition (see inset of Figure 11), the symmetry of the fusion capsule is modified. In Figure 11 we show the ratio P_2/P_0 as a function of time which has been optimized for $f = 0.05$ by adjusting beam power and pointing. P_2 is the coefficient of the Legendre polynomial describing the pole–equator asymmetry, while P_0 describes the spherical flux. Optimization means reducing the capsule asymmetries by minimizing the ratio P_2/P_0 (as well as higher-order Legendre polynomials).

Using beam power and pointing that was optimized for $f = 0.05$ for the calculations with $f = 0.01$, results in larger amplitudes of the ratio P_2/P_0 and consequently the capsule yield decreases from 16.1 MJ to 3.8 MJ. The pointing and relative power of the beams have to be adjusted in order to improve the capsule yield.

Finally, the reasonable agreement between the experimentally observed stagnation and the LASNEX simulations shows that capsule implosions in gas-filled hohlraums are not directly affected by the pressures produced in the stagnation regions. For example, early NIF hohlraums used plastic liners[1] instead of a gas fill to produce the low-Z beam propagation region in the hohlraum interior. These liners blew inward at high velocity and generated an early-time axial stagnation pressure, which affected the subsequent capsule implosion symmetry. However, in the gas-filled hohlraums, the high gas pressures occur late, after the capsule has generated a large surrounding region of ablated material. In these hohlraums, there is virtually no effect of the gas-region pressure on the capsule implosion. Because the capsule is moving inward and the radiation-ablated capsule blowoff is moving outward at speeds comparable to the sound speed in the gas fill, the capsule is essentially isolated from the pressure generated in the gas. This is true for both the Nova experiments and for the NIF target designs. In NIF calculations, the capsules have essentially the same symmetry and implosion velocity in integrated calculations that explicitly account for the low-Z gas pressure[2,3,11] and in separate calculations that only drive the capsule with the hohlraum x-ray flux. However, the effect of the stagnation plasma regions on the level of parametric instabilities, which result in filamentation and backscatter losses by SBS and SRS, for example, has not yet been quantified.

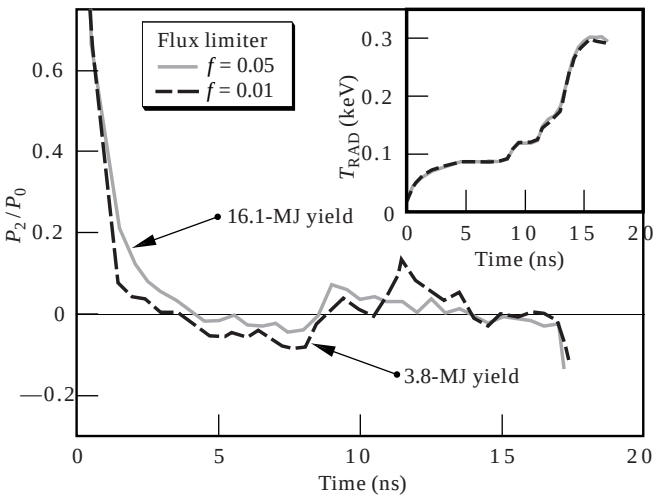

FIGURE 11. Calculated ratio of the P_2/P_0 symmetry of the NIF capsule for constant flux limiter of $f = 0.05$ and $f = 0.01$. The inset shows the radiation temperature as function of time. Both calculations essentially overlap. In case of $f = 0.01$ reoptimization of the beam power and pointing will be necessary to increase the capsule gain. (08-00-0798-1555pb01)

Conclusions

We have developed Thomson scattering as a powerful diagnostic of inertial confinement fusion plasmas. Open-geometry experiments were performed verifying the theory of Fejer.[17,18] They show that Thomson scattering measures temporally and spatially resolved electron and ion temperature in two-ion-species plasmas with high accuracy from the frequency separation and damping of the ion-acoustic waves. Furthermore, plasma flow can be inferred from the Doppler shift of the whole scattering spectra, and the relative ion densities can be determined if the ion charge state is known independently, or vice versa. Applying this theory for the Thomson scattering spectra from closed-geometry hohlraum plasmas produced with 21 to 25 kJ at the Nova laser facility benchmarked radiation hydrodynamic LASNEX simulations. These studies are important for our understanding of heat transport, energetics, and beam pointing in gas-filled hohlraums. The ion temperatures and plasma flow, i.e., quantities that are not sensitive to the choice of the heat transport flux limiter, agree quite well with the simulations. This implies that stagnation effects are well described by LASNEX. The simulations show that stagnation occurs too late in gas-filled hohlraums so that there is no direct effect of the high pressure stagnating plasma on the fusion capsule.

On the other hand, the experimental electron temperatures are best approximated with a time-varying flux limiter showing large electron heat-transport inhibition at the peak of the drive. This observation is presently not understood. We have started to include heat-transport-limiting effects into the hydrodynamic modeling, but more calculational and experimental work remains to be done for a complete description of the heat transport in gas-filled hohlraums. Another calculational attempt to understand the experimental

results used calculations that include magnetic fields in hohlraums. They show the occurrence of megagauss magnetic fields, hot spots, and significant heat transport inhibition in plasma regions close to the scattering volume. Although these results are encouraging as they show features that are observed in the present hohlraum experiments, there is not yet experimental verification of the existence of such high magnetic fields in hohlraums.

New experiments are presently being performed with a 4ω probe laser to improve our understanding of the physics in ignition experiments. The new 4ω probe diagnostic will allow us to measure temperatures in directly and indirectly heated regions of the hohlraum as well as on the hohlraum axis. In addition, the experiments will be performed with smoothed Nova beams. These types of experiments provide benchmarks for the radiation hydrodynamic modeling, and we hope that they will ultimately help us to improve the modeling for accurate prediction of the plasma conditions in fusion targets.

Acknowledgements

We thank E. M. Campbell, A. A. Offenberger, A. J. MacKinnon, and D. Hinkel for helpful discussions.

Notes and References

1. J. D. Lindl, *Phys. Plasmas* **2**, 3933 (1995).
2. S. W. Haan et al., *Phys. Plasmas* **2**, 2480–2487 (1995).
3. W. J. Krauser et al., *Phys. Plasmas* **3**, 2084–2093 (1995).
4. H.-J. Kunze, in *Plasma Diagnostics*, edited by W. Lochte-Holtgreven (North-Holland, Amsterdam, 1968) p. 550.
5. A. W. DeSilva and G. C. Goldenbaum, in *Methods of Experimental Physics*, edited by H. R. Griem and R. Lovberg (Academic, New York, 1967), Sec. V9A.
6. D. E. Evans and Katzenstein, *Rep. Pro. Phys.* **32**, 207–271 (1969).
7. J. Sheffield, *Plasma Scattering of Electromagnetic Radiation* (Academic, New York, 1975).
8. N. C. Luhman, Jr. and W. A. Peebles, in *Laser Handbook*, edited by M. Bass and M. L. Stitch (North-Holland, Amsterdam, 1985), Vol. 5, p. 455.
9. B. A. Hammel et al., *Phys. Rev. Lett.* **70**, 1263 (1993).
10. R. L. Kauffman et al., *Phys. Rev. Lett.* **73**, 2320–2323 (1994).
11. L. J. Suter et al., *Phys. Rev. Lett.* **73**, 2328–2331 (1994). *Phys. Plasmas* **3**, 2057–2062 (1996).
12. E. A. Williams et al., *Phys. Plasmas* **2**, 129 (1995).
13. B. J. MacGowan et al., *Phys. Plasmas* **3**, 2029–2040 (1996).
14. R. K. Kirkwood et al., *Phys. Rev. Lett.* **77**, 2706–2709 (1996).
15. J. C. Fernandez, *Phys. Rev. Lett.* **77**, 2702–2705 (1996).
16. S. H. Glenzer et al., *Phys. Rev. Lett.* **77**, 1496–1499 (1996).
17. J. A. Fejer, *Can. J. Phys.* **39**, 716 (1961).
18. D. E. Evans, *Plasma Phys.* **12**, 573 (1970).
19. S. H. Glenzer et al., *Phys. Rev. Lett.* **79**, 1277–1280 (1997).
20. G. B. Zimmerman and W. L. Kruer, *Comments Plasma Phys. Controlled Fusion* **2**, 85 (1975).
21. S. E. Bodner, *Comments Plasma Phys. Controlled Fusion* **16**, 351 (1995).
22. J. A. Stamper and B. H. Ripin, *Phys. Rev. Lett.* **34**, 138 (1975); M. G. Haines, *Phys. Rev. Lett.* **78**, 254 (1997).
23. J. R. Albritton, E. A. Williams, I. B. Bernstein, and K. P. Swartz, *Phys. Rev. Letters* **57**, 1887 (1986); J. F. Luciani, P. Mora, and R. Pellat, *Phys. Fluids* **28**, 835 (1985); A. R. Bell, R. G. Evans, and D. J. Nicholas, *Phys. Rev. Lett.* **46**, 243 (1981).
24. E. M. Campbell, J. T. Hunt, E. S. Bliss, D. R. Speck, and R. P. Drake, *Rev. Sci. Intrum.* **57**, 2101 (1986).
25. E. E. Salpeter, *Phys. Rev.* **120**, 1528 (1960); J. A. Fejer, *Can. J. Phys.* **38**, 1114 (1960); J. P. Dougherty and D. T. Farley, *Proc. Roy. Soc. Ser.* A **259**, 79 (1960).
26. J. S. De Groot et al., "Laser Interaction and Related Plasma Phenomena" (in *AIP Conf. Proc.*, No. 318, Plenum Press, 1994), pp. 135–143.
27. T. Wrubel, S. Glenzer, S. Büscher, and H.-J. Kunze, *J. Atmos. Terr. Phys.* **58**, 1077 (1996).
28. A. W. DeSilva, T. J. Baig, I. Olivares, and H.-J. Kunze, *Phys. Fluids* B **4**, 458 (1992).
29. V. T. Tikhonchuk, W. Rozmus, V. Yu. Bychenkov, C. E. Capjack, and E. Epperlein, *Phys. Plasmas* **2**, 4169 (1995).
30. L. Spitzer, Jr., *Phys. Rev.* **58**, 348 (1940).
31. B. La Fontaine et al., *Phys. Plasmas* **1**, 2329 (1994).
32. D. S. Hinkel, E. A. Williams, and C. H. Still, *Phys. Rev. Lett.* **77**, 1298 (1996).
33. D. S. Montgomery et al., *Phys. Rev. Lett.* **73**, 2055 (1994); S. H. Batha et al., *Phys. Plasmas* **2**, 3792 (1995); S. H. Glenzer et al., *Rev. Sci. Instrum.* **68**, 668 (1997).
34. B. B. Afeyan, A. E. Chou, and W. L. Kruer, *Phys. Rev. Lett.* **80**, 2322 (1998);
35. R. Town, private communication (1997).
36. H. S. Rose, *Phys. Plasmas* **3**, 1709 (1996). J. D. Moody et al., *Phys. Rev. Lett.* **77**, 1294 (1996).

OBSERVATION OF ENERGY TRANSFER BETWEEN IDENTICAL-FREQUENCY LASER BEAMS IN A FLOWING PLASMA

K. B. Wharton[*] *B. B. Afeyan*[**]

R. K. Kirkwood *B. I. Cohen*

S. H. Glenzer *J. D. Moody*

K. G. Estabrook *C. Joshi*[†]

Introduction

Energy transfer between two intersecting laser beams in a plasma directly addresses fundamental aspects of laser–plasma interactions and is also relevant to laser-driven inertial confinement fusion (ICF). When an electromagnetic wave (frequency ω_0, wave number $\mathbf{k}_0$) intersects another electromagnetic wave with equal or lower frequency (ω_1, $\mathbf{k}_1$), optical mixing will drive a beat-wave density perturbation in the plasma at (Ω, $\mathbf{K}$):

$$\Omega = \omega_0 - \omega_1; \mathbf{K} = \mathbf{k}_0 - \mathbf{k}_1 . \quad (1)$$

If the driven beat-wave satisfies the plasma-dispersion relation, then this three-wave interaction is resonant and can be very efficient.[1,2] Electron plasma waves can be driven in this manner, using two laser beams with a difference in frequency equal to the electron plasma frequency.[1,3] This technique has found applications in particle acceleration.[4–6] For beams of comparable frequency, resonance can be reached when (Ω, $\mathbf{K}$) satisfies the dispersion relation ($\Omega = \omega_{ia}$, $\mathbf{K} = \mathbf{k_{ia}}$) = 0 for ion-acoustic waves in a flowing plasma:

$$\omega_{ia} = c_s \, |\mathbf{k_{ia}}| + \mathbf{v_d} \bullet \mathbf{k_{ia}} . \quad (2)$$

Here c_s is the ion sound speed, and $\mathbf{v_d}$ is the drift velocity of the plasma. In subsonic plasmas ($|\mathbf{v_d}| < c_s$), Eq. 1 and Eq. 2 show that identical frequency beams cannot drive a resonant ion wave. With the appropriate frequency mismatch, however, resonant ion waves have been driven by microwaves[7] and also by two laser beams.[8] This latter experiment measured a modest transfer of energy mediated by a resonant ion wave, as evidenced by the fact that no energy transfer was observed for two laser beams of equal frequency.

Nonresonant ion waves have been produced with two identical frequency beams, which were found to have an effect on stimulated Raman scattering.[9] More recently, Lal et al. have observed energy transfer between two λ = 10.6-μm-wavelength laser beams,[10] but this was during a transient period on the order of a few acoustic periods, during which energy transfer may occur between identical frequency beams.[11,12] These previous experiments were performed in subsonic plasmas. In a supersonic plasma ($|\mathbf{v_d}| \geq c_s$) the resonant ion wave can have zero frequency in the laboratory frame if $\omega_{ia} = 0$ in Eq. 2, and the ion wave can therefore transfer energy between two identical frequency beams over many acoustic periods.[13–15] In this article, we present the first measurements of steady-state energy transfer between identical frequency beams in a plasma with supersonic flow.

This effect has been the subject of much theoretical work,[12,16,17] in part motivated by current designs for fusion experiments on the National Ignition Facility[18] (NIF) in which multiple laser beams cross as they enter a cylindrical radiation enclosure (hohlraum). Because the plasma flow leaving the enclosure is near supersonic,[15] there may be resonant energy exchange between the laser beams. This would have deleterious effects on the symmetry of the laser radiation inside the hohlraum and might require the use of the NIF's ability to frequency detune the crossed beams and avoid a resonance.

Experimental Configuration

The experiments were performed on the 10-beam Nova laser facility at Lawrence Livermore National Laboratory (LLNL), using four $f/4.3$ beams with

*University of California, Los Angeles, Los Angeles, CA, and Lawrence Livermore National Laboratory, Livermore, CA
**Polymath Associates, Livermore, CA, and University of Nevada, Reno, Reno, NV
†University of California, Los Angeles, Los Angeles, CA

λ = 351 nm. Two of the beams were partially defocused to 80-μm-diam spots, each spatially smoothed with a kinoform phase plate[19] (KPP) and each containing 3 kJ of energy in a square pulse lasting from $t = 0$ to $t = 3$ ns. These two heater beams were incident (40° to normal) on both sides of a 5-μm-thick Be ($Z = 4$) rectangular foil, 2 mm by 4 mm. The exploding foil was initially modeled with LASNEX,[20] using the heater beam parameters described above. A layer with Mach 1 flow ($|\mathbf{v_d}| = c_s$) was calculated to move out from the initial foil position over time, reaching a distance of 500 μm from the foil at $t = 3$ ns. At this time, the density along the center normal of the foil had reached a 1-mm-scale plateau of a roughly constant electron density $n_e = 0.06\, n_c$, where n_c is the critical density for 351-nm light (9×10^{21} cm^{-3}).

The flow velocity was experimentally characterized with a Thomson scattering technique.[21] A lower-intensity, λ = 526-nm beam was focused in a 100-μm full-width at half maximum (FWHM) spot, 500 μm from the center foil position. The frequency- and time-resolved Thomson scattered light is shown in Figure 1a. At $t = 2.9$ ns, the upshifted ion wave feature overlaps the stray light, signifying that $\omega_{ia} = 0$ and that a Mach 1 plasma flow was present. Figure 1b shows that this measured Mach 1 position ($z = 500$ μm, $t = 2.9$ ns) is consistent with the LASNEX calculation. However, the measured electron plasma temperature at $t = 2.9$ ns is 0.8 ± 0.1 keV, lower than the predicted 1.2 keV at this location. The error bars of the Mach 1 measurement are largest in the direction away from the foil due to the possibility that the beam was deflected by the plasma density gradient, with a maximum error defined by the spatial view of our diagnostic. Even with this effect, the error in the Mach 1 measurement is much smaller than the spatial and temporal extent of the region sampled in the main experiment.

The main experiment was then performed by crossing two additional λ = 351-nm beams in the exploding foil plasma. We refer to the higher-intensity beam as the "pump" and the lower-intensity beam as the "probe." As shown in Figure 2, these beams arrived from opposite directions, separated by an angle of 152°. Both the pump and probe were incident at 14° from the normal of the foil (the z-axis, defined in Figure 2), and the resultant ion wave was therefore aligned to the plasma flow along the z-axis. The pump and probe beams were originally focused at a location $z = -500$ μm from the $z = 0$ initial foil position. The pump has a higher frequency in the frame of the flowing plasma on the $-z$ half of the foil, and therefore the resonance would be expected to transfer energy from the pump to the probe and the ion wave.

The probe light transmitted through the plasma was incident on a frosted fused-silica plate 1.5 m from the target, and the scattered light was then imaged onto a fast photodiode.[22] Postprocessing of the photodiode signal helped correct for the finite-time response of both the large scatter plate and the diode. The final absolute uncertainty in the transmission measurements is ±14% (±20% for time scales <100 ps), and the relative uncertainty between different shots is ±10%.

The specifications of the crossing beams were as follows: the pump beam was identical to the heater beams (square pulse, 3 kJ in 3 ns, KPP), but arrived 1 ns late, staying on from $t = 1$ ns to $t = 4$ ns. The pump was focused to a 340-μm full-diam spot, reaching an intensity of 10^{15} Wcm^{-2}. The probe beam had a typical energy of 0.2 kJ, and two focal spots were used. First, no phase plate was used on the probe, allowing a focused FWHM of 100 μm (170-μm full diameter). The probe's pulse shape was a 3-ns upward ramp, beginning at $t = 1$ ns and reaching a peak of 150 GW at $t = 4$ ns.

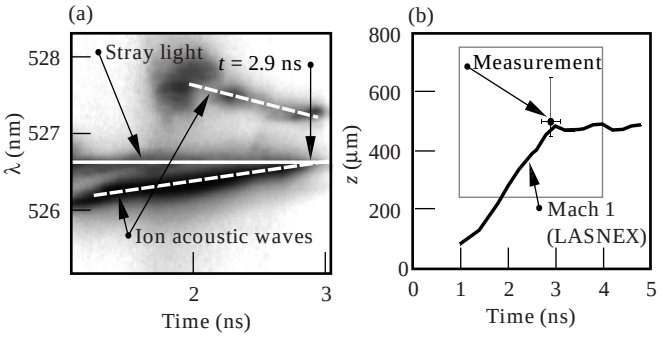

FIGURE 1. (a) Thomson scattering image from a λ = 526.6-nm probe focused at $z = 500$ μm from the original foil position, resolved in wavelength and in time. The upshifted ion acoustic wave feature overlaps the unshifted light at $t = 2.9$ ns, signifying a Mach 1 plasma flow. (b) The LASNEX calculation of the Mach 1 flow location is plotted against time. The measurement from (a) is shown in comparison. The dotted box represents the typical spatial and temporal extent of the crossed beams in the primary experiment. (08-00-0798-1541pb01)

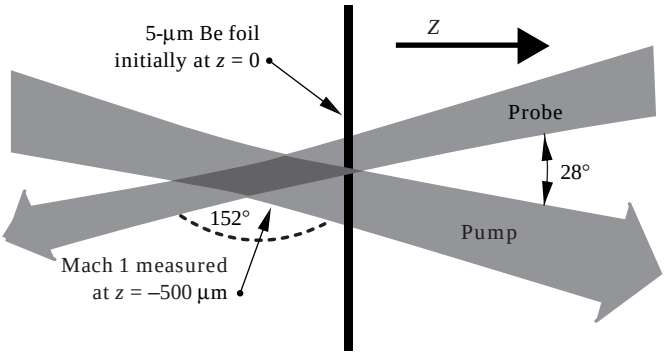

FIGURE 2. The experimental geometry is shown. The 5-μm Be foil is initially at $z = 0$, where z is the normal to the foil in the direction of the "pump" beam propagation. At $t = 0$ ns, two heater beams (not shown) illuminate the foil from both sides. At $t = 1$ ns, the "pump" and "probe" laser beams intersect at a known distance from the foil, at a 152° angle. The diamond-shaped crossing region can have a z-extent of 850 μm to 1300 μm depending on the focal spot sizes, but >75% of the intensity intersects in a region only half this size. (08-00-0798-1542pb01)

Results

The transmission of this probe beam is plotted against time in Figure 3a. With no pump beam present, the transmission of the probe through the exploding foil stabilized at 50–60%. With the addition of the pump beam, crossing the probe at a location $z = -500$ μm, the transmission of the probe increased to near 100% on short time scales. However, when the two beams were crossed at a location $z = -750$ μm, the probe transmission returned to the previous 50–60% level. Because the probe passed through the bulk of the exploding foil plasma before reaching the crossing region, this region had an average intensity ratio I_{pump}/I_{probe} of ~3.

To change this intensity ratio, a KPP was then added to the probe beam, increasing the spot size to 340 μm (full diameter) and raising the average I_{pump}/I_{probe} to ~25. Also, the probe's pulse shape was changed to a 4-ns square pulse, extending from $t = 1$ ns to $t = 5$ ns. The increased size of the probe stretched the z-extent of the diamond-shaped region where the full beams intersected from 850 μm to 1350 μm. The length of the region where >80% of the energy intersected increased from 500 μm to 800 μm.

Figure 3b shows the transmission of this lower-intensity probe beam, both with and without the pump beam. The no-pump transmission was nearly identical to the previous case despite the different pulse shapes, evidence that the low-intensity probe beam was not strongly affecting the plasma. With the pump beam present, the transmission was again increased to ~100% levels when the beams were crossed at $z = -500$ μm; ~80% levels when the beams were crossed at the original foil position ($z = 0$); and no significant transmission enhancement when the beams were crossed at $z = +500$ μm.

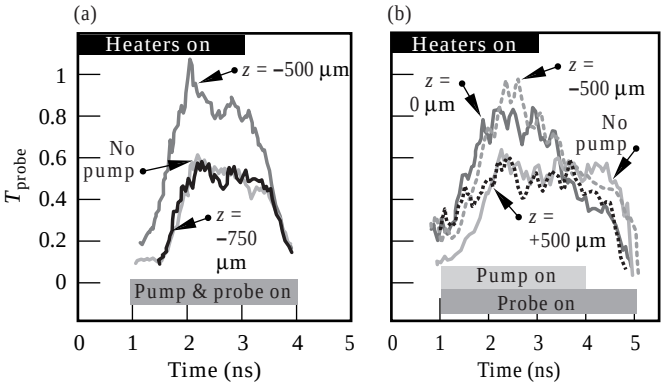

FIGURE 3. (a) Probe transmission fraction (T_{probe}) is plotted against time for a pump / probe intensity ratio of ~3. The light gray solid line is the probe-only (no-pump) condition. The other data shows beam-crossing locations of z = –500 μm (dark gray solid line) and z = – 750 μm (black line). (b) Probe transmission fraction is plotted against time for a pump / probe intensity ratio of ~25. The light gray solid line is the probe-only condition. The other data shows beam-crossing locations of z = –500 μm (dark gray dashed line), z = 0 μm (black solid line), and z = +500 μm (black dashed line). (08-00-0798-1543pb01)

Discussion

Increased transmission of the probe beam in the presence of a pump, however, is not by itself absolute evidence of energy transfer; alternatively, the pump might heat the plasma and thereby decrease the inverse bremsstrahlung absorption of the probe beam. LASNEX simulations show no pump beam effect on the plasma density or Mach 1 location, but do show a higher temperature plasma when the pump is on. This temperature change increases the peak theoretical probe transmission from 60% to 70%, but cannot explain the observed ~100% transmission. In addition, this effect is calculated to occur late in the pump pulse, from $t = 3$ ns onward, rather than the earlier $t = \sim 2$ ns where our peak transmission is observed. Further evidence against this pump-heating scenario includes a measurement of the transmission of the pump beam; it peaks later in time ($t = 3.2$ ns), at a level of 55%, while the amplified probe signal peaks earlier ($t = 2.4$ ns) and with much higher transmission levels. Because the two beams are not exactly colinear, any pump-induced heating should have primarily increased the pump transmission.

For each transmission measurement, a linear gain factor can be computed by simply dividing the crossed-beam transmission by the no-pump transmission. Although the early-time peak gains are large (>3) in both cases where the beams were crossed at z = –500 μm, the corresponding errors are large as well because of the lower no-pump transmission values at these times. A more quantitative gain measurement can be made by averaging the gain over 2 ns < t < 3 ns, the time period when the Mach 1 flow velocity is calculated to be between $z = -300$ μm and $z = -500$ μm. These averages are plotted versus position in Figure 4. The large horizontal error bars represent the extent in the z-axis of the high-intensity diamond-shaped crossing region of the two beams. The maximum gain values of ~1.6 occurred when the crossing region overlapped the Mach 1 region; little gain was observed when the beams were crossed outside this region. This dependence on position is strong evidence of a resonant process.

It is interesting to note that the measured average gain at $z = -500$ μm is roughly the same (~1.6) for both experimental intensity ratios. If the resonant ion wave were saturated, one would expect the gain to increase with increasing I_{pump}/I_{probe}. Our equal gain measurements, however, suggest that this process is not in a saturated regime. This conclusion concurs with previous resonant energy-transfer scaling[8] but is at odds with the near-complete transfer of the pump energy predicted by assuming a linearly driven ion wave in a homogeneous plasma.[12,16]

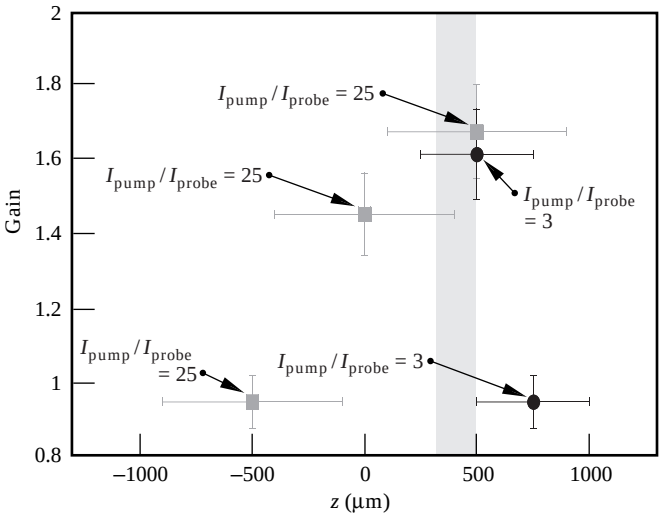

FIGURE 4. The gain factor of the probe beam (averaged from 2 ns < t < 3 ns) is plotted versus position for each crossed-beam location. Circles are for pump / probe intensity ratios of 3; squares are ratios of 25. The large horizontal error bars represent the region over which >80% of the crossed beams overlap. The shaded region represents the calculated Mach 1 location during the 2-ns < t < 3-ns period. (08-00-0798-1544pb01)

One mechanism that could explain the low energy transfer is a spatial degradation of gain due to velocity fluctuations produced by spatially inhomogeneous laser beams.[8,16,23] Laser "hot spots" can also modify the plasma's electron distribution function, creating fluctuations in the ion-acoustic frequency,[24] which could further spatially detune the resonance condition in our experiment. Both of these effects would be enhanced by large-scale filamentation of the pump beam.[25]

Numerical simulations of such plasmas with strong gradients show further reductions of the amplification. BZOHAR, a 2D electromagnetic code that uses particle ions and Boltzmann fluid electrons,[26] has been used to perform simulations of this experiment on small spatial scales.[27] This suggests that the resonant ion waves and the probe amplification saturate after several ion acoustic periods, but the energy gain quickly relaxes (after 40 ps) and becomes nearly proportional to the input probe intensity, as seen in the experiments. BZOHAR arrives at this "linear" condition by means of nonlinear detuning and nonlinear localization of the ion-wave resonance.

Summary

Enhanced transmission of a laser beam has now been observed when it is crossed with a higher-intensity beam of the same frequency in a flowing plasma. Positional and temporal scaling of this effect demonstrates that this is due to a resonance with an ion wave that has zero frequency in the laboratory frame, making this the first observation of steady-state energy transfer between identical frequency laser beams. The observed intensity gain of ~1.6 in two different intensity regimes suggests that the resonant energy transfer is responding linearly to the driving laser beams.

Notes and References

1. N. M. Kroll, A. Ron, and N. Rostoker, *Phys. Rev. Lett.* **13**, 83 (1964).
2. V. N. Tsytovich and A. B. Shvartsburg, *Sov. Phys. Tech. Phys.* **11**, 1431 (1967); L. M. Kovrizhnykh, *Sov. Phys. Tech. Phys.* **11**, 1183 (1967); V. Stefan, B.I. Cohen, and C. Joshi, *Science* **243**, 494 (1989).
3. B. L. Stansfield, R. Nodwell, and J. Meyer, *Phys. Rev. Lett.* **26**, 1219 (1971).
4. T. Tajima and J. M. Dawson, *Phys. Rev. Lett.* **43**, 267 (1979).
5. C. E. Clayton, C. Joshi, C. Darrow, and D. Umstadter, *Phys. Rev. Lett.* **54**, 2342 (1985).
6. C. E. Clayton et al., *Phys. Rev. Lett.* **70**, 37 (1993).
7. C. J. Pawley, H. E. Huey, and N. C. Luhmann, Jr., *Phys. Rev. Lett.* **49**, 877 (1982); C. W. Domier and N. C. Luhmann, Jr., *Phys. Rev. Lett.* **69**, 3499 (1992).
8. R. K. Kirkwood et al., *Phys. Rev. Lett.* **76**, 2065 (1996).
9. D. M. Villeneuve, H. A. Baldis, and J. E. Bernard, *Phys. Rev. Lett.* **59**, 1585 (1987).
10. A. K. Lal et al., *Phys. Rev. Lett.* **78**, 670 (1997).
11. V. V. Eliseev et al., *Phys. Plasmas* **3**, 2215 (1996).
12. C. J. McKinstrie, J. S. Li, R. E. Giacone, and H. X. Vu, *Phys. Plasmas* **3**, 2686 (1996).
13. I. M. Begg and R. A. Cairns, *J. Phys. D* **9**, 2341 (1976).
14. R. W. Short and E. A. Williams, *Phys. Rev. Lett.* **47**, 337 (1981); C. J. Randall, J. R. Albritton, J. J. Thomson, *Phys. Fluids* **24**, 1474 (1981); K. Baumgärtel and K. Sauer, *Phys. Rev. A* **26**, 3031 (1982); R. W. Short and E. A. Williams, *Phys. Fluids* **26**, 2342 (1983).
15. R. K. Kirkwood et al., *Phys. Plasmas* **4**, 1800 (1997); S. H. Glenzer et al., *Phys. Plasmas.*, to be submitted.
16. W. L. Kruer et al., *Phys. Plasmas* **3**, 382 (1996).
17. C. J. McKinstrie et al., *Phys. Rev. E* **55**, 2044 (1997).
18. S. W. Haan et al., *Phys. Plasmas* **2**, 2480 (1995).
19. S. N. Dixit et al., *Optics Lett.* **21**, 1715 (1996).
20. G. Zimmerman and W. Kruer, *Comments Plasma Phys. Controlled Fusion* **2**, 85 (1975).
21. S. Glenzer et al., *Rev. Sci. Instrum.* **68**, 641 (1997).
22. J. D. Moody, et al., *Review of Sci. Instr.* **68**, 1725 (1997).
23. B. B. Afeyan et al., *Bull. Am. Phys. Soc.* **40**, 1822 (1995) and *Phys. Plasmas*, to be submitted; D.S. Montgomery et al., *Phys. Plasmas*, in press (1998).
24. B. B. Afeyan, A. E. Chou, and W. L. Kruer, *ICF Quarterly Report*, Lawrence Livermore National Laboratory, Livermore, CA (1997) and submitted to *Phys. Rev. E*; B. B. Afeyan et al., *Phys. Rev. Lett.*, **80**, 2322 (1998).
25. A. J. Schmitt and B. B. Afeyan, *Phys. Plasmas* **5**, 503 (1998).
26. B. I. Cohen et al., *Phys. Plasmas* **4**, 965 (1997).
27. B. I. Cohen et al., *Phys. of Plasmas* **5**, 3402 (1998).

OBSERVATION OF THE NONLINEAR SATURATION OF LANGMUIR WAVES DRIVEN BY PONDEROMOTIVE FORCE IN A LARGE-SCALE PLASMA

R. K. Kirkwood *D. S. Montgomery***

*B. B. Afeyan** *K. G. Estabrook*

Introduction

The scattering of laser energy by large-amplitude Langmuir waves has long been recognized as an important loss mechanism in laser driven inertial confinement fusion (ICF) research.[1] The scattering waves are driven to large amplitude by the three-wave process of stimulated Raman scattering (SRS), in which the incident electromagnetic wave decays into a Langmuir wave and a scattered wave. Early modeling efforts assumed the three-wave process was limited by simple convective saturation, which results from the propagation of energy out of the interaction volume by the decay waves. In the large-scale plasmas expected in ignition experiments, however, the convective saturation level is sufficiently high that the stimulated Langmuir waves can be saturated at much lower amplitude by nonlinear processes, such as secondary stimulation of ion-acoustic, Langmuir, and electromagnetic waves.[2–6] The primary manifestation of nonlinear saturation is that the Langmuir-wave amplitude can no longer increase linearly with the ponderomotive force, but rather is limited to a lower, saturated level. Previous experiments have found evidence of secondary mechanisms and their effect on SRS.[7–13] More recent experiments have shown that, under conditions similar to what is expected under ignition conditions, the SRS reflectivity is dependent on the damping rate of the ion-acoustic wave,[14–16] consistent with saturation by secondary decay. Further, it has been shown that the scattered SRS spectrum has both a shape[17] and magnitude[14] that are consistent with Langmuir-wave saturation by a secondary decay involving ion waves. However, there was previously no direct observation of the nonlinear response of the Langmuir wave. The potential to observe the Langmuir wave response has been shown by theoretical[18,19] and experimental[13,20–22] studies, in which Langmuir waves and their secondary decay products[23] have been generated by the beating of two laser beams of different frequency. A parallel line of experimentation using beating laser beams to excite ion waves[24,25] has succeeded in demonstrating that the response of the waves to ponderomotive force is linear.

We now report the first demonstration of the nonlinear saturation of Langmuir waves driven by ponderomotive force under conditions relevant to indirect-drive ignition experiments. The Langmuir waves are driven by the beating of two intersecting laser beams of widely disparate frequency. Scattering of energy from the high-frequency beam to the low-frequency beam provides a measure of the wave amplitude, while adjustment of the intensity of the low-frequency beam allows the ponderomotive force to be varied. The amplitude of the Langmuir wave is thus found to be very weakly dependent on the ponderomotive drive when the drive is large, as expected by secondary decay models.[2-6] The experiments are done in low-Z plasmas, which have electron temperatures, densities, and scale length similar to what is expected in indirect-drive ignition experiments[26,27] and which support the interpretation of the observed dependence of SRS reflectivity on the damping rate of the ion-acoustic wave[14,15,16] as due to saturation by secondary decay under these conditions.

Description of the Experiments

The experiments were performed at the ten-beam Nova laser facility, using eight of the beams to preheat a gas-filled target and the remaining two beams as interaction beams. The target consists of a 0.3-μm-thick polyimide bag that is filled with atmospheric pressure gas so that it is nearly spherical, with a radius of 1.3 mm, when placed in the vacuum chamber. The target is preheated

*Polymath Associates, Livermore, CA, and University of Nevada, Reno, Reno, NV
**Los Alamos National Laboratory, Los Alamos, NM

with eight of the $f/4.3$ beams that are defocused (converging) to a diameter of ~1.7 mm. The heater beams each deliver 2.5 kJ at a wavelength of 351 nm in a 1-ns square pulse that produces a plasma that is hot and relatively homogeneous in the region inside a 1-mm radius and during the latter half of the heating pulse (0.5 to 1.0 ns). The target is filled to between 730 and 800 T with a mixture of the following gases: C_3H_8, C_5H_{12}, CH_4, and a 1% Ar impurity to allow for x-ray spectral analysis.[26] The three carbonous gases are mixed in various percentages, which together with small variations in the fill pressure allows the density of electrons to be controlled, thus allowing adjustment of the Langmuir-wave resonance. Application of the heater beams for a duration of 1.0 ns results in a plasma with an electron density approximately that of the initial gas fill (n_0) inside a radius of ~1 mm and an electron temperature that increases to a maximum of ~2.6 keV at 1.0 ns. The electron temperature is determined from x-ray spectral measurements from a region of plasma at $r = 400$ μm, and its peak value is in reasonable agreement with LASNEX simulations.[26]

The remaining two beams are focused in the interior of the plasma and brought to best focus at the same point at $r = 400$ μm, where the plasma is expected to be most uniform. The beams are chosen to cross 25° away from antiparallel, approximating the geometry of SRS backscatter.[27] The pump beam is $f/4.3$ with 2.5 kJ of energy at a wavelength of 351 nm in a 1-ns square pulse that is delayed 0.5 ns with respect to the heaters. The use of a random phase plate (RPP) on the pump beam limits the spot size to 320-μm full width at half maximum (FWHM) at best focus. The probe beam has a wavelength of 527 nm with a variable energy (100 J to 1 kJ) in a 2-ns pulse that is turned on simultaneously with the heaters. The RPP on the probe limits the spot size to 350 μm. This allows the beams to interact in a parallelogram 800 μm on each side with an acute interior angle of 25° as shown in Figure 1. The timing of the beams allows the interaction to occur during the 0.5- to 1.5-ns period. During the first half of this period, the plasma is being heated, while during the second half the plasma is being cooled by radiation and expansion. The transmitted power of the probe beam is collected by a scatter plate of roughened fused silica. The plate is imaged onto a gated optical imager and onto the cathode of a photodiode that provides a measure of the transmitted probe power as a function of time.[28] The response time of the photodiode measurements is improved to 150 ps by deconvolving the measured impulse response of the system.

Measurements of the transmission of the probe beam were performed over a range of plasma densities and compared with the transmission from experiments under the same conditions with no pump beam. The initial density in each experiment was determined by differing gas fill pressures and molecular composition. The initial density was varied from 5.6% to 8.2% of the critical density

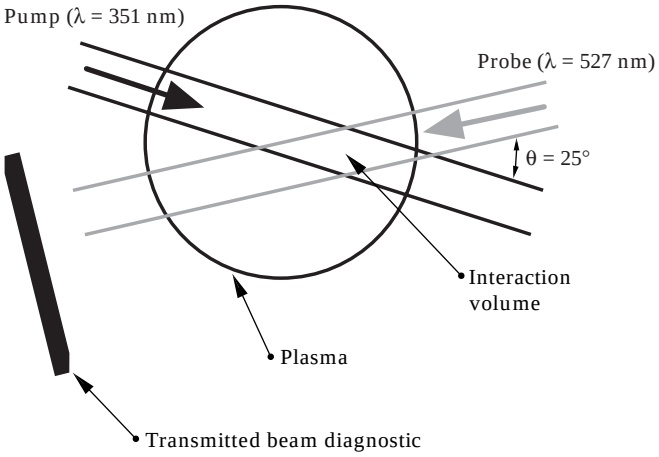

FIGURE 1. Geometry of the crossing beam experiment showing a short wavelength, high-intensity pump beam and a long wavelength, low-intensity probe beam intersecting in a spherical, low-density plasma. The transmitted beam diagnostic measures the time history of the transmitted power of the probe beam. (08-00-0798-1537pb01)

for 351 nm light (n_{c0}), which brackets the Langmuir-wave resonance in this case. The plasma density during the 0.5- to 1.0-ns interaction period is very close to the initial density over this range, as expected from LASNEX simulations[27] and confirmed by the measurements of the peak wavelength of SRS back[27] and forward[28] scattering. The transmitted probe power in the absence of a pump beam (pump-off) was only weakly sensitive to the changes in density, while the transmitted power in the presence of the pump beam (pump-on) was observed to have a substantial enhancement compared to the pump-off case when the initial plasma density was in the vicinity of $n_0/n_{c0} = 7.1\%$. Figure 2 shows the time history of

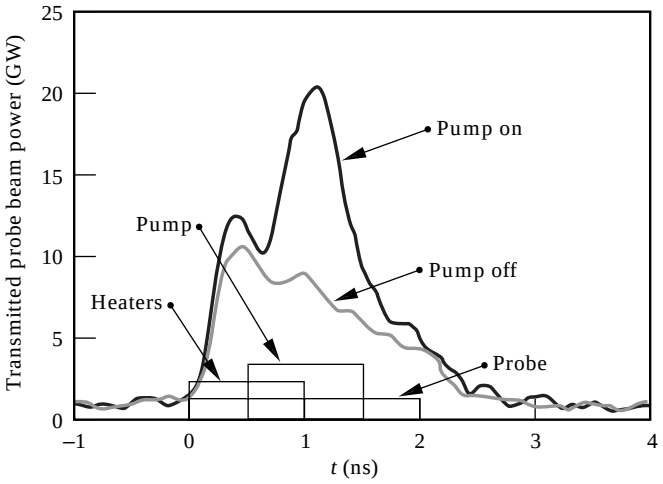

FIGURE 2. Power transmitted through the plasma by the probe beam for the cases with and without a pump beam. The transmission of the probe beam is enhanced by a factor of ≥2 during the period in which the pump is on, indicating that a large amplitude Langmuir wave is being stimulated and is scattering substantial energy. (08-00-0798-1538pb01)

the transmitted probe power near the resonant value of density for both the pump-on and pump-off cases. The observed attenuation of the transmitted beam in the pump-off case is determined primarily by inverse bremsstrahlung absorption and is also affected by scattering, as described in Moody.[28] In the pump-on case, the probe transmission is observed to be strongly enhanced during the 0.5- to 1.5-ns window when both pump and probe are on, indicating that significant energy is transferred from the pump beam. The amplification is measured during the 0.5- to 1.0-ns period by averaging the transmitted power over this period and taking the ratio of the average power in the pump-on case to that in the pump-off case. This amplification is 2.15 (±0.3) for the case shown in Figure 2. Spectral measurements of the transmitted power in the pump-on experiment show a very narrow line width (≤2 nm). The interaction is found to be strongly resonant with plasma density, as observed in the plot of amplification vs n_0 shown in Figure 3. The data in Figure 3 is restricted to the case of low probe-beam power ($P \leq 0.2$ TW), so that the wave response is small and unsaturated. The observation of maximum amplification at 7.1% of the critical density combined with the observation of little or no effect of the pump (amplification ~1) at both higher and lower density in Figure 3 are consistent with the calculated Langmuir-wave resonance for a plasma with an electron temperature of 2.1 keV, which is somewhat lower than the peak value[26] and is consistent with the average temperature measured during the 0.5- to 1.0-ns period. The data in Figure 3 supports the interpretation that the amplification is due to a resonant three-wave interaction of the two beams with a Langmuir wave in the plasma.

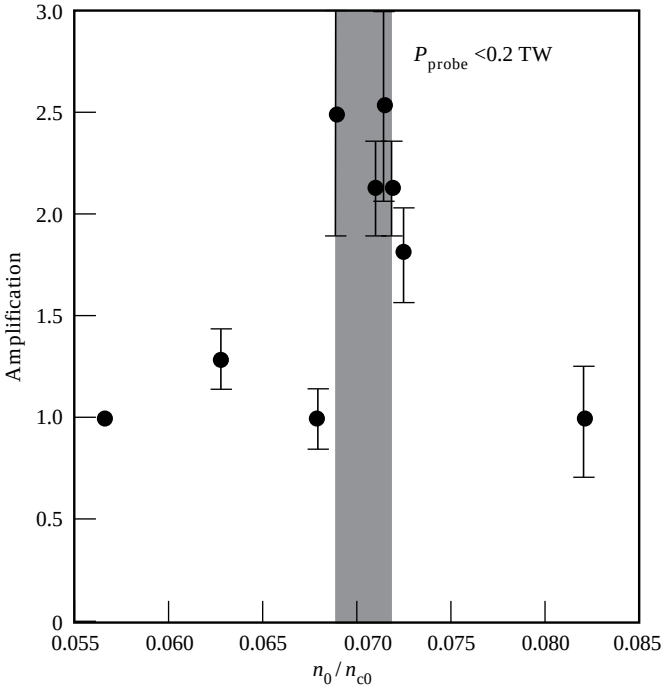

FIGURE 3. The amplification measured during the 0.5- to 1.0-ns period shown as a function of the initial plasma density for the case of low probe intensity and strong ion-acoustic wave damping (i.e., unsaturated Langmuir waves). A maximum is observed at $n_0 / n_{c0} = 7.1$ (±0.15%) (shaded), consistent with the Langmuir resonance. (08-00-0798-1539pb01)

Having identified a density resonant with the Langmuir wave in this experiment ($n / n_c = 7.1\%$) and determined the magnitude of the amplification when the Langmuir-wave amplitude is small, we performed experiments to investigate the nonlinear response of Langmuir waves at larger amplitudes by increasing the probe-beam intensity. These experiments show that the amplification is substantially reduced by increasing the probe intensity, while holding the plasma density close to the resonant value (i.e., within the shaded region in Figure 3). For example, the amplification observed at low probe power (65 GW) under the conditions of Figure 2 is 2.5 ± 0.5, while the amplification in a similar experiment with a probe power of 500 GW is less than 1.32 ± 0.12 (where 1.0 represents no resonance). The nonlinearity is not due to the transmission diagnostic, which has been calibrated and found to be linear with up to an order-of-magnitude-higher transmitted power.[28] These observations are used to demonstrate the saturation of the Langmuir wave by interpreting the enhancement of the probe beam as a measurement of the Langmuir-wave amplitude and the product of the incident intensities of the probe and pump beams as the ponderomotive force that drives the Langmuir wave. This analysis can be understood by considering the total power scattered from the pump beam rather than the amplification of the probe. The power scattered from the pump is determined as the difference between the transmitted probe power with the pump on and with the pump off, again averaging over the 0.5- to 1.0-ns period when all the beams are on. This scattered power is corrected for absorption between the point of scattering (where the center of the beams cross) and the outer edge of the plasma and is plotted vs the incident probe power with the pump power constant in Figure 4. Because the power scattered by the Langmuir wave is proportional to the square of its amplitude δn^2, and because the probe-beam intensity is proportional to the square of the ponderomotive force driving the Langmuir wave, a linear Langmuir wave response would be represented by data that parallels the linear scaling curve shown as a black line in Figure 4. Clearly, the scattered power falls below the linear scaling when the probe power is greater than 200 GW, demonstrating that the Langmuir-wave amplitude is nonlinearly saturated at high ponderomotive drive. This observation of the nonlinearly saturated response of the Langmuir wave to the ponderomotive force produced by the beating of

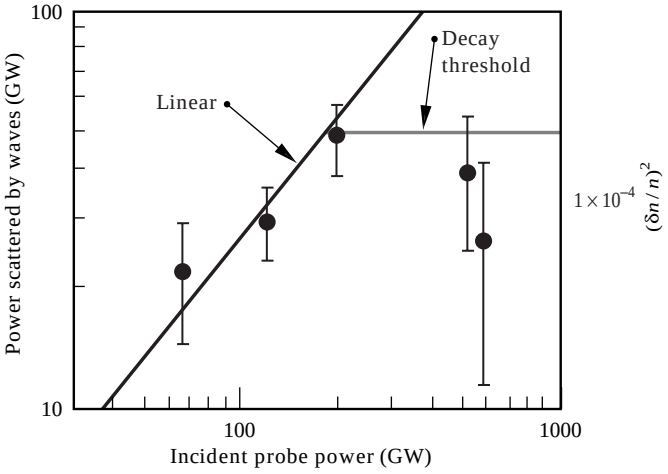

FIGURE 4. The additional power scattered into the probe beam (scattered power) when the pump beam is present and the density is resonant, plotted vs the incident power in the probe. The black line represents a linear relationship between the amplitude of the scattering Langmuir wave and the probe power (ponderomotive force), which is fit to the data for low probe power. The data at high probe power is below the linear scaling (i.e., saturated). The scattered power is interpreted as Langmuir-wave amplitude, and the gray line represents the threshold of the secondary decay instability, as discussed in the text. (08-00-0798-1540pb01)

the two laser beams is the primary result of this article. Such a nonlinearity may be created by many mechanisms, ranging from nonlinear Landau damping, to the relativistic detuning that has been studied in high-phase-velocity plasma waves,[21] to the secondary decay of the Langmuir wave[2-6] and as such is consistent with previous interpretations of data from ignition-relevant plasmas that suggest that SRS backscatter is limited by saturation by secondary decays involving ion waves.[14,15]

The structure of the spectrum of transmitted light and scattering waves was studied in a further set of experiments. These experiments studied the interaction of the two beams during the 1.15- to 1.5-ns period, after the heater beams shut off, to eliminate spectral contributions from heater side scatter. The transmitted probe beam was analyzed by a high-resolution spectrometer for cases corresponding to incident probe powers of 50, 200, and 450 GW in Figure 4. In all cases the spectrum was less than 0.6-nm FWHM, corresponding to a Langmuir-wave spectrum with a width of $\Delta\omega/\omega = 5 \times 10^{-3}$. Amplification of the probe beam was clearly observed in the lowest-power experiment and diminished in higher-power experiments. This is consistent with the early time measurements of Figure 4. This data cannot be directly compared with the data in Figure 4, however, because the absence of heaters during this period makes the plasma conditions and their time dependence different than during the early period. The observed Langmuir-wave spectrum is much narrower than expected for a cascade of multiple Langmuir decay instabilities (LDIs), indicating that if such a cascade is present, it involves very little energy. Because of the geometry and wavelength of the measurements, the transmitted spectrum provides information only about Langmuir waves that are copropagating with the primary Langmuir wave, and it may be consistent with either saturation by a single Langmuir decay producing a counterpropagating wave[8,9] or with saturation by the electromagnetic decay instability (EDI) in which the decay products are not Langmuir waves.

Comparison with Secondary Decay Model

A comparison of the observations with theories of secondary decay of the Langmuir wave[2–6] can be made by estimating the amplitude of the waves from the fraction of power they scatter from the pump beam. Such an estimate is made using a 1D, Bragg wave scattering model for a homogeneous beam,[14,29] which gives an estimate of the scattering wave amplitude. This model gives the relationship between the fraction of pump power scattered F and the wave amplitude $(\delta n / n)$ in terms of the normalized plasma density, the incident-beam wave number, and two characteristic lengths (the system size L and the correlation length of the Langmuir waves $\Delta k)^{-1}$.

$$F \approx \frac{1}{4}\left(\frac{n}{n_{c_0}}\right)^2 k_0{}^2 L(\Delta k)^{-1}\left(\frac{\delta n}{n}\right)^2 \qquad (1)$$

As an estimate of the correlation length, we use the correlation length of the driving ponderomotive force produced by the two $f/4.3$ beams. The width of the spectrum of $k_z = (\mathbf{k}_1 - \mathbf{k}_2)\cdot\hat{z}$ is the speckle length projected into the axis of the beam ($\hat{z}$). We use this width of the k_z spectrum of the incident beams as an estimate of the correlation length of the Langmuir waves: $\Delta k \approx 1.2 \times 10^6$ m^{-1}. Using this length and the experimental plasma parameters in Eq. 1, we estimate the amplitude of the scattering Langmuir wave from the measurements of the fraction of pump-beam power that the wave scatters, as shown on the right axis in Figure 4. This fraction is calculated using the pump-beam power determined from the incident power and a correction for inverse bremsstrahlung between the plasma edge and the point at which the centers of the two beams cross. The results are compared with the threshold for the secondary decay instability, shown as the gray line in Figure 4. The threshold is determined by the damping rates of the secondary decay products and

can be written in terms of the Langmuir-wave amplitude as

$$\left(\frac{\delta n}{n}\right) = 4\, k_L \lambda_D \left(\frac{\nu_{ia}}{\omega_{ia}}\right)^{1/2} \left(\frac{\nu_3}{\omega_3}\right)^{1/2} \qquad (2)$$

where k_L is the wave number of the primary Langmuir wave driven by the beating of the two beams, λ_D is the Debye length, ω_{ia} and ν_{ia} are the real and imaginary parts of the frequency of the ion-acoustic decay product ($\nu_{ia}/\omega_{ia} \approx 0.2$ for a $T_{ion}/T_e \approx 0.15$ as determined by simulations for this case[30]), and ω_3 and ν_3 represent the frequency of the third wave.

When the instability is EDI, the third wave is an electromagnetic wave,[6] and ω_3 and ν_3 are approximately the plasma frequency and the inverse bremsstrahlung absorption rate. When the instability is LDI, the third wave is a Langmuir wave, and ω_3 and ν_3 are approximately the plasma frequency and the electron Landau damping rate. Electrons are produced in these plasmas by mechanisms such as collisional absorption of the beams, nonlinear Landau damping of the Langmuir waves, and nonlocal heat transport.[31] Recent analysis of the non-Maxwellian velocity distribution of such electrons has shown that the electron Landau damping rate may be much lower than in a Maxwellian plasma. In a laser hot spot the damping rate could be reduced by an order of magnitude, approaching the collisional damping rate as a lower limit. As a result, a necessary condition for the presence of EDI or LDI in a non-Maxwellian plasma is that the $\delta n/n$ estimated from the measured scattered power (points in Figure 4) be greater than or equal to the threshold given by Eq. 2 evaluated with ω_3 and ν_3 equal to the plasma frequency and the collisional damping rate (gray line in Figure 4). This threshold is found to be close to the observed saturation level in Figure 4. This is consistent with previous interpretations[2–6, 14–16] that the Langmuir wave is saturated by a secondary decay process involving ion waves.

Conclusion

We have developed a technique to study the properties of Langmuir waves in ignition-relevant plasmas and used this technique to demonstrate that the response of Langmuir waves to ponderomotive force is nonlinearly saturated consistent with earlier studies of SRS.[14,15]

Acknowledgments

The authors gratefully acknowledge conversations with D. F. DuBois (Los Alamos National Laboratory) and W. Rozmus (University of Alberta) on the nature of EDIs and LDIs, as well as with T. Johnston (INRS). This work was performed with support from the Science Use of Nova program.

Notes and References

1. See for example W. L. Kruer, *The Physics of Laser Plasma Interactions* (Addison-Wesley Publishing Co., Redwood City, CA, 1988).
2. S. J. Karttunen, *Plasma Physics* **22**, 151 (1980).
3. G. Bonnaud, Denis Pesme, and Rene Pellat, *Phys. Fluids B* **2**, 1618 (1990).
4. B. Bezzerides, D. F. Dubois, and H. A. Rose, *Phys. Rev. Lett.* **70**, 2569 (1993).
5. T. Kolber, W. Rozmus, and V. T. Tikhonchuk, *Phys. Fluids B* **5**, 138 (1993).
6. K. L. Baker, Ph.D. Dissertation, University of California, Davis, 1996; see also P. K. Shukla et al., *Phys Rev. A* **27**, 552 (1983).
7. D. M. Villeneuve et al., *Phys. Rev. Lett.* **71**, 368 (1993).
8. K. L. Baker et al., *Phys. Rev. Lett.* **77**, 67 (1996).
9. C. Labaune et al., *Phys. of Plasmas* **5**, 234 (1998).
10. C. J. Walsh, D. M. Villeneuve, and H. A. Baldis, *Phys. Rev. Lett.* **53**, 1445 (1984).
11. H. A. Baldis et al., *Phys. Rev. Lett.* **62**, 2829 (1989).
12. D. S. Montgomery et al., submitted to *Phys. Rev. Lett.*
13. D. Umstadter, W. B. Mori, and C. Joshi, *Phys. Fluids B* **1**, 183 (1989).
14. R. K. Kirkwood et al., *Phys. Rev. Lett.* **77**, 2706 (1996).
15. J. C. Fernandez et al., *Phys. Rev. Lett.* **77**, 2702 (1996).
16. R. K. Kirkwood et al., *Physics of Plasmas* **4**, 1800 (1997).
17. R. P. Drake and S. H. Batha, *Phys. of Fluids B* **3**, 2936 (1991).
18. N. Kroll, A. Ron, and N. Rostoker, *Phys. Rev. Lett.* **13**, 83 (1964).
19. A. N. Kaufman and B. I. Cohen, *Phys. Rev. Lett.* **30**, 1306 (1973).
20. B. L. Stansfield, R. Nodwell and J. Meyer, *Phys. Rev. Lett.* **26**, 1219 (1971).
21. C. E. Clayton, C. Joshi, C. Darrow, and D. Umstadter, *Phys. Rev. Lett.* **54**, 2343 (1985).
22. C. Darrow et al., *Phys. Rev. Lett.* **56**, 2629 (1986).
23. F. Amiranoff et al., *Phys. Rev. Lett.* **68**, 3710 (1992).
24. R. K. Kirkwood et al., *Phys. Rev. Lett* **. 77**, 2065 (1996); and *ICF Quarterly Report* **6**(2), Lawrence Livermore National Laboratory, Livermore, CA (UCRL-LR-105821-96-2).
25. W. L. Kruer, B. B. Afeyan, S. C. Wilks, and R. K. Kirkwood, *Physics of Plasmas* **3**, 382 (1996).
26. S. H. Glenzer et al., *Phys. Rev. E* **55**, 927 (1997).
27. B. J. MacGowan et al., *Physics of Plasmas* **3**, 2029 (1996).
28. J. D. Moody et al., *Rev. Sci. Inst.* **68**, 1725 (1997).
29. T. Kolber, W. Rozmus, and V. T. Tikhonchuk, *Phys. Plasmas* **2**, 256 (1995).
30. E. A. Williams et al., *Physics of Plasmas* **2**, 129 (1995).
31. B. B. Afeyan et al., *Phy. Rev. Lett.* **80**, 2322 (1998), and elsewhere in this volume.

HYBRID PARTICLE-IN-CELL SIMULATIONS OF STIMULATED BRILLOUIN SCATTERING INCLUDING ION–ION COLLISIONS

P. W. Rambo

S. C. Wilks

W. L. Kruer

Introduction

Stimulated Brillouin scattering (SBS) is an instability in which intense laser light incident on a target can decay into a scattered light wave and an ion sound wave. The process requires frequency and wave vector matching (i.e., $\omega_0 = \omega_{sc} + \omega_i$ and $\mathbf{k}_0 = \mathbf{k}_{sc} + \mathbf{k}_i$), which corresponds to energy and momentum conservation. Here ω_0 (ω_{sc}) is the frequency of the incident (scattered) light wave; ω_i is the frequency of a sound wave in the plasma; and $\mathbf{k}_0$, $\mathbf{k}_{sc}$, $\mathbf{k}_i$ are the corresponding wave vectors. It is important to understand and control this instability to optimize energy deposition in inertial fusion targets.

Although there has been much progress in characterizing SBS in experiments,[1,2] a better understanding of the nonlinear behavior is clearly needed. The nonlinear behavior of the ion wave is particularly complex. Collisionless particle-in-cell (PIC) simulations[3–7] have emphasized strong distortions in the ion distribution function near the ion wave phase velocity. The damping and dispersion of the driven ion wave are then determined by nonlinear processes, such as trapping, self-consistent tail formation, and mode coupling. It should be emphasized that the distributions are modified quite rapidly even when the driven ion wave has a rather small amplitude. A characteristic time for the ion distribution to distort is $\tau_b = \pi/\omega_b$, where ω_b is the bounce frequency of a resonant ion in the potential trough of the ion wave. Here $\omega_b = (ZeEk_i/M)^{1/2}$, where E is the electric field, k_i the wave number, Z the ion charge state, and M its mass. For even a very small ion wave amplitude corresponding to a fluctuating density $\delta n/n \approx 1\%$, the bounce time is only about 1 ps in typical experiments using 0.35-μm lasers.

It is readily seen that ion–ion collisions can strongly reduce these distortions of the ion distribution function, especially in high-Z plasmas found in laser-irradiated hohlraums. The scattering rate of an ion at the phase velocity [approximated as the sound speed, $C_s \equiv (ZT_e/M)^{1/2}$] is

$$\nu_\perp = \frac{6\sqrt{\pi}}{(ZT_e/T_i)^{3/2}}\tau_i^{-1} \quad , \tag{1}$$

where T_e (T_i) is the electron (ion) temperature and τ_i is the Braginskii ion–ion collision time

$$\tau_i \equiv \frac{3\sqrt{M}\,T_i^{3/2}}{4\sqrt{\pi}\,Z^4 e^4 n_i \lambda_{ii}} \quad . \tag{2}$$

Here, n_i is the ion number density and λ_{ii} is the Coulomb logarithm for ion–ion collisions. The time required for collisions to restore the distribution is determined by the trapping width ($\delta v_{trap} \approx 2\omega_b/k_i$) and $\nu_\perp$:

$$\tau_{detrap} \approx \frac{2}{\nu_\perp}\left(\frac{\delta v_{trap}}{C_s}\right) \approx \frac{4}{\nu_\perp}\left(\frac{\delta n}{n}\right)^{1/2} \quad . \tag{3}$$

These arguments are easily generalized to the case of a plasma composed of a light minority species (α) and a heavy species (β).

In the following example, Be is added to a Au plasma[8] to increase the Landau damping of the ion waves. For an equal mixture Au^{+50}/Be^{+4} plasma, with electron temperature $T_e = 3$ keV, $\delta n/n = 0.05$, electron plasma density $n_e = n_c/4$ (n_c = critical density), and $k_i = 3.5 \times 10^5/\text{cm}^1$ ($\approx 2k_0$ for blue laser light): $\tau_{detrap} \approx \tau_{bounce} \approx 1$ ps. Similar results can be estimated for recent gas bag experiments with Xe/H mixtures.[9]

In addition to countering and/or modifying tail formation in the nonlinear state, ion–ion collisions can inhibit the transport of heated ions from the interaction region. (In collisionless simulations, they simply free-stream away.) The reduced transport enhances the local

ion heating, which can reduce the instability growth. Such an effect will be particularly important on long time scales, when significant energy has been transferred via the driven ion waves.

Hybrid Simulation Model

Hybrid simulations, which model some physical species with particles and others with fluids, have been applied to a wide variety of problems in magnetically confined fusion plasmas and space plasma physics. Typically, the regime of interest is such that the ions are essentially collisionless and require a kinetic treatment, while the electrons may be represented by a fluid. More recently, such simulation models are being applied to laser-generated plasmas.[4–7] Our simulations are performed in one spatial dimension, using a PIC description for the kinetic ions and an isothermal electron fluid at constant temperature T_e. The particle ion velocities and positions are simply advanced by

$$\frac{dx}{dt} = v_x \ , \quad \frac{dv_x}{dt} = \frac{ZeE_x}{M} \ , \tag{4}$$

using the longitudinal electric field $E_x = -\partial\Phi/\partial x$. The electrostatic potential Φ is found from solution of the nonlinear Poisson equation in terms of the total ion charge density and the electron density (n_e) given by a Boltzmann relation,

$$-\partial^2\Phi/\partial x^2 = 4\pi e\left(\Sigma_i Z_i n_i - n_e\right);$$
$$n_e \equiv n_0 \exp\left\{e\left(\Phi - \Phi_{\text{pond}}\right)/T_e\right\} \ . \tag{5}$$

The use of a reduced treatment for the electrons enables efficient simulation of longer time scales; in particular, the restriction of resolving the electron plasma frequency is relaxed. The ponderomotive potential $\Phi_{\text{pond}} = m_e\left\langle u_y^2\right\rangle/2$ is accumulated in time during the explicit advance of the electromagnetic field equations and transverse electron fluid velocity (u_y), which are subcycled in time relative to the ion particle advance. Use of the nonlinear Poisson equation retains the physics of charge separation due to finite-electron Debye length, and hence includes modifications to the ion-acoustic dispersion relation embodied in the linear dispersion relation $\left(w/kC_s\right)^2 = \left(1 + k^2\lambda_{De}^2\right)^{-1}$, where $\lambda_{De} = (4\pi n_e e^2/T_e)^{-1/2}$ is the Debye length.

Although for the parameters considered here the dispersive effect of finite $k\lambda_{De}$ is small, the smoothing achieved is beneficial in reducing numerical heating, a major concern for these high ZT_e/T_i plasmas.[10]

Additionally, we use quadratic splines to interpolate between particles and grid and large numbers of particles per cell, typically 200 to 400 for each ion species. The use of quadratic splines reduces numerical heating approximately an order of magnitude compared to linear interpolation.

Ion–ion collisions between particles are handled using a scheme substantially like that developed by Takizuka and Abe.[11] Particles sharing the same spatial cell are randomly paired up and then undergo a collision irrespective of their positions in the cell. Each collision is kinematically correct, thus ensuring microscopic momentum and energy conservation. For scattering between species α and β, the collision is performed in the center of mass frame for each particle pair with a polar scattering angle picked from a Gaussian distribution of width,

$$\left\langle\theta^2\right\rangle \equiv \frac{8\pi Z_\alpha^2 Z_\beta^2 e^4 \lambda_{\alpha\beta} n_\beta}{m_{\alpha\beta}^2 |\delta\mathbf{v}|^3}\delta t \ , \tag{6}$$

where $m_{\alpha\beta} = m_\alpha m_\beta/(m_\alpha + m_\beta)$ is the reduced mass and $\delta\mathbf{v}$ is the relative velocity between each scattering pair. The collisional time period δt is typically equal to the particle advance time step Δt or a small multiple of it. The azimuthal scattering angle is picked uniformly over the interval $[0, 2\pi]$. The postcollision velocity of the particle from species β is given by the kinematic relations. The Coulomb logarithm $\lambda_{\alpha\beta}$ is set to a constant in these simulations and provides a convenient multiplier to vary the collisionality. Extensive tests have verified that this method is equivalent to a Fokker–Planck description of cumulative small-angle Coulomb scattering. In the multispecies simulations performed here, typically only the light–heavy species (α–β) collisions were included. The rate of collisions between light ions (α–α) is typically low enough to ignore, while the heavy–heavy (β–β) collisions also contribute little to wave damping. In fact, failure to properly resolve the short collisional scales for heavy–heavy collisions can artificially enhance the wave damping rate.

Wave Damping

As a simple illustrative example of the relevant physics, we first consider the damping of a finite-amplitude ion wave composed of a mixture of light and heavy ions. The linear damping of such a mixed-species plasma has been discussed by several authors, both with[12,13] and without[14] collisions. Consider the Au/Be plasma previously discussed. We can estimate the ion Landau damping in the absence of collisions to be approximately $\gamma_i \approx 0.07\omega_i$. Figure 1a shows the time history of the electron fluid velocity from a simulation of a single wavelength, initially with amplitude

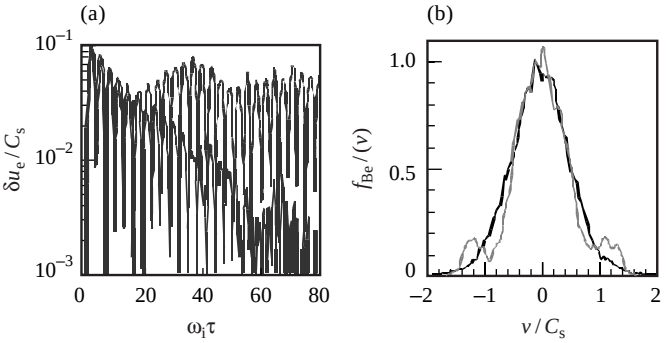

FIGURE 1. Damping of a small-amplitude wave in a Be / Au plasma: (a) time history of electron fluid velocity and (b) velocity distribution of Be ions for collisionless (gray line) and collisional (black line) simulations. (50-00-0898-1711pb01)

perturbation $\delta n/n = 0.05$. (Because the plasma is initialized as a standing wave, the total initial ion density perturbation is the sum of left- and right-going waves, $2\delta n/n = 0.10$). We can clearly see the initial linear decay with $\gamma_i \approx 0.07\omega_i$, followed by a recurrence due to nonlinear trapping; this occurs at time $t \approx 1$ ps $\approx \tau_b$. The ion velocity distribution is presented in Figure 1b, clearly showing the nonlinear distortion near the phase velocity of the ion wave. In contrast, a simulation including ion–ion collisions between the Au and Be particles is also shown, which displays steady linear damping.

It is important to note that the linear damping rate is unaffected by this level of collisions ($\lambda_{\alpha\beta} = 2$). This is consistent with estimates for the amount of damping contributed by frictional and viscous effects caused by collisions, $\gamma_{collision} \approx 5 \times 10^{-3}\ \omega_i << \gamma_{Landau.}$[13] Increasing or decreasing the collisionality by a factor of two was observed to have essentially no effect, either on the linear damping rate or the supression of trapping. Significantly decreasing the collision rate eventually returns to the collisionless result of nonlinear trapping; significantly increasing the collisionality eventually suppresses Landau damping, and the wave damping rate is observed to monotonically decrease with further increases in collisionality. (Much like the situation of a single-ion species,[15] a mixture with reduced ion Landau damping, e.g., $T_e / T_i = 8$, exhibits a maximum in the wave damping for $\nu_{\alpha\beta} \approx \omega_i$, where $\nu_{\alpha\beta}$ is the generalization of Branginskii's collision time for multiple species[13]).

Self-Consistently Driven Ion Waves

We now consider a case with ion waves self-consistently driven by SBS. The system is a finite-length plasma slab composed of the same Au / Be plasma just considered, with laser light (wavelength $\lambda_0 = 0.35$ μm) of intensity $I_0 = 4.0 \times 10^{15}$ W / cm^2, incident from the left-hand side. The plasma slab is composed of an active plasma region (represented by particles) $L = 11$ μm, buffered between fixed ion regions; the fixed ions prevent plasma expansion driven by the ambipolar field at the slab edges, which have linear density ramps to minimize reflection. The density profile is shown in Figure 2a for a collisionless case, illustrating the geometry as well as showing the strong ion wave fluctuations present in this case due to SBS. The time-dependent reflectivity is presented in Figure 2b; note that it reaches a very high level, $R \approx$ 80%. Inspection of the ion velocity phase space shows trapping of resonant ions in the large-amplitude waves, $\delta n/n \approx$ 15–20%. For comparison, an identical case except for ion–ion collisions ($\lambda_{\alpha\beta} = 2$) is also presented that shows a significant decrease in the saturated reflectivity $R < 1$%. For this case, the instability saturates at a much lower level, $\delta n/n \approx$ 2–3%, and although the ion velocity distribution shows strong heating, the slope of the distribution is observed to still be monotonic. We note that a reduction in the reflection is one effect in the right direction, because collisionless simulations have typically predicted too much reflectivity from large regions of plasma.

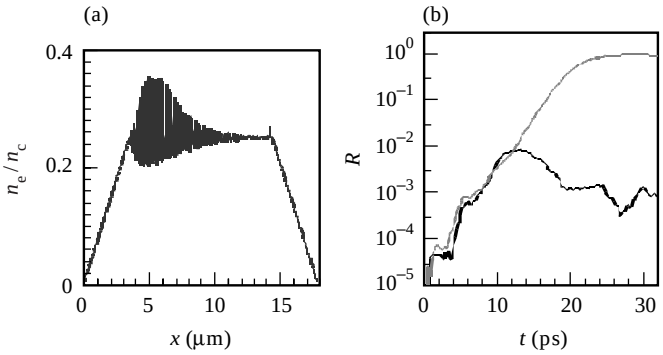

FIGURE 2. Simulations of SBS in a Be / Au plasma: (a) electron density from a collisionless simulation and (b) time-dependent reflectivities from collisionless (gray line) and collisional (black line) simulations. (50-00-0898-1712pb01)

The saturated ion wave amplitude for the collisional case is consistent with our earlier estimates of the level below which collisions can repopulate the resonant region and counteract trapping. The collision rate necessary to maintain wave damping depends on the strength of the instability driving the ion waves. This is illustrated by a set of simulations presented in Figure 3 for a fully ionized CH plasma (1:1, $n_e = n_c / 4$, $T_e = 10T_i = 3$ keV, $L = 22$ μm). In Figure 3a, the time-dependent reflectivity for an incident intensity of $I_0 = 2.7 \times 10^{15}$ W / cm^2 is compared for a collisionless simulation and three collisional runs employing half, nominal, and double

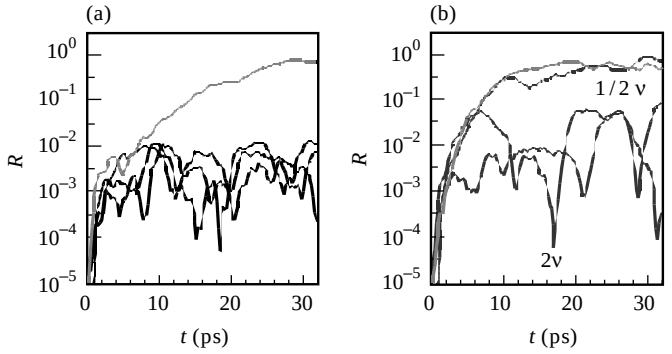

FIGURE 3. Time-dependent SBS reflectivities for CH plasma comparing collisionless (gray line) and collisional (black lines) simulations for intensity (a) $I_0 = 2.7 \times 10^{15}$ W/cm^2 and (b) $I_0 = 3.4 \times 10^{15}$ W/cm^2; three collisional runs employ nominal, half, and double collisionality. (50-00-0898-1713pb01)

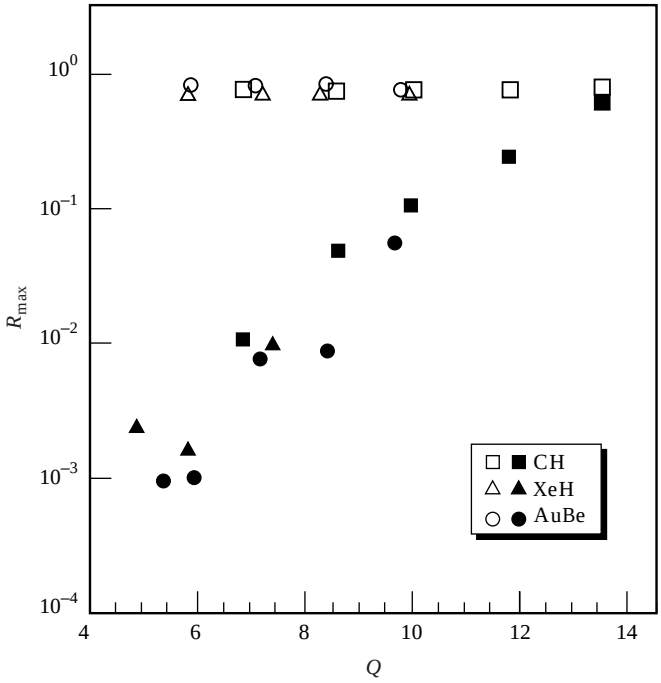

FIGURE 4. Maximum reflectivity observed in simulations of SBS with and without collisions as a function of the linear gain exponent; closed and open symbols are collisional and collisionless results, respectively. (50-00-0898-1725pb01)

collisionality ($\lambda_{\alpha\beta}$ = 2, 4, and 8 respectively); all the collisional runs are similar with peak reflectivity $R \approx 1\%$. A similar insensitivity was found for the Au/Be plasma case previously described. In contrast, increasing the incident pump strength to $I_0 = 3.4 \times 10^{15}$ W/cm^2, as shown in Figure 3b, drives the ion waves strongly enough that the case with collisionality halved now nearly follows the collisionless result. If the collision rate is significantly increased, however, the wave damping is decreased, increasing the linear gain and increasing the reflectivity. An additional simulation at $I_0 = 3.4 \times 10^{15}$ W/cm^2 with collisionality increased by a factor of thirty clearly showed faster instability growth, consistent with the decreased damping ($\gamma_i/\omega_i \approx 0.06$ measured in a linear wave damping test). In spite of this, the saturated reflectivity ($R \approx 10\%$) was still lower than the collisionless result.

A number of self-consistent SBS simulations are summarized in Figure 4, which shows peak reflectivity as a function of the linear gain exponent

$$Q \equiv \frac{\pi}{4}\left(\frac{L}{\lambda_0}\right)\left(\frac{n_e/n_c}{1-n_e/n_c}\right)\left(\frac{v_0}{v_e}\right)^2\left(\frac{\gamma_i}{\omega_i}\right)^{-1}, \qquad (7)$$

where v_0/v_e is the ratio of an electron's quiver velocity in the pump laser field to its thermal velocity. In all the simulations, the electron parameters were $n_e = n_c/4$ and T_e = 3 keV. We see that the collisionless reflectivities are all very large and only weakly dependent on the gain. In contrast, the simulations including ion–ion collisions more nearly follow an exponential gain relationship, $R \approx R_0 \exp(Q)$, until the gain is large enough to drive the ion wave amplitude beyond the level where collisions keep pace with the trapping. In addition to the Au^{+50}/Be^{+4} and C^{+6}/H^+ plasmas, simulations are also shown for a Xe^{+44}/H^+ mixture (1:4, $T_e = 2T_i$, $\lambda_{\alpha\beta} = 2$, L = 11 μm) with similar behavior. This Xe/H plasma differs fundamentally in that the resonant ion wave is the slow mode, with phase velocity smaller than the proton thermal velocity. Simulations of the damping of small amplitude waves determined the damping rates used in Eq. 7 to calculate the linear gain, $\gamma_i/\omega_i \approx 0.10$ for the C/H plasma and $\gamma_i/\omega_i \approx 0.05$ for the Xe/H plasma.

In addition to affecting tail formation, ion–ion collisions can inhibit the transport of heated ions from the interaction region. We illustrate this with a simulation of a single-species plasma, Au^{+50} ($n_e = n_c/4$, $T_e = T_i$ = 3 keV, L = 11 μm). The sound speed $C_s = 2.7 \times 10^7$ cm/s is much larger than the ion thermal velocity $v_i = (T_i/m_i)^{1/2} = 3.8 \times 10^6$ cm/s, so that ion Landau damping is very weak. (In fact, no resonant particles are initially present in the simulation.) Because of the large ratio of sound speed to thermal velocity, collisional damping of the wave is also very small, in spite of the large collision rate $\tau_i\omega_i \approx 0.10$. Thus, the reflectivities from two simulations with and without collisions are initially very similar, as shown in Figure 5a. The driven ion waves are very large, so that collisions are slow to repopulate the tail. Collisions are effective, however, in preventing the heated ions from free-streaming out of the simulation as rapidly as occurs in the collisionless case. Figure 5b shows the mean ion energy $\langle \varepsilon_i \rangle$ as a function of position from the collisional simulation at two different times; although not Maxwellian, the ion distribution is fairly isotropic.

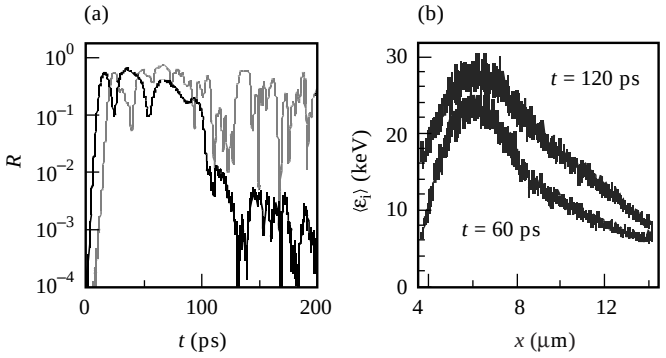

FIGURE 5. Simulations of SBS in a Au plasma showing (a) reflectivities from collisionless (gray line) and collisional (black line) simulations and (b) average ion energy as a function of position from collisional simulation. (50-00-0898-1714pb01)

At late time (t > 100 ps), the mean ion energy exceeds 20 keV for much of the simulation region, and the reflectivity is significantly reduced compared to the collisionless run. This decrease in reflectivity can be interpreted as being due to the increase in linear damping of the ion waves. This increase in linear damping may be due to Landau damping from the nonlinearly populated tails, but is also due to increased collisional damping. Assuming a Maxwellian with $T_i = 15\ \text{keV} \approx 2\left\langle \varepsilon_i \right\rangle / 3$, the collisional wave damping[15] is $\gamma_i / \omega_i \approx 0.04$, and the linear gain exponent of the system is reduced to $Q \approx 7$. The late-time reflectivity is consistent with this reduced gain.

Conclusion

In summary, we have shown the important effect that ion–ion collisions can have on SBS. By restoring the nonlinearly distorted distribution function, damping is maintained closer to the linear value, significantly reducing the reflectivity observed in simulations. The fact that damping is maintained close to the linear value for finite-amplitude ion waves is important to the interpretation of recent experiments,[9,16] which have observed an inverse correlation between stimulated Raman scattering and linear ion wave damping, as well as one important justification for reduced descriptions of coupled parametric processes that assume linear damping. Collisions also modify the ion transport and enhance long-term changes in the plasma conditions, which can disrupt SBS. Although not always important, the collisional effects we have identified should be assessed for each application.

Acknowledgments

The authors wish to acknowledge helpful discussions with R. L. Berger, B. Cohen, A. B. Langdon, and B. Lasinski.

Notes and References

1. H. A. Baldis, E. M. Campbell, and W. L. Kruer, *Physics of Laser Plasmas* (North Holland, Amsterdam, 1991) pp. 361–434, and many references therein.
2. B. J. MacGowan et al., *Phys. Plasmas* **3**, 2029 (1996).
3. D. W. Forslund, J. M. Kindel, and E. L. Lindman, *Phys. Rev. Lett.* **30**, 739 (1973).
4. W. L. Kruer, E. J. Valeo, and K. G. Estabrook, *Phys. Rev. Lett*. **35**, 1076 (1975).
5. S. C. Wilks et al., *Phys. Rev. Lett*. **74**, 5048 (1995).
6. B. I. Cohen, B. F. Lasinski, A. B. Langdon, and E. A. Williams, *Phys. Plasmas* **4**, 956 (1997).
7. H. X. Vu, *J. Comput. Phys*. **124**, 417 (1996).
8. R. K. Kirkwood et al., *Phys. Plasmas* **4**, 1800 (1997).
9. R. K. Kirkwood et al., *Phys. Rev. Lett*. **77**, 2706 (1996).
10. P. W. Rambo, *J. Comput. Phys*. **133**, 173 (1997).
11. T. Takizuka and H. Abe, *J. Comput. Phys*. **25**, 205 (1977).
12. E. M. Epperlein, R. W. Short, and A. Simon, *Phys. Rev. E* **49**, 2480 (1994).
13. V. Yu. Bychenkov, W. Rozmus, and V. T. Tikhonchuk, *Phys. Rev. E* **51**, 1400 (1995).
14. H. X. Vu, J. M. Wallace, and B. Bezzerides, *Phys. Plasmas* **1**, 3542 (1994); E.A. Williams et al., *Phys Plasmas* **2**, 129 (1995).
15. C. J. Randall, *Phys. Fluids* **25**, 2231 (1982); M. D. Tracy et al., *Phys. Fluids B* **5**, 1430 (1993).
16. Juan C. Fernández et al., *Phys. Rev. Lett*. **77**, 2702 (1996).

REDUCTION OF LASER SELF-FOCUSING IN PLASMA BY POLARIZATION SMOOTHING

*E. Lefebvre** *B. J. MacGowan*

R. L. Berger *J. E. Rothenberg*

A. B. Langdon *E. A. Williams*

Introduction

Achievement of inertial confinement fusion with upcoming megajoule-scale laser facilities requires intense laser light to be propagated through thousands of wavelengths of underdense plasma—a situation naturally susceptible to vigorous growth of laser-plasma instabilities. These instabilities affect the propagation of the incident light by absorbing and/or scattering energy; they prevent efficient coupling to the target and can threaten the symmetry of the x-ray drive imposed on the capsule. The eventual result is a reduction of the safety margin included in the design of the facilities. These detrimental processes are most violent in the so-called hot spots of the beam, where the laser intensity is significantly higher than its average value over the focal spot. Moreover, the concentration of energy into the hot spots is itself prone to an unstable phenomenon, known as self-focusing or filamentation.[1–3] In the regions of high laser intensity, the increased thermal electron pressure and the ponderomotive force cooperate to expel the plasma, increasing the refractive index and leading to a still higher intensity. Temporal and spatial smoothing have been observed to significantly reduce both the backscatter[4–6] and filamentation[7] from underdense plasmas. Stimulated Raman and Brillouin backscattering from very low-density plasma, associated with strong filamentation, was virtually eliminated with temporal smoothing.[5,6] Suppressing filamentation is therefore needed to control backscattering instabilities and requires as much beam smoothing as possible.

A number of approaches to smoothing have been proposed for megajoule-class lasers.[8–12] One such approach is to use a random phase plate (RPP)[9] to homogenize the long-scale structure of the focal spot and to then reduce the residual fine-scale speckle within the focal envelope by using the temporal smoothing by spectral dispersion (SSD) method.[10] In this method, the laser pulse is spectrally broadened by phase modulation, and the resulting bandwidth is then angularly dispersed by a diffraction grating so different frequencies produce shifted speckle patterns that average out in the focal plane. From a time domain viewpoint, the speckle pattern in the focal plane changes at a rate determined by the total bandwidth of the modulation, and thus, the time-integrated intensity seen by the plasma is smoothed. If this rate is more rapid than the plasma hydrodynamic response time, then one expects the smoothing method to be effective in reducing self-focusing. However, this rate is bounded by practical limits on the maximum laser bandwidth, and an alternative or complementary smoothing technique is therefore of great interest.

In this article, we present the first calculations of the effect of polarization smoothing (PS) on the filamentation instability. These calculations show that PS by itself is highly effective in controlling filament formation. In addition, it is shown that PS, with unexpected efficacy, can be combined with SSD to provide suppression greater than either smoothing technique can provide alone. Because PS can be implemented in a large laser system without loss of performance and at reasonable cost, it is a smoothing alternative that satisfies the requirements of both laser engineers and inertial fusion target scientists.

Polarization Smoothing in Vacuum

A few simple techniques have been suggested for PS.[11–13] In the implementation examined here, the laser beam is incident upon a wedged birefringent crystal, with its linear polarization at 45° from both the ordinary and extraordinary axes of the crystal.[11] The

*Commissariat à l'Energie Atomique, Bruyères-le-Châtel, France

crystal output then consists of two beams with equal intensities and orthogonal polarizations. Their directions of propagation are separated by an angle α to the wedge θ; the birefringence Δn of the crystal: $\alpha = \theta\Delta n$.[14] Due to their orthogonal polarizations, the two waves do not interfere in the target plane, and the total incident intensity is simply the sum of both intensities. The angular shift between the beams in the near-field translates into a spatial shift at focus: $\Delta x = \alpha L = \alpha f D$, where L and f are the focal length and the f-number of the lens, and D is the width of the beam at the lens. The intensity speckle pattern of one beam at focus has a transverse coherence length of $l_\perp = f\lambda_0$.[15,16] For the sum of the two beams, the intensity statistics are determined by the correlation between the shifted speckle patterns,[15] and hence the displacement Δx. The correlation function, $g(\Delta x)$, is given by the Fourier transform of the near-field beam aperture. In our simulations, the beam is square, and $\Delta x = [\sin(\pi\Delta x/f\lambda_0)]/(\pi\Delta x/f\lambda_0)$. It is straightforward to determine the intensity distribution function for a finite displacement, x, between the patterns. The probability $P(I)dI$ that the total intensity lies in the interval, I to $I + dI$, is given by

$$P(I) = \frac{4I}{I_0^2(1-g^2)} \exp\left[\frac{-2I}{I_0(1-g^2)}\right] \int_0^1 ds I_0\left(\frac{gI\sqrt{1-s^2}}{I_0(1-g^2)}\right) . \quad (1)$$

The function I_0 is the modified Bessel function of zeroth order. If the separation between the two beams is much smaller than the transverse coherence length of one of them, $\Delta x \ll l_\perp$, the intensity statistics in vacuum have the exponential distribution of a single beam; the probability $P_1(I)dI$ that the total intensity lies in the interval, I to $I + dI$, is given by $P_1(I) = \exp(-I/I_0)/I_0$, where I_0 is the total average intensity.[15] An elementary calculation then shows that the fraction of beam energy contained in regions where the intensity is higher than nI_0 is $F_1(n) = (1 + n)\exp(-n)$. Hence, e.g., 4% of the beam energy has a local intensity above $5I_0$. Conversely, if the beams are completely uncorrelated (e.g., a displacement of $f\lambda_0$), $g = 0$, and the intensity distribution is that of the incoherent sum of two speckle patterns governed by $P_2(I) = 4I\exp(-2I/I_0)/I_0^2$. Now the fraction of beam energy above nI_0 reads $F_2(n) = (1 + 2n + 2n^2)\exp(-2n)$, and is less than 0.3% for $n = 5$. The intensity contrast, defined as

$$\sigma = \sqrt{\frac{\langle I^2 \rangle}{I_0^2} - 1} ,$$

is reduced from 1 for one RPP beam to $1/\sqrt{2}$ for the superposition of two uncorrelated beams,[15] indicating a smoother intensity distribution.

Polarization Smoothing in a Plasma

These promising properties of speckle statistics in vacuum will be modified in a plasma, where the electron density, and hence the refractive index, is nonlinearly dependent on the local intensity. To model this intricate laser–plasma coupling, we used the code F3D, which has been described elsewhere.[3] For this first study, we limited our attention to the "slow" ion waves responsible for self-focusing and filamentation of the light. PS is modeled by generating two tilted beams at the final focusing lens, resulting in two shifted speckle patterns in the focal plane. To advance the simulation by one time step, each beam is propagated independently (in the z direction) in the density profile. The total intensity distribution in the plasma is then computed by summing the intensities of both beams, and it is used to update the plasma hydrodynamic quantities (density, momentum, and energy) through the ponderomotive and thermal pressures.

The parameters that we used in our simulations are representative of the plasmas that will be produced inside the hohlraums of the future megajoule-scale lasers:[6] equimolar CH mixture; electron density $n_e = 0.1n_c$, where n_c is the critical density at the laser wavelength $\lambda_0 = 0.35$ μm; and electron and ion temperatures $T_e = 3$ keV and $T_i = 1$ keV, respectively. The incident light is focused with an $f/8$ square lens. Unless otherwise specified, the laser intensity is $I_0 = 2 \times 10^{15}$ W/cm^2. The plasma is typically two speckle lengths long, i.e., $2l_{||} = 16f^2\lambda_0 = 1024\lambda_0$, and the usual simulation time is 100 ps. SSD is modeled in its simplest form (1D-SSD),[10] where the laser is sinusoidally phase modulated (FM) at a modulation frequency ν_{FM}, and the grating dispersion is chosen such that the FM sidebands are each separated at focus by $f\lambda_0$ in the y direction ("critical dispersion").

Results and Discussion

Filamentation in the plasma can dramatically change the intensity distribution by increasing the probability of power at high intensity. To illustrate that process and the effect of PS, we display in Figure 1, as a function of position along the propagation axis, the fraction of beam power exceeding five times the average intensity I_0. This measure of the modified intensity distribution, hereafter called the "tail fraction," is admittedly arbitrary, but other measures are similar in behavior. Four different smoothing configurations are considered in Figure 1: (a) a beam smoothed by RPP only, (b) a beam smoothed by RPP and SSD along the y direction, (c) a beam smoothed by RPP and PS, with a separation between the two shifted beams $\Delta x = l_\perp = 8\lambda_0$

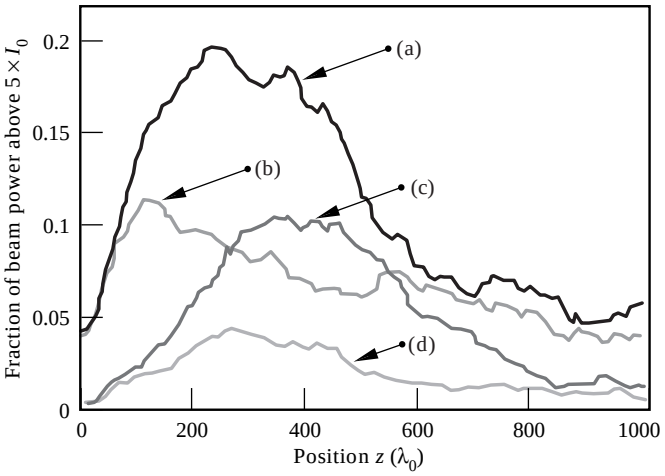

FIGURE 1. Fraction of beam energy above $5I_0$ vs axial position z in the plasma. Smoothing with (a) RPP only; (b) RPP and 1D-SSD (bandwidth $\Delta\nu/\nu = 2.5 \times 10^{-4}$, ν_{FM} = 20 GHz); (c) RPP and PS (beams shifted by $f\lambda_0$ in the target plane); (d) RPP, 1D-SSD and PS as above, with orthogonal dispersions. (50-00-0898-1678pb01)

along x, and finally (d) a beam smoothed by a conjunction of all three techniques (RPP, SSD along y, and PS along x). For all cases the tail fraction first increases monotonically with distance, as small filaments form in the target, concentrating large amounts of the incident energy to high irradiance. Then the tail fraction drops back to roughly its initial value, indicating that the small filamented structures defocus. The first two curves, without PS, start at the value of 4% expected for irradiation by a single beam. Whereas curve (a) reaches a maximum of ~20%, curve (b) grows at the same rate but stops at 11%. SSD apparently has little effect on the focusing of the most unstable hot spots, but is effective in stabilizing the more slowly growing filaments. The PS case, curve (c) starts from a lower value and increases more slowly in space, which reflects the lack of power in fast-growing filaments. That is, PS reduces the power at high intensity in the incident beam. It even turns out, in this case, that the maximum tail fraction is slightly lower than that produced by SSD. Finally [curve (d)], using both techniques is highly effective because PS eliminates the power in fast-growing filaments, while SSD suppresses the growth of slower filaments. The maximum tail fraction in this last case is about the same (4%) as that for an RPP beam in vacuum, illustrating the effectiveness of PS.

The time history of the tail fractions (measured, at each time, at the z positions where their maxima are achieved) confirms the above description, even though the maximum tail fraction can oscillate in time by a few percent around the values of Figure 1. The rise time with PS is slightly longer than with the RPP alone (10 ps versus 7 ps), whereas the growth with SSD is much slower (rise time ~50 ps) and oscillatory. The maximum intensity in the plasma reaches $50I_0$ when only an RPP is used, but is limited to $14I_0$ when PS and SSD are operated together. The values for SSD alone and PS alone are similar, around $30I_0$.

The importance of using SSD and PS together can be illustrated more practically. For a beam smoothed by RPP only, roughly 21% of the energy will be above $5I_0 = 10^{16}$ W/cm^2 at maximum. If we use an SSD- and PS-smoothed beam with the parameters mentioned above and tolerate the same fraction of beam energy above 10^{16} W/cm^2, we can use a pulse with nearly twice the average intensity: $I_0 = 4 \times 10^{15}$ W/cm^2. On the other hand, if we only accept the same absolute amount of energy above 10^{16} W/cm^2, we can still drive the plasma around $I_0 = 3 \times 10^{15}$ W/cm^2, i.e., at a 50% higher intensity with RPP, SSD, and PS than with RPP alone.

From another point of view, PS can effectively increase the bandwidth of the pulse, but without the usual decrease in laser performance. In fact, at $I_0 = 2 \times 10^{15}$ W/cm^2, the benefit provided by PS seems out of reach of SSD alone, as shown in Figure 2. When the pulse bandwidth is increased from $\Delta\nu/\nu = 2.5 \times 10^{-4}$ to 6×10^{-4}, the tail fraction produced by a SSD-smoothed beam only drops from 13% to 10%, far from the 5% obtained with PS at $\Delta\nu/\nu = 2.5 \times 10^{-4}$. The same conclusion holds at $I_0 = 4 \times 10^{15}$ W/cm^2, where a bandwidth $\Delta\nu/\nu = 6 \times 10^{-4}$ results in a maximum tail fraction of roughly 15%, whereas it is only 9% to 10% for a combined smoothing by SSD ($\Delta\nu/\nu = 2.5 \times 10^{-4}$ at 3 GHz) and PS ($\Delta x = f\lambda_0$). Figure 2 also confirms the effectiveness of PS alone relative to SSD alone. With PS alone, the tail fraction is found to be ~12%. To achieve an

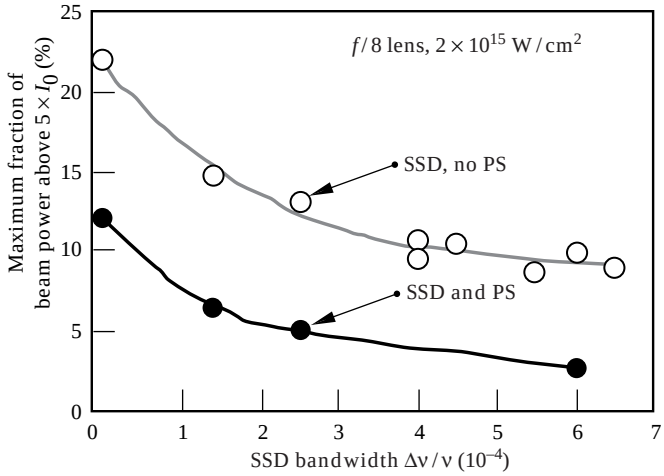

FIGURE 2. Maximum value along z for the fraction of beam energy above $5I_0$, averaged over the last 20 ps of the simulation, vs bandwidth of the 1D-SSD, with or without PS ($\Delta x - f\lambda_0$). Different ν_{FM} guides have been used. (The solid lines are fits to guide the eye.) (50-00-0898-1679pb01)

equivalent tail fraction with SSD alone requires a bandwidth of $\Delta\nu/\nu \sim 3 \times 10^{-4}$. This result is quite notable in that PS only sums two speckle patterns, whereas SSD (asymptotically) sums many more; at $\Delta\nu/\nu = 3 \times 10^{-4}$ and $\nu_{FM} = 3$ GHz, the number of FM sidebands, and hence speckle patterns, is ~85. This emphasizes the importance of the instantaneous nature of PS, and one can conclude that the temporal smoothing rate is critical for suppression of filamentation.

It is interesting to note that some of the data points in Figure 2 have been obtained with 3 GHz SSD, and the other ones with 20 GHz SSD, in both cases critically dispersed. Yet both series obviously lie on the same curve. At a fixed bandwidth $\Delta\nu$, a change in the SSD modulation frequency does not change the time it takes for two independent speckle patterns to be successively generated in the focal plane, which is simply the coherence time, $\tau = 1/\Delta\nu$. Yet a higher SSD modulator frequency means that fewer independent speckle patterns will be formed on the target, so that the asymptotic contrast value will be higher (meaning less smoothing) and reached in a shorter time. The insensitivity of the plasma to the modulation frequency is explained by the fact that its reaction time is of the order of the laser coherence time, so that the larger number of speckle patterns produced in the low ν_{FM} case appears well after the plasma has responded and cannot effectively participate in smoothing the intensity distribution. This is fully consistent with the above statement that the instantaneous smoothing produced by PS is paramount to explaining its effectiveness. Moreover, this also supports using a relatively high SSD modulation frequency in future facilities, since a critically dispersed beam is less divergent at high ν_{FM}. Then the usual difficulties of propagating a divergent beam through a laser chain (such as pinhole clipping in the spatial filters, modification of the pulse shape, and smearing of the focal spot) can be substantially reduced, without negatively impacting the smoothing efficiency.

As is the case in vacuum, the efficiency of PS depends on the amount of spatial separation that is introduced between the beams in the target plane. Our results for $I_0 = 1$, 2 and 4×10^{15} W/cm^2 are summarized in Figure 3. The conditions for these simulations are an RPP only (open points); or an RPP, SSD along y with $\nu_{FM} = 3$ GHz and bandwidth $\Delta\nu/\nu = 2.5 \times 10^{-4}$ (closed points); and PS with a variable shift along x between the two beams (shaded points). Linear optics in vacuum (see "Polarization Smoothing in Vacuum" on p. 83) suggests that the absolute minimum in the tail fraction should be reached for a shift equal to $\Delta x = f\lambda_0$. Plasma-induced nonlinearities modify this simple picture, and the tail fraction appears to be best minimized only for shifts $\geq 2f\lambda_0$.

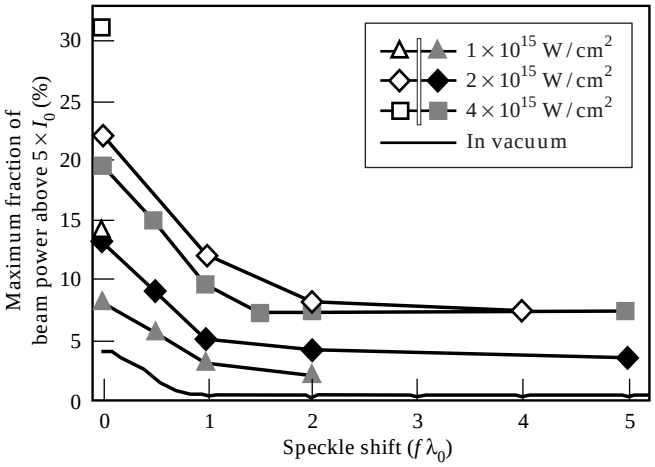

FIGURE 3. Maximum value along z for the fraction of beam energy above $5I_0$, averaged over the last 20 ps of the simulation, vs beam separation at focus. The open symbols correspond to RPP only, the closed ones to RPP and 1D-SSD ($\nu_{FM} = 3$ GHz, bandwidth $\Delta\nu/\nu = 2.5 \times 10^{-4}$). Results with zero beam separation are identical to results without PS. The level obtained in vacuum is also plotted. (50-00-0898-1680pb01)

The initial independence between the beam profiles can change as they propagate into the plasma. To assess this effect, we define a normalized cross-correlation function between the intensities I_1 and I_2 of beams 1 and 2 as

$$K(x,y,z) = \frac{\iint du dv \left[I_1(u,v) - \langle I_1 \rangle\right]\left[I_2(u-x, v-y) - \langle I_2 \rangle\right]}{\sqrt{\langle I_1^2 \rangle - \langle I_1 \rangle^2} \times \sqrt{\langle I_2^2 \rangle - \langle I_2 \rangle^2}} \qquad (2)$$

where the z dependence of I_1 and I_2 is omitted for clarity, and the brackets stand for averaging over the transverse coordinates u and v. Close to the laser entrance plane and as we expected, the cross-correlation function is maximum and equal to 1 for (x,y) equal to the displacement of beam 1 relative to beam 2. Far from this peak, K typically oscillates around ±0.1, owing to the sampling statistics of our finite grid size. We observe two opposing trends when the beams propagate deeper into the plasma—K gets smoothed out, and its maximum oscillates around a low value, $K_{max} = 0.1$ to 0.2, but also the location of this maximum can shift toward the origin in the (x,y) plane. The latter observation means that the beams tend to recorrelate under the influence of the plasma, each one being focused into the density troughs created by the other. Fortunately, the decay of K is faster than this mutual

attraction—only a small fraction of the beams will effectively be recorrelated, while on the whole, they will even lose the "preferred" cross-correlation distance ($-\Delta x$) that they had at the plasma entrance.

For our nominal conditions, with an initial beam shift $\Delta x = 2f\lambda_0$ and a laser irradiance $I_0 = 2 \times 10^{14}$ W/cm^2, this decay of the cross-correlation function occurs after propagation through roughly 750 λ_0. When the irradiance is twice as large, it happens after only $375\lambda_0$. This I^{-1} scaling is consistent with a phenomenon driven by the ponderomotive force of the laser via the plasma density modulations. The variations of K_{max} with z are established in less than 20 ps and remain constant in time thereafter. If the initial separation between the beams, or their intensity, is varied, the competition between recorrelation and decorrelation can evolve differently. At $I_0 = 4 \times 10^{15}$ W/cm^2, e.g., the decay of K along the z axis is roughly the same for $\Delta x = 2f\lambda_0$ and $\Delta x = 1f\lambda_0$, but the maximum of K is localized around the origin in the latter case, indicating less decorrelation by the plasma. When the shift is reduced further to $\Delta x = 0.5f\lambda_0$, K steadily maximizes at the origin of the (x,y) plane after propagation along $400\lambda_0$, with a value of 0.5, supporting a stronger but still partial recorrelation of the beams. This cross-influence of the beams explains why it can be more effective, contrary to what linear optics suggests, but in agreement with Figure 3, to use an initial separation Δx greater than $l_\perp = f\lambda_0$. Note that other implementations of PS,[12,13] where the second beam is completely decorrelated from the first one instead of simply being a shifted duplicate, can significantly reduce this concern. This is, for instance, the case if the orthogonally polarized pulses are transmitted through different phase plates.

Because PS and SSD each disperse in a selected direction, one expects different results depending on whether the PS dispersion is parallel or orthogonal to the direction of SSD dispersion. SSD can be thought of as generating on target a large number of speckle patterns shifted along y. If the PS dispersion is in the same direction, we might expect only a small benefit since the additional dispersion is only marginal. On the other hand, if PS shifts the beams in the orthogonal (x) direction, the maximum smoothing is expected. This effect is simulated with the same plasma parameters as above, SSD bandwidth of $\Delta\nu/\nu = 2.5 \times 10^{-4}$, ν_{FM} = 30 GHz, a shift of $2f\lambda_0$ between the PS-generated beams, and a simulation time of 110 ps. For an average intensity $I_0 = 10^{15}$ W/cm^2, the tail fraction averages to 2% if PS is dispersed along x and 3% if it is dispersed along y parallel to SSD. At $I_0 = 2 \times 10^{15}$ W/cm^2, the tail fractions for the two directions are still similar—3.5% for PS orthogonal to SSD and 5% for PS parallel to SSD, both much smaller than the 13% obtained without PS. Thus, one sees that PS is quite effective even when it is applied along the same direction as SSD. This is due to the fact that even though the PS dispersion is small compared to SSD, PS acts instantaneously, whereas SSD irradiates the plasma with a speckle pattern that changes at the bandwidth limited rate. The addition of PS reduces the tail fraction by smoothing the changing speckle pattern at each instant in time. Although not simulated here, our results suggest that similar benefits will be obtained when PS is combined with any other temporal smoothing method, such as the induced spatial incoherence method.[8]

Conclusion

In conclusion, we have investigated the dynamics of an underdense plasma, typical of those that will be produced by next-generation megajoule-class lasers, when irradiated by an intense laser whose intensity speckle inhomogeneities are reduced by polarization smoothing. The essence of this scheme lies in the superposition, in the focal plane, of two orthogonally polarized and uncorrelated speckle patterns, that, e.g., can be achieved with a wedged birefringent crystal. For intensities of a few times 10^{15} W/cm^2, polarization smoothing was found to be highly effective in reducing the self-focusing of light in the plasma. Its operation in conjunction with SSD leads to a suppression of self-focusing that could not be achieved by SSD alone. We found that a relatively small shift (typically $2f\lambda_0$) between the orthogonally polarized beams in the focal plane is sufficient to achieve this result, since the tendency of the beams to recorrelate as they propagate is found to be limited.

Acknowledgments

The authors acknowledge valuable discussions with G. Bonnaud, T. W. Johnston, and C. H. Still. This work was a cooperation in High-Energy Laser-Matter Interaction Physics by the Commisariat à l'Engerie Atomique and the U.S. Department of Energy.

Notes and References

1. P. Kaw, G. Schmidt, and T. Wilcox, *Phys. Fluids* **16**, 1522 (1973); F. W. Perkins and E. J. Valeo, *Phys. Rev. Lett*. **32**, 1234 (1974).
2. A. J. Schmitt, *Phys. Fluids* **31**, 3079 (1988); A. J. Schmitt, *Phys. Fluids B* **3**, 186 (1991); H. A. Rose and D. F. DuBois, *Phys. Fluids B* **4**, 252 (1992).
3. R. L. Berger et al., *Phys. Fluids B* **5**, 2243 (1993); C. H. Still, R. L. Berger, A. B. Langdon, and E. A. Williams, *ICF Quarterly Report* **6** (4), 138, Lawrence Livermore National Laboratory, Livermore, CA, UCRL-LR-105821-9G-4 (1996).

4. S. P. Obenschain et al., *Phys. Rev. Lett*. **62**, 768 (1989); W. Seka et al., *Phys. Fluids B* **4**, 2232 (1992); A. N. Mostovych et al., *Phys. Rev. Lett*. **59**, 1193 (1987).
5. J. D. Moody et al., *Phys. Plasmas* **2**, 4285 (1995); D. S. Montgomery et al., *Phys. Plasmas* **3**, 1728 (1996).
6. B. J. MacGowan et al., *Phys. Plasmas* **3**, 2029 (1996).
7. C. Labaune et al., *Phys. Fluids B* **4**, 2224 (1992).
8. R. H. Lehmberg and S. P. Obenschain, *Optics Commun*. **46**, 27 (1983); R. H. Lehmberg and J. Goldhar, *Fusion Technology* **11**, 532 (1987).
9. Y. Kato et al., *Phys. Rev. Lett*. **53**, 1057 (1984).
10. S. Skupsky et al., *J. Appl. Phys*. **66**, 3456 (1989).
11. "Phase conversion using distributed polarization rotation," *LLE Review* **45**, 1 (1990).
12. K. Tsubakimoto et al., *Optics Commun*. **91**, 9 (1992); K. Tsubakimoto et al., *Optics Commun*. **103**, 185 (1993).
13. S. Pau, S. N. Dixit, and D. Eimerl, *J. Opt. Soc. Am. B*, **11**, 1498 (1994).
14. S. G. Lipson, H. Lipson, and D. S. Tannhauser, *Optical Physics*, 3rd ed. (Cambridge University Press, Cambridge, 1995).
15. J. W. Goodman, "Statistical properties of speckle patterns," in *Laser Speckle and Related Phenomena*, edited by J. C. Dainty, (Springer, New York, 1984).
16. The transverse coherence length for a speckle pattern is $l_\perp = f\lambda_0$ for square laser beams, as modeled here, and $l_\perp = 1.22f\lambda_0$ for circular ones.

NOVA/BEAMLET/NIF UPDATES JANUARY–MARCH 1998

R. Ehrlich/S. Burkhart/S. Kumpan

Nova Operations

Nova Operations performed 200 full system shots resulting in 208 experiments during this quarter. These experiments supported efforts in ICF, Defense Sciences, university collaborations, laser science, and Nova facility maintenance. As the technicians hired during the previous quarter gained experience in operating the laser, we were able to begin expanding the shift schedule. In the middle of the quarter, the second shift was moved to end at 10:30 p.m. During the next quarter, the operation of Nova will expand back to a full two shifts per day, with the second shift ending at 12:30 a.m.

During this quarter, 94-cm full-aperture gratings were installed in the Petawatt laser system. This allowed an increase in beam diameter to 55 cm, with a corresponding maximum energy of ~900 J. With the completion of the full-aperture compression system, activation of an adaptive-optic wavefront correction system began. Experiments in the Petawatt front-end demonstrated the ability of the deformable mirror to correct for several waves of distortion in a reproducible fashion. Hartmann sensor packages were then deployed in the Nova Output sensor and in the Petawatt diagnostic station following compression. An automatic component status verification system was deployed on the Petawatt system at this time to ensure the proper configuration of components before a full-system shot with the deformable mirror.

A newly redesigned system was built to retrofit one beamline of Nova with an $f/8$ final focus lens for experiments designed to estimate the backscatter levels in NIF hohlraum targets. These experiments during the next quarter will give us confidence that there will be no surprises in NIF hohlraum backscatter levels with reasonable amounts of bandwidth from a high-frequency modulator in conjunction with kinoform phase plates. The experiments will also investigate the effect of a polarization smoothing technique on backscatter levels from various types of targets.

Beamlet Operations

Beamlet completed a total of 121 shots in 44 shot days this quarter. We performed major campaigns on final optics damage at 5 J/cm^2 at 3ω, evaluated extensively the NIF first-boule doubling crystal, executed the final series of pinhole closure experiments at high energy and long pulse, and measured pinhole closure and propagation effects of 1D smoothing by spectral dispersion (1D-SSD). We also began experiments to determine doubling efficiency of the first large fast-growth KDP crystal. Beamlet operations and experimental campaigns are detailed as follows:

- The final optics cell (FOC) and integrated optics module (IOM) were assembled in late December and installed in the Test Mule just before the end of the year. Following alignment, calibration, and the first 5 ramp-up shots, we vented and inspected the medium damage threshold final focus lens (MDT-RFL). We inspected once more the MDT-RFL following the first two shots at the desired fluence (5 J/cm^2), then proceeded with the shot series (see Figure 1). A special optics inspection mechanism was developed for inspecting the MDT-RFL mounted in the Test Mule.
- Eleven shots at 5 kJ (5 J/cm^2) were performed, followed by another Test Mule vent and lens inspection that revealed growing damage as was observed using the on-line inspection system (Schlieren On-Line Imaging of Damage) and by high-resolution near-field photographic film images. Eight more shots were done, and then the IOM/FOC was removed for disassembly, inspection, and damage mapping.
- A new frequency doubler, cut from the NIF first-bundle boule, was delivered to LLNL the last week of December. It was coated, characterized, and installed in the second FOC (FOC-B) by the week of January 26, 1998. The MDT lens, from the

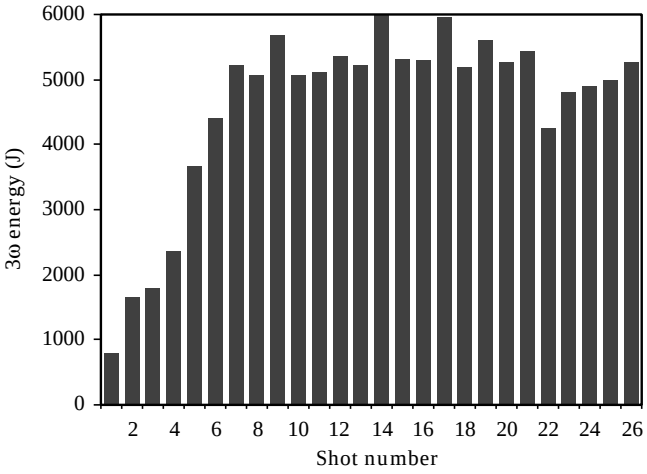

FIGURE 1. Beamlet MDT Lens Campaign, January 1998.
(50-00-1098-1955pb01)

above damage tests, was installed in FOC-B, and the IOM/FOC assembly was returned to Beamlet in late January for Test Mule installation and alignment. System shots for the Doubler Only campaign commenced at the end of January and continued through the end of February.

- Significant calibration effort was performed to obtain confidence in the doubler efficiency experimental results. The design of the focal plane diagnostics (FPDs) does not allow for a direct measurement of all three wavelengths; instead the 2ω is inferred by subtracting a measurement of the 1ω from the whole-beam calorimeter. In addition, the large FPD attenuation precludes direct calibration, and there were unresolved stray light problems affecting the energy diodes. To circumvent this, a large plate of BG18 (1ω-blocking) filter glass was installed to obtain absolute 2ω measurement of the whole-beam calorimeter from which we scaled all of the Doubler Only experiments. This data linked all the previous measurements to the absolute frequency-doubling conversion efficiency of 73.2% for the whole beam, temporal and spatial variations included. This compared to 72.9% from the plane wave model, accounting for the measured pulse shapes. Following these experiments, the diagnostics were redesigned similar to the Beamlet Phase I system, using prisms and calorimeters to separate and independently measure energy in each of the three colors.
- Hardware design is under way for the French Commissariat à l'Energie Atomique experiments scheduled for June. The experiments include silica plate filamentation experiments at 3ω, full-aperture polarizer damage testing, and high-fluence 1ω mirror damage testing at reduced aperture.
- The final pinhole closure experiments, 20 shots, were conducted during the month of March, including cone-shaped 100-μrad Ta, 100-μrad stainless steel (SS), 100-μrad diamond-oriented gold-plated SS, and a 100-μrad solid Au pinhole. Of course, we still had the 150-μrad SS cone, which has been the workhorse for some time because of its superior back-reflection (none) and closure characteristics. In addition, we tested the French pinhole—a design similar to two short cones in series. The Ta cone pinhole performed the best. It took over 7 kJ in a 20-ns square pulse to close it, and it stayed open up to 11 kJ in a Haan ignition pulse with the nominal SSD. The diagnostics for closure worked very well, with good returns from the streaked pinhole interferometer and the gated optical imager. Data analysis was greatly improved with the addition of numerous Interface Definition Language routines to automatically calculate the contrast ratio for a number of 5- × 5-cm patches for each shot. We also measured the threshold for pinhole closure with background pressure, taking shots up to 3.5 kJ through the 100-μrad cone at 90 mT.
- 1D-SSD experiments were purposely limited to a demonstration of transmission through two different pinholes. Two shots above 15 kJ (15.1 and 15.4) were taken through the 150-μrad pinhole with ±7.5 μrad of 1D-SSD using the Haan ignition pulse. Evidence of pinhole closure initiation was observed on the pinhole interferometer, but the plasma was far enough out of the beam focus to not cause near-field beam modulation. We also propagated 20-ns square and Haan ignition pulses through the 100-μrad Ta cone. The Ta cone was the big surprise in the campaign, as it performed exceedingly well. It transmitted 11 kJ using ±7.5-μrad divergence with the Haan ignition pulse shape. The last mirror in the mirror tower (M9), damaged during the first 11-kJ Haan ignition pulse shape, incurred a damage spot of about 3 mm and was subsequently replaced. Although the spot is not growing, the modulation is too large for further high-fluence frequency conversion campaigns.

National Ignition Facility

Summary

Overall progress on the NIF Project remains satisfactory for the second quarter of FY98. During this quarter, NIF construction subcontractors recovered four of the estimated six to eight weeks of schedule lost in the November and December El Niño rains, despite the heaviest rainfall on record for the month of February. Implementation of a wet weather construction plan,

additional construction equipment, additional manpower, and an extended workweek combined with a second shift generated a sense of urgency and improved productivity through the quarter.

In Special Equipment, 79% of the Mid-Title II (65%) design reviews and 10% of the Title II (100%) final design reviews have been completed. The two major procurements, Beam Transport Stainless Steel and the Target Chamber, are on schedule.

In Optics, the progress on facilitization contracts and development activities remains satisfactory. The first full-scale continuous pour of NIF laser glass has yielded positive results. The potassium dihydrogen phosphate (KDP) rapid growth decision was made early, and the KDP facilitization contracts awarded. Also, the contracts for mirror and polarizer coating facilitization were awarded.

There were no Level 0, 1, 2, 3 milestones due during the second quarter. There were 18 Department of Energy/Oakland (DOE/OAK) Performance Measurement Milestones due this quarter, and 19 were accomplished. There was a total of 30 milestones due in the first half of FY98, and 31 have been accomplished, for an overall variance of (–1). In March, nine milestones were completed, whereas seven were planned. This is based upon DOE/OAK's concurrence with *Revision A* of the FY98 Milestones, which was effective February 28, 1998.

Key Assurance activities during the second quarter to support the Project included assurances preparation for major concrete pours and disposition of mammoth bones. Litigation activities included the following:

- Litigation support to the DOE for the settlement of 60(b) (Agreement to prepare a Progammatic Environmental Impact Study supplement analysis and to conduct specific evaluations and surveillance of potential buried hazardous materials) and the overall litigation against the Stockpile Stewardship Program's *Programmatic Environmental Impact Statement*.
- The NIF Construction Safety Program.
- Interface with the LLNL Institutional surveillance for buried hazardous/toxic and/or radioactive materials.
- Risk Management Plans.
- The *Final Safety Analysis Report*.
- Assurance surveillances and audits.
- Support for environmental permits.

All are on schedule.

The current assessment of Project status remains as stated last quarter; there will be no change to the 4th Qtr. 2001 Level 2 milestone for the End of Conventional Construction nor to the 4th Qtr. 2003 Project Completion date. However, it is still anticipated that there could be a three- to six-week impact to the 4th Qtr. 2001 Level 4 milestone for the start-up of the First Bundle. The current assessment is that there may also remain two to four weeks' impact to other internal milestones for construction. This is an improvement since the first quarter report resulting from the accelerated use of overtime on the construction site. Accelerated activities in addition to the rain mitigation actions taken in the second quarter, which could reduce the First Bundle schedule impact, are currently being assessed in conjunction with construction contractors.

Site and Conventional Facilities

The NIF Conventional Facilities construction subcontractors recovered four weeks of lost schedule during the second quarter despite the heaviest rainfall on record for the month of February. At the end of March, Walsh Pacific (Construction Subcontract Package [CSP]-3, Target Building Mat and Laser Bay Foundations) had recovered one-half of the two months schedule lost in the November and December El Niño rains. As noted above, implementation of a wet weather construction plan, additional construction equipment, additional manpower, and an extended workweek combined with a second shift generated a sense of urgency and improved productivity through the quarter (see Figure 2).

The bids for CSP-6/10, Target Area Building Shell and Buildout, were received in March, bringing to closure the procurement phase of the major Conventional Facilities construction subcontracts. Seven of the eight Conventional Facilities construction subcontracts have been awarded; two of these subcontracts (CSP-1 and 2) are complete, and four subcontractors (CSP-3, 4, 5, and 9) are actively constructing on the NIF site. Construction work in place at the end of the second quarter is approximately 9%.

The Conventional Facilities Title II engineering design ended on schedule in February, and Title III engineering support to construction began in earnest concurrent with the ramp-up of subcontractors and craftspersons at the NIF site.

FIGURE 2. Target Area retaining wall forms and rebar.
(40-60-0198-0084#46pb02)

Construction Milestones. Several important milestones were achieved on the NIF site in the second quarter. The critical path backfill of the retaining wall along gridline 10/12 was completed (FY98 DOE/OAK Performance Measurement Milestone). This was important for two reasons. First, the completion of backfill allowed footings and tie-beams in the Laser Bays to be completed, a prerequisite to start of structural steel erection, which is, in turn, on the critical path of construction activities for the Laser Bay. Second, the completion of the Target Building retaining wall backfill was the final construction work by Teichert under CSP-2.

Another significant milestone achieved by Walsh Pacific (CSP-3) was the placement of the Target Bay mat slab (FY98 DOE/OAK Performance Measurement Milestone); this 3300-cubic-yard continuous pour occurred over an 18-hour period in late March (see Figure 3). This critical path concrete work in the Target Building is the first of three major mat slab pours by Walsh Pacific that are prerequisite to the start of work in the Target Building by Nielsen-Dillingham, CSP-6/10. Other work completed by Walsh Pacific included forming, rebar, installation, and placement of concrete in the Target Building retaining wall and footings; the Target Building wing walls; and the footings, short pilasters, and tie beams within the Laser Building core.

Nielsen-Dillingham (CSP-4) continued steel fabrication in Oklahoma City during the second quarter, with anticipated arrival on site in mid-April. All critical submittals and shop drawings have been reviewed and approved. Dillingham (CSP-5) also completed the Optics Assembly Building (OAB) concrete footings six days ahead of schedule (FY98 DOE/OAK Performance Measurement Milestone). The work on contract includes: completed footing and foundations, poured basement walls, continued installation of the grounding loop for building steel, erected structural steel column stubs on the entire perimeter, and started basement wall. The Nielsen-Dillingham CSP-6/10 bids were opened and the contract was awarded in March.

FIGURE 3. Finishing the Target Bay slab. (40-60-0398-0616#20pb01)

Hensel-Phelps (CSP-9) and their subcontractors have fully mobilized their trailers on site. A full platform proposal that will shorten the subcontractor's duration in the Laser Building was negotiated this quarter at no cost to the NIF Project. Hensel Phelps will begin site utilities in April, including: storm drain and sewer lines at the east side of the site, tie into mechanical bundle at the northeast side of the site, and site temporary power.

Mammoth Bones. The excavation of the mammoth bones in the area of the Laser Building 1 retaining wall footing, adjacent to Switchyard 1, was completed in February. DOE confirmed in March that bones located adjacent to the Diagnostics Building and Switchyard 2, outside the building footprint, will not be removed at this time. Change orders will be issued to subcontractors by Conventional Facilities to protect the bones for future recovery. Survey information and maps identifying the locations of the bones have been recorded for future reference.

Special Equipment

This quarter, a major focus was to successfully bring closure to outstanding requirement issues as part of the Mid-Title II (65%) design reviews. With the completion of the second quarter, a majority of the Mid-Title II design reviews were completed, and more of the final (100%) design reviews were held. Reviews of the Beam Transport procurement packages also began.

Mid-Title II reviews were held for the Laser Amplifier, the Target Positioner, the Optical Pulse Generation (OPG), Optical Assembly and Alignment Systems, Alignment Control, Precision Diagnostics, Roving Mirror and Roving Assemblies, Power Diagnostic and Back-reflection Sensor/Portable Sensor, Energy Diagnostic, the Final Optics Assembly (FOA), the Target Chamber Vacuum System, Target Area Structures, and Relay Optics/3ω Energy. Final design reviews were held for the Supervisory Control (Framework) and the Computer Systems. Design review reports were prepared and released for the Pockels Cells, the Beam Transport, the Target Positioner, the Amplifier, the OPG, and the OAB reviews.

Laser Systems. Nearly all Laser Systems design issues have been resolved, and detailed drawings are being produced in all areas. Substantial progress was made on prototypes during the second quarter. The preamplifier prototype was procured and assembled in preparation for testing during the third quarter. Tests on the Amplifier Module Prototype Laboratory (AMPLAB) amplifier prototype were completed for the 2-slab-long configurations. The 4×1 Pockels cell prototype was assembled and tested, demonstrating

the necessary switching performance for the NIF. The detailed design of the power conditioning first-article prototype was completed, while the performance models were validated by tests on the existing prototype capacitor module. Design documentation is being produced at a rapid pace consistent with completing in time to procure hardware for the first beam bundle.

Optical Pulse Generation. A substantial effort during the past quarter focused on resolving the remaining issues required to complete the OPG design. Experiments and modeling quantified the modulation due to FM-to-AM conversion from the modulators in the Master Oscillator system. A decision was made to use polarizing fiber to minimize the modulation, while system propagation modeling began to quantify the impact of the residual AM on laser performance. The rmaining hardware for the prototype preamplifier module arrived, and assembly of this complex subsystem began. Perfor-mance of important subassemblies was validated, in-cluding commercial diode arrays, the regenerative amplifier, and the optoelectro-mechanical beam-shaping module produced by Allied Signal in Kansas City. Optical design of the preamplifier beam transport system was completed, enabling the team to freeze the design and begin detailed drawing production.

Amplifier. Since the key features of the amplifier design were frozen in the first quarter, the design team is now in the process of creating detailed fabrication drawings. During the second quarter, many of the computer-aided design (CAD) models were sufficiently completed that they could be exported to a subcontractor for detailing.

A parallel experimental effort, centered in the AMPLAB, worked to address the few remaining open issues and provide a final physics validation of the design. The $4 \times 2 \times 2$ AMPLAB gain and wavefront experiments were completed during the second quarter, and the facility is currently being configured to measure three-slab-long gain and wavefront to complete the data set required to validate the amplifier model. The three-slab-long measurement is expected to show that most of the wavefront error is produced by the end slabs in the amplifier chain. This would explain the concern raised earlier this quarter regarding a discrepancy between the expected and measured wavefront error on the AMPLAB. Analysis of the data is ongoing, but so far indicates that the amplifier will meet or exceed its gain requirement.

In response to the issue raised earlier this quarter, the cleanliness tiger-team, consisting of NIF amplifier, cleanliness, and optics personnel as well as LLNL analytical chemists, continued to characterize the nature, source, and effects of the contamination observed in AMPLAB. A detailed plan was developed to complete the tests necessary to demonstrate that the amplifier can be installed and operated cleanly.

Pockels Cell. During the past quarter, the plasma electrode Pockels cell (PEPC) detailed design has progressed in parallel with activation and testing of the 4×1 prototype cell. The prototype drawings, also considered the Title II drawings, were entered into the Project Data Management system and placed under configuration control. Several interface control documents (ICDs) were updated to reflect changes since the 65% review. Parts for the prototype control system were ordered. The controls approach will be validated through integrated testing with the 4×1 prototype. The prototype was assembled and tested for the first time during the second quarter. Minor problems with potting and simmering were encountered and solved. By the end of March, the prototype was operating, and simultaneous measurements on all four apertures indicated that the cell exceeds the minimum NIF requirements for switching efficiency in both the “on” and “off” states. The remaining operational prototype effort will test the cell against the remaining system requirements and validate the controls and diagnostics designs via integrated testing and operations. The mechanical prototype is assembled, and preparations are under way for mounting and alignment tests.

Power Conditioning. The power conditioning effort during the past quarter was focused on completing the design of the first article so that parts could be ordered and on using the existing $2 \times 2 \times 5$ capacitor prototype module to refine and validate a detailed circuit model. The model was then modified to reflect the design of the $2 \times 3 \times 4$ first article and predict its performance. Several meetings of the design team were held to resolve the issues regarding the first article design. Among the decisions made were the following: the use of coaxial cable instead of twin-line, the architecture of the first article module ($2 \times 3 \times 4$), the grounding strategy for the bank / amplifier system, and the details of the preionization pulse requirements. A scale model of the first article module was completed and is being used to develop maintenance and safety procedures for the bank, as well as to help the design team evaluate the architecture. The life test of the baseline (ST-300) switch commenced in order to demonstrate adequate life and performance at the elevated currents associated with 24-capacitor operation.

Beam Transport System (BTS). Final checking and documentation for critical path components were highly focused activities in this quarter. The installation schedule drove all resource priorities. The first two procurement packages, for the Laser Bay steel material and spatial filter vacuum vessels, were completed and reviewed, including checked and signed drawings, engineering calculations, and all Title II deliverables. The BTS structural / mechanical analysis team completed the Title II analyses and

final analysis reports for the BTS Laser Bay structures, the Bldg. 298 laydown area grading activity is under way, the amplifier cooling system fan units have begun fabrication and are on schedule, and the stainless steel plate is on schedule.

- The spatial filter vacuum vessel designs were completed, and drawings were signed and released into Configuration Management (CM). The fabrication specification was completed and reviewed. Mill production of stainless steel is nearing completion and is on schedule.
- Discussions with Los Alamos National Laboratory (LANL) regarding the proposed Roving Mirror system design, space allocation, alignment, installation sequence, and cleaning issues for the switchyard enclosures were continued. BTS has finalized its decision to perform design and installation of enclosures using internal rather than external resources to allow more schedule flexibility for the Roving Mirror changes proposed by LANL system.
- Ports were added to the Laser Bay interstage beam tubes for clean air purge in the event of in situ maintenance. Seal testing was initiated to evaluate three candidate materials (solid silicone, silicone foam, and expanded Teflon tape) and a number of bolt patterns at both switchyard and Laser Bay pressure differentials.
- The PEPC team recently made a change to use self-contained, local dry pumps to provide backing turbomolecular pumps for the vacuum system. Therefore, a separate backing line to the PEPC is no longer needed from Auxiliary Systems.
- Leak rate measurements for one design of the beam tube seals was completed to validate the design of the gas-handling system.
- The Switchyard 2 structural support structural drawings are about 80% complete, and the structural steel quantity takeoff (spread sheet) is 95% complete. It includes everything but LM5 support subframes because some member sizes are not available.
- Finite-element analysis plots of forces and moments necessary for the completion of the concrete pedestal reinforcement design calculations for the Laser Bay were generated. Pedestal design is nearing completion. Steel-concrete interface force data for the pedestal embedment plates was prepared.
- Tests of o-ring, flat gasket, and formed gasket seal designs for the spatial filter lens prototype were conducted. All three seal designs met the design requirements. These test results provide high confidence in proceeding to final, detail drawings for the spatial filter lens cassettes (see Figure 4). The prototype testing has shown that formed gaskets can be used in place of o-rings at lower cost and similar performance.
- A modified transport mirror attachment design was tested during February. This modification contacted the bore in the back of the mirror at its midplane, which reduced the distortion induced on the front face. Interferometer tests confirmed that a significant reduction was achieved. Improvements to address two problems, plastic deformation of the attachment and creep of the elastomer within the attachment, have been identified.

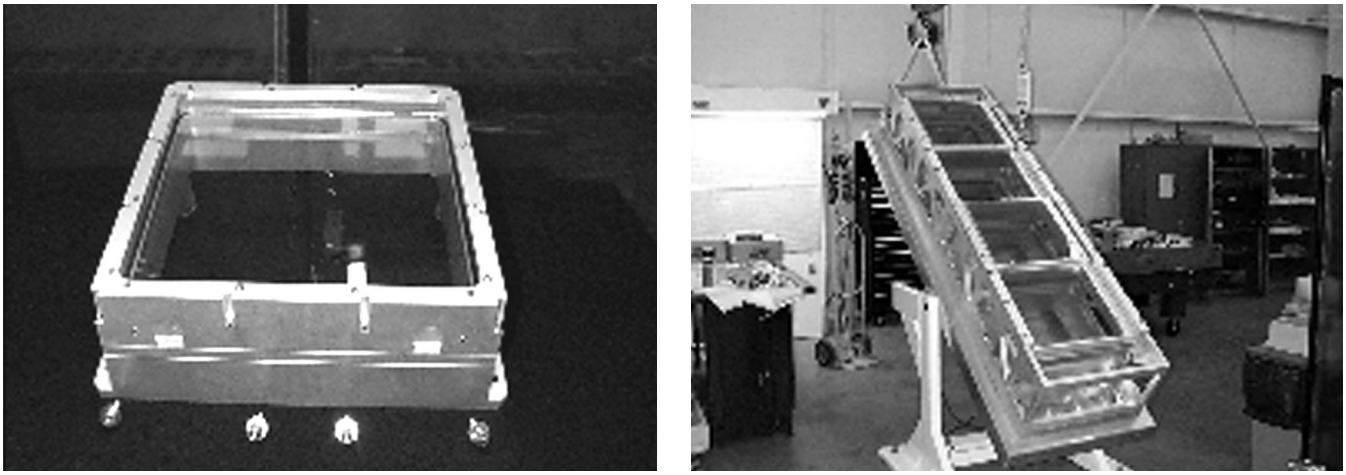

FIGURE 4. A single spatial filter lens assembly is shown above on the left. Four such assemblies are installed into a cassette, which has a strong back for stiffness / handling (shown on right). (50-00-1098-1989pb01 and 50-00-1098-1990pb01)

Integrated Computer Control System (ICCS). Title II 100% Design Reviews were conducted a month early for the Computer System and the Supervisory Software Frameworks.

- The 100% design review for the computer system and network held in February featured 153 drawings, all of which are under configuration control. The network design has evolved since the 65% review to become a hybrid topology of switched Fast Ethernet and Asynchronous Transfer Mode networks. Analysis of expected traffic over the full-shot cycle combined with simulation study shows that substantial performance margin exists in the design. The prototype operator console was delivered and installed in Bldg. 481-1206 for conducting ICCS testbed demonstrations.
- The Title II 100% Review of the Software Frameworks was delivered in February. The review featured a number of presentations on the framework including front-end processor (FEP) preparation, operations databases, system management, status monitoring and reporting, CORBA distribution strategy and measurements, and results from the discrete event simulation for the status monitor performance.
- The report for the 65% Design Review for the integrated timing system was released. In total the reviewers generated 46 comments, of which 7 were level one, 35 were level two, and 4 were level 3. The review committee recommended that an additional prototype of the timing distribution backbone be pursued to demonstrate precision timing requirements and ensure continuing vendor involvement leading to NIF deployment.
- The Control Logix integrated safety system beta unit was received from Allen-Bradley and activated for testing. This unit represents the next generation of higher-performance programmable logic controllers and will form the basis for the NIF Industrial Control Systems.
- The Preliminary Timing Analysis of NIF Beamline Alignment was finalized and used to demonstrate Alignment Control's ability to meet Software Subsystem Design Requirements (SSDR) alignment time specifications in support of the 65% review. This analysis defines the step-by-step alignment procedures from the Preamplifier Module (PAM) through the Target Chamber and includes how shared resources (such as the Output Sensor and Target Chamber) impact system performance.

Optomechanical Systems Management. Title II design progress was very good. Spatial filter lens cassette prototype testing was completed. Mirror attachment design testing continued with moderate success. Transport mirror sizes were determined. Most of main laser cavity optics final drawings have been released. The FOA Mid-Title II (65%) design review was held. The final optics configuration was updated to incorporate ECR180. Major pieces of FOA prototype hardware were received. The CAVE (Crystal Assembly Verification Equipment) became ready to begin manual measurements.

Optical Design. Title II optical design progress during the second quarter included the following:

- The final, planned update to the main laser design optical configuration drawing was released. The optical design of the main laser cavity is complete.
- The optical design of the OPG system was presented by the responsible optical engineer at the Mid-Title II (65%) review in February. Important results were reported for the optical stability analysis, the wavefront specifications for optical components, the optical layout (under CM), and the optical design performance.
- Detailed optical design studies of the telescopes in the preamplifier beam transport section (PABTS) of the OPG were completed and showed that a lengthening of the relay telescope was necessary to reduce fluence on lenses within the telescope. As part of the system design, the telescope in the input sensor package was also redesigned to better balance the energy loading.
- Good progress was made on releasing final main laser optics drawings into CM. The following drawings have been released: amplifier blank, spatial filter lens, cavity mirrors and polarizer, switch window, and diagnostic beamsplitter. The remaining cavity optics drawings (switch crystal and amplifier finishing) are being updated by the optics manufacturing organizations.
- The Title II mirror sizes for the transport mirrors were determined. The alignment scheme (i.e., which mirrors would be used to control pointing to the target and centering at the final optics) had to be changed to obtain mirror sizes acceptable to the various interfacing groups, generally decreasing in size. As a result, the final drawings (nine) for the mirror blanks were released.
- Two out of six FOA optics drawings are under CM (target chamber vacuum window and focus lens). The final sizes of the diffractive optics plates and debris shields were established and the Title II drawings should be released in April.
- The defect-induced damage analysis calculations for the NIF vacuum barriers investigated the beam modulation at spatial filter lenses (vacuum barriers) arising from defects in optical components. The results showed that the presence of

defects modulates the beam slightly more than fabrication phase errors, but that this modulation is below damage thresholds. The results confirm that the polarizer and LM3 are the most sensitive locations for defects.

Optical Components. Several potential qualified suppliers have expressed strong interest in supplying the BK-7 mirror and polarizer substrate materials for the NIF. In contrast to the other materials, BK-7 is a commodity glass requiring no special facilitization or development efforts. The statement of work was written for these substrates in conjunction with the release of the Title II mirror and polarizer substrate drawings.

Significant progress was made in NIF small optics in the second quarter. A list of prototypes and a delivery schedule were developed, along with a vendor survey from which a qualified bid list will be developed for production optics. The Vendor Qualification Plan was also completed and released on schedule.

The small-sample cleanliness verification system was completed, as was a comprehensive technical review of the large-optics processing plan. This review included a status of the following areas: all optics processing support facilities for the NIF, QA for optics processing, staffing and training, database documentation, facility and process cleanliness control, and mechanical handling equipment and fixtures. The requirements document for the Metrology Data Management System, which will be used to assist inspection and quality assurance (QA) of the optics at the vendors and LLNL, was updated based on input from the optics component lead engineers and the vendors.

Laser Control. Considerable progress has been made in completing and reviewing parts of the laser control design. In addition, various prototype components were ordered, received, and assembled, with more on the way.

- The Transport Spatial Filter area now has a fully integrated design that encompasses the mechanical, optical, and electronic systems for the preamplifier module, injection beams, alignment and diagnostic beams, input sensors, output sensors, and beam enclosures.
- Solid modeling of the Input Sensor package is essentially complete, and some detail drawings are also finished.
- Signal level requirements for beam control light sources were analyzed in more detail using a complete NIF transmission model for all optical paths from the light source locations to the corresponding detectors. The model compared well with the transmission elements of current beam propagation codes, and the two methods are believed to be equivalent.
- Substantially all of the mechanical parts for the Output Sensor prototype have been received, and assembly is being planned. Similarly, all purchased parts for the sensor test stand are in hand while fabrication parts are on order.
- The optical design of the Laser Optic Damage Inspection (LODI) System was modified to accommodate 3ω light. When the Schlieren focus stop is removed, LODI can be used to record near-field images of light that have made a round trip to the final optic and back. This will likely be part of an on-line system for measuring the net 3ω reflectivity profile of the 1ω transport mirrors.

Target Experimental Systems. The Target Experimental System has continued Title II design according to schedule, for the most part.

- All 18 target chamber plates have been formed and shipped to Precision Components Corp. (PCC) for edge machining. The first sphere plate edge machining was done at PCC, with the long sides of the plate receiving the weld groove configuration. The land of the weld joint will be at a 5064 mm (199.38 in.) radius on all pieces (see Figure 5). This will facilitate alignment and use of semiautomated welding equipment.
- Stainless steel louvers appear to work for both the x-ray panels and beam dumps in the target chamber first wall. Tests showed that either B4C or stainless steel louvers pass the requirement, which is the debris shield contamination rate limit. Stainless steel louvers are substantially cheaper than B4C louvers, and since the base material does not matter, there is no strong reason to go to the additional expense of B4C louvers.

  Work is proceeding to test a prototype stainless steel louvered beam dump on Nova. The fixture is designed and is being reviewed with Nova personnel. The stainless steel louver without a vertical member has been tested on 2-beam, and a

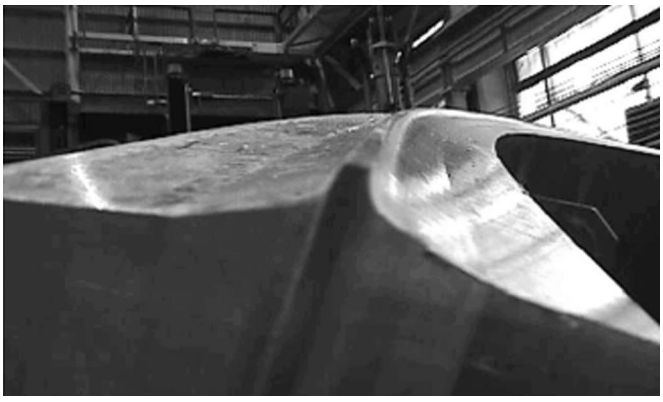

FIGURE 5. Shown is the radiused weld prep that has been machined on one of the target chamber sections. (40-00-1098-2033pb01)

larger panel with 45° louvers with vertical members will be tested on Nova.

- The 65% Title II Design Reviews for the target chamber vacuum system and the target positioner were held this quarter. Creation of detailed mechanical drawings for the Target Bay vacuum components assemblies and detailed design of the positioner are proceeding.
- A Diagnostics Working Group Meeting was held at Jackson Hole, Wyoming, to present the status of the NIF design and discuss the diagnostics to be placed on the NIF and other laser facilities. Data Acquisition, Calibration facilities, X-Ray Diagnostics, and Neutron Diagnostics were also discussed. Participants included representatives from LLNL, LANL, Sandia National Laboratories (SNL), Laboratory for Laser Energetics (LLE), and Atomic Weapons Research Establishment (AWE), who are also developing a Web page to share diagnostic design information. It will soon be password accessible by diagnostic users.
- The design of the diagnostic instrument manipulator (DIM) is proceeding. AWE has designed and is starting the fabrication of a test setup to verify the design of the rails that mount the insertion tube and the z-axis motor design. Detailed drawings of this test setup have been received. AWE is reviewing the DIM development schedule and LANL has volunteered the Trident laser facility for evaluating the prototype DIM.
- The Q31T mirror support frame, the largest and most complex, is located in a position within the Target Area Building that experiences the most severe environmental conditions. For this reason, it has been extensively analyzed to validate the proposed structural design, and detail drawings are being prepared so it can be a model for the remaining frames.

Final Optics Assembly. Title II second quarter progress for the FOA is summarized below.

- The Mid-Title II (65%) FOA design review was presented in February. All mechanical subsystems were reviewed: integrated optics module (IOM), final optics cell (FOC), debris shield cassette, actuation system, alignment fiducial arm, 3ω calorimeter chamber, vacuum isolation valve, thermal control system, and vacuum/venting system. The optical configuration was described, and a scientific update on frequency conversion, with special attention paid to the performance error budget, was also given. Analysis results presented included structural, seismic, thermal, and computational fluid dynamics.
- The optical configuration was revised to implement the requirements imposed by ECR180 (additional diffractive optic cassette). Extensive ghost analysis and optical chief ray tracing provided detailed input to establish the revised configuration.
- Work has focused on incorporating ghost mitigation measures (e.g., absorbing glass) into the IOM. The ghost analysis has indicated that two sides and both ends of the of the IOM require mitigation. It is highly desirable to use glass that is textured appropriately to diffuse or scatter the incident light, thereby reducing the fluence on subsequent surfaces. Work has also been proceeding on ghost control in the FOC. Two sides of the cell are "illuminated" by stray light at sufficient levels to require protection. The baseline scheme involves covering the sides of the cell and the retaining flanges with absorbing glass. Key test data is needed for the damage limits of various materials (aluminum surfaces, ceramics, and absorbing glass) to complete the design.
- Major pieces of FOA prototype hardware were received: the calorimeter chamber, three integrated optics modules, large test stand, and debris shield cassette hardware. The test stand was installed in Bldg. 432, and the pumping system

FIGURE 6. The full-scale FOA test stand (large steel structure in center of photo) was installed in the Bldg. 432 high-bay in March. A CAD representation of the FOA has been superimposed to illustrate the soon-to-be-installed hardware. The actual vacuum isolation valve is shown on a support stand at the bottom of the photo. (40-00-1098-2032pb01)

was located at the base of the stand, as shown in Figure 6. It will permit testing of the prototype hardware in an orientation consistent with installation on the target chamber. The vacuum isolation valve will be installed after the valve body is caustic-etched, and the revised bell crank mechanism is fabricated. The calorimeter chamber is ready for installation thereafter.

- All hardware for the CAVE has been delivered and assembled in Bldg. 432 (see Figure 7). Specifically, the following items were installed: optical table, temperature-controlled clean room, high-power laser, and large reference mirror. The laser operational safety procedure and interlocks were approved so that operations can begin.

Operations Special Equipment. Title II design is progressing well. Hardware prototyping is providing excellent cleanliness data and design validation. During the second quarter, the group completed the Transport and Handling (T&H) 35% Review, the OAB Mid-Title II (65%) Review, and an Informal OAB Corridor Review.

- Line-replaceable unit (LRU) refurbishment meetings with various LRU owners continued in order to develop requirements for refurbishment. Requirements for LRU and equipment movement in the OAB corridor were documented. The drawing package of the corridor is now complete.
- The detailed designs of the bottom-loading, top-loading, side-loading, switchyard, and Target Area delivery systems are progressing well. The 35% Review was completed this quarter.
- The interface and Phase II requirements review was held this quarter with RedZone Robotics, Inc. / AGV Products, Inc. to clarify the Laser Bay transporter deliverables and the requirements of the design. Permission was given to the vendor to start procuring long-lead items for the fabrication of the first vehicle.
- The assembly and testing of the T&H prototype hardware is progressing well. The "clean" testing of the cover removal mechanism for the bottom-loading canister has begun and will be completed next quarter. The assembly of the components for the insertion mechanism is complete, and dirty testing of the mechanism has begun. The hardware for the scissors mechanism and vacuum cover has been fabricated, and assembly will start in April.
- The OAB hardware designs and the simulation model were presented in February at the Mid-Title II (65%) design review. The review was highly interactive, key areas of interest were discussed with the interface partners, and all comments have now been addressed.
- The software requirements specifications were completed for the FEPs for bottom-loading, top-loading, side-loading, and switchyard delivery systems. The control points (sensors, actuators) for all T&H prototype delivery systems were specified. A draft interface specification was completed identifying data interfaces between the Laser Bay transport system computer systems and the T&H FEPs and Supervisory System. A "proof of concept" graphical user interface of an OAB integrated desktop was presented at the OAB 65% review and received very positive feedback.

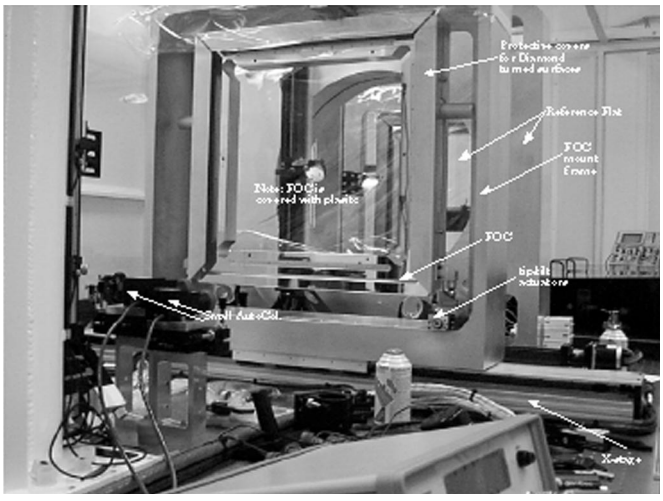

FIGURE 7. The CAVE FOC mount, the reference flat, horizontal slide, and autocollimators for tracking tip / tilt as the mount is translated. (40-00-1098-2031pb01)

Start-Up Activities

Integrated Project Schedule (IPS) Assessment. The month-end March status of the IPS showed no impact to Level 0–3 milestones. Current schedule issues are (1) the coordination challenge of interfacing Conventional Facilities multiple subcontractor activities with Special Equipment activities, (2) restructuring the Optics schedule module in the IPS from process-based (development / facilitization / pilot / production) to component-based (windows / lenses / mirrors / polarizers / etc.) activities, and (3) adding equipment installation details to the IPS.

Start-Up Planning. A draft Start-Up Plan for the first bundle has been completed on schedule. The purpose of this plan is to outline the sequence of integrated system Operational Test Procedures, which constitute start-up of the first bundle of eight beam-lines. These integrated tests will be conducted once all first bundle special equipment in Laser Bay 2 has been installed and Acceptance Test Procedures have been completed. After start-up has been successfully completed, the first

bundle will be ready for ICF / NIF Program experimental operations.

Advanced Operations Planning. A draft *NIF Operations Procedures Plan* document has been completed. The NIF Start-Up and Operations Planning Group is responsible for providing the management and technical oversight necessary to ensure a smooth project transition from the construction and equipment development phase of the NIF to integrated beamline operation in a fully functional facility.

Optics Technology

Facilitization efforts are proceeding well. The initial evaluation of the Schott laser glass melting campaign at the end of the first quarter was very promising. The glass was formed at full size without any major problems with inclusions or fracturing. Minor problems with the melter and batch feeding system will be addressed when the melter is rebuilt for the pilot production campaign in the first quarter 1999. Though not all of the specifications were met during this campaign, the assessment both at Schott and LLNL is positive. Hoya started and completed its final subscale campaign at the production facility in Fremont, California. The glass met nearly all the NIF specifications, but OH content needs to be reduced slightly. Fine annealing of both the Schott and Hoya glass will be complete in the third quarter, so the glass can be evaluated for homogeneity.

Facilitization of the remaining four rapid crystal growth tanks was accelerated during the second quarter due to the early decision to select rapid growth as the baseline process for NIF crystals. Several crystals were fabricated from development boules for frequency conversion testing on Beamlet; the optical quality and damage threshold meet NIF specifications.

Finishing facilitization at Zygo is on schedule and going extremely well. The NIF facility was formally dedicated in February 1998. The start of the Tinsley building construction was delayed from November 1997 until April 1998, primarily due to the extended rains. Aside from the building, most of the equipment design and construction at Tinsley is on schedule.

Coatings facilitization contracts were negotiated and signed with Spectra Physics and LLE in the second quarter. Veeco Process Metrology, formerly Wyko, delivered interferometry unit Nos. 2 and 3 to LLNL and Hoya, respectively. Facilitization efforts in other metrology areas, including photometry and surface inspection, also went well.

Upcoming Major Activities

During the third quarter of FY98, Conventional Facilities will complete the CSP-3 Target Bay and Mat Foundations work and begin the CSP-4 erection of the Laser Building steel. In the OAB, the concrete foundations will be completed, and the steel work will begin. In Special Equipment, the 65% and 100% design reviews will continue at a faster pace, and procurements will be initiated for some of the Beam Transport items such as the Spatial Filter Vacuum vessels. In Optics, the contracts for mirror and polarizer substrates should be placed, and the vendor facilitization activities will continue.

PUBLICATIONS AND PRESENTATIONS JANUARY–MARCH 1998

A

Afeyan, B. B., Boley, C. D., Estabrook, K. G., Matte, J. P., and Ratowsky, R. P., *Laser Beam Propagation and Interaction in Pinhold Plasmas Including Plasma Kinetic Effects*, Lawrence Livermore National Laboratory, Livermore, CA, UCRL-JC-129863 ABS. Prepared for *Solid State Lasers for Application (SSLA) to Inertial Confinement Fusion (ICF) 3rd Annual Intl Conf*, Monterey, CA, Jun 7, 1998.

Afeyan, B. B., Chou, A. E., Matte, J. P., Town, R. P. J., and Kruer, W. L., *Kinetic Theory of Electron Plasma and Ion Acoustic Waves in Nonuniformly Heated Laser-Plasmas*, Lawrence Livermore National Laboratory, Livermore, CA, UCRL-JC-128687; *Phys. Rev. Lett.* **80**(11), 2322–2325 (1998).

Aikens, D. M., Bajuk, D., Rich, L., and Slomba, A., *Developing Enabling Optics Finishing Technologies for the National Ignition Facility*, Lawrence Livermore National Laboratory, Livermore, CA, UCRL-JC-129317. Prepared for *1998 Summer Topical Mtgs*, Kailua-Kona, HI, Jun 8, 1998.

Amendt, P. A., Bailey, D. S., Celliers, P., Glinsky, M. E., London, R. A., Maitland, D. J., Strauss, M., Visuri, S., and Young, D. A., *Vapor Bubble Studies for Medical Applications: Dynamics and Energetics*, Lawrence Livermore National Laboratory, Livermore, CA, UCRL-JC-129419. Submitted to *J. Appl. Phys.*

Auerbach, J. M., Barker, C. E., Couture, S. A., De Yoreo, J. J., Eimerl, D., Hackel, L. A., Hibbard, R. L., Liou, L. W., Norton, M. A., and Perfect, S. A., *Modeling of Frequency Doubling and Tripling with Converter Crystal Refractive Index Spatial Non-Uniformities*, Lawrence Livermore National Laboratory, Livermore, CA, UCRL-JC-130030 ABS. Prepared for *Solid State Lasers for Applications (SSLA) to Inertial Confinement Fusion (ICF) 3rd Annual Intl Conf*, Monterey, CA Jun 7, 1998.

B

Back, C. A., Landen, O. L., Lee, R. W., Libby, S. B., and Woolsey, N. C., *Implosions: an Experimental Testbed for High Energy Density Physics*, Lawrence Livermore National Laboratory, Livermore, CA, UCRL-JC-129715 ABS. Prepared for *2nd Intl Workshop on Laboratory Astrophysics with Intense Lasers*, Tucson, AZ, Mar 19, 1998.

Back, C. A., Landen. O. L., Lee, R. W., Libby, S. B., and Woolsey, N. C., *Atomic Processes in Inertial Fusion Plasmas*, Lawrence Livermore National Laboratory, Livermore, CA, UCRL-JC-129714 ABS. Prepared for *11th American Physical Society Topical Conf on Atomic Processes in Plasmas*, Auburn, AL, Mar 22, 1998.

Bailey, D. S., Alley, W. E., and London, R. A., *Hard Tissue Ablation Simulations Using the LATIS Computer Code*, Lawrence Livermore National Laboratory, Livermore, CA, UCRL-JC-130048. Prepared for *Intl Symp on BIOS '98 Intl Biomedical Symp*, San Jose, CA, Jan 24, 1998.

Baldis, H. A., Labaune, C., Moody, J. D., Jalinaud, T., and Tikhonchuk, V. T., *Localization of Stimulated Brillouin Scattering in Random Phase Plate Speckles*, Lawrence Livermore National Laboratory, Livermore, CA, UCRL-JC-128618; *Phys. Rev. Lett.* **80**(9), 1900–1903 (1998).

Berger, R. L., Hinkel, D. E., Key, M. H., Kruer, W. L., Langdon, A. B., Lasinski, B. F., MacGowan, B. J., Rothenberg, J., Still, C. H., and Williams, E. A., *Particle and Fluid Simulations of Relativistic Channeling, Hole Boring, and the Interplay among Stimulated Raman and Brillouin Backscattering and Filamentation Instabilities*, Lawrence Livermore National Laboratory, Livermore, CA, UCRL-JC-130050 ABS. Prepared for *25th European Conf on Laser Interaction with Matter*, Formia, Italy, May 4, 1998.

Berger, R. L., Langdon, A. B., Still, C. H., and Williams, E. A., *On the Dominant and Subdominant Behavior of Stimulated Raman and Brillouin Scattering Driven by Nonuniform Laser Beams*, Lawrence Livermore National Laboratory, Livermore, CA, UCRL-JC-129673. Submitted to *Phys. Plasmas*.

Bodner, S. E., Colombant, D. G., Gardner, J. H., Lehmberg, R. H., McCrory, R. L., Obenschain, S. P., Phillips, L. S., Schmitt, A. J., Seka, W., and Sethian, J. D., *Direct-Drive Laser Fusion: Status and Prospects*, Lawrence Livermore National Laboratory, Livermore, CA, UCRL-ID-129418 Rev l-D.

Bodner, S. E., Gardner, J. H., Lehmberg, R. H., McCrory, R. L., Obenschain, S. P., Phillips, L. S., Schmitt, A. J., Seka, W., Sethain, J. D., Verdon, C. P., *Direct-Drive Laser Fusion: Status and Prospects*, Lawrence Livermore National Laboratory, Livermore, CA, UCRL-ID-129418.

Boley, C. D., and Estabrook, K. G., *Modeling of Laser Knife-Edge and Pinhole Experiments*, Lawrence Livermore National Laboratory, Livermore, CA, UCRL-JC-129613 ABS. Prepared for *Solid State Lasers for Application (SSLA) to Inertial Confinement Fusion (ICF) 3rd Annual Intl Conf*, Monterey, CA, Jun 7, 1998.

Britten, J. A., and Summers, L. J., *Multiscale, Multifunction Diffractive Structures Wet-Etched into Fused Silica for High-Laser Damage Applications*, Lawrence Livermore National Laboratory, Livermore, CA, UCRL-JC-130115. Submitted to *Opt. Lett*.

Budil, K. S., Bach, D. R., Klein, R. I., and Perry, T. S., *Experimental Investigation of the Shock-Cloud Interaction*, Lawrence Livermore National Laboratory, Livermore, CA, UCRL-JC-129511 ABS. Prepared for *1998 Joint American Physical Society/American Association of Physics Teachers Mtg*, Columbus, OH, Apr 18, 1998.

Budil, K. S., Bell, P. M., Brown, C., Estabrook, K., Gold, D. M., Key, M., Kock, J. A., Lerche, R., Pennington, D. M., and Remington, B. A., *Blast Wave Breakout Diagnostic for the Petawatt Laser System*, Lawrence Livermore National Laboratory, Livermore, CA, UCRL-JC-129852 ABS. Prepared for *12th Topical Conf on High-Temperature Plasma Diagnostics*, Princeton, NJ, Jun 7, 1998.

Budil, K. S., Bell, P. M., Brown, C., Estabrook, K., Gold, D. M., Key, M., Kock, J. A., Lerche, R., Pennington, D., and Remington, B. A., *Diagnosis of a Blast Wave Launched by the Petawatt Laser System*, Lawrence Livermore National Laboratory, Livermore, CA, UCRL-JC-130177 ABS. Prepared for *2nd Intl Workshop on Laboratory Astrophysics with Intense Lasers*, Tucson, AZ, Mar 19, 1998.

Budil, K. S., Farley, D. R., Murray, S., Perry, T. S., Peyser, T. A., Remington, B. A., and Weber, S. V., *Nonlinear Hydrodynamic Instability Experiments at Nova*, Lawrence Livermore National Laboratory, Livermore, CA, UCRL-JC-129305 ABS. Prepared for *Joint Operations Weapons Operations Group-37*, Los Alamos, NM, Feb 2, 1998.

Budil, K. S., Perry, T. S., Remington, B. A., Stry, P. E., and Wan, A. S., *Ablation Instability Experiments at Nova*, Lawrence Livermore National Laboratory, Livermore, CA, UCRL-JC-128012 ABS Rev. Prepared for *Joint Operations Weapons Operations Group-37*, Los Alamos, NM, Feb 2, 1998.

Burkhart, S. C., Brading, K. R., Feru, P. M., Kozlowski, M. R., Murray, J. E., Rothenberg, J. E., Van Wonterghem, B. M., Wegner, P. J., and Weiland, T. L., *High-Fluence and High-Power 1.05 µm and 351 nm Performance Experiments on Beamlet*, Lawrence Livermore National Laboratory, Livermore, CA, UCRL-JC-129865 ABS. Prepared for *Solid State Lasers for Application (SSLA) to Inertial Confinement Fusion (ICF) 3rd Annual Intl Conf*, Monterey, CA, Jun 7, 1998.

Burmann, J., Letts, S., and Saculla, M., *One Piece Capsule/Fill Tube Assemblies*, Lawrence Livermore National Laboratory, Livermore, CA, UCRL-JC-129956 ABS. Prepared for *Target Fabrication Mtg '98*, Jackson Hole, WY, Apr 19, 1998.

Burnham, A. K., Curren, D., Genin, F., Gerassimenko, M., Hibbard, W., Latkowski, J., Peterson, P., Scott, J., Tokheim, B., and Whitman, P., *Constraints on Target Chamber First Wall and Target Designs That Will Enable NIF Debris Shields to Survive*, Lawrence Livermore National Laboratory, Livermore, CA, UCRL-JC-129707 ABS. Prepared for *Solid State Lasers for Application (SSLA) to Inertial Confinement Fusion (ICF) 3rd Annual Intl Conf*, Monterey, CA, Jun 7, 1998.

C

Caird, J. A., Anderson, A. T., Hermes, G. L., Landen, O. L., Murray, J. E., Narduzzi, J. M., Norton, M. A., Orth, C. D., Seppala, L. G., and Sommer, S. C., *Z-Backlighter, a Laser X-Ray Diagnostic for High Energy Density Physics in Matter*, Lawrence Livermore National Laboratory, Livermore, CA, UCRL-JC-130043 ABS. Prepared for *Solid State Lasers for Application (SSLA) to Inertial Confinement Fusion (ICF) 3rd Annual Intl Conf*, Monterey, CA, Jun 7, 1998.

Caird, J., Adams, R., Anderson, A., Behrendt, B., Dawson, E., Edwards, G., Hermes, G., Ives, H., Murray, J., and Norton, M., *Z-Accelerator Laser Backlighter Conceptual Design Report*, Lawrence Livermore National Laboratory, Livermore, CA, UCRL-ID-129722-DR.

Camp, D. W., Britten, J., Kiikka, C., Kozlowski, M., Sheehan, L., Thomas, I., and Weinland, S., *Effect of Subsurface Damage on Fused Silica Laser Damage*, Lawrence Livermore National Laboratory, Livermore, CA, UCRL-JC-128368 ABS. Prepared for *Annual Symp on Optical Material for High Power Lasers*, Boulder, CO, Oct 6, 1997.

Campbell, J. H., Ficini-Dorn, G., Hawley-Fedder, R., McLean, M. J., and Suratwala, T. I., *Progress on Development of Continuous Glass Melting for Production of Laser Glass Needed for the NIF and LMJ*, Lawrence Livermore National Laboratory, Livermore, CA, UCRL-JC-129804 ABS. Prepared for *Solid State Lasers for Application (SSLA) to Inertial Confinement Fusion (ICF) 3rd Annual Intl Conf*, Monterey, CA, Jun 7, 1998.

Campbell, J. H., Kimmons, J. F., and Schwartz, S., *Platinum Particle Detection in Phosphate Laser Glasses*, Lawrence Livermore National Laboratory, Livermore, CA, UCRL-JC-130306. Submitted to *Analysis of Composition and Structure of Glass and Glass Ceramics*, Volume 7.

Cauble, R., Perry, T. S., Bach, D. R., Budil, K. S., Hammel, B. A., Collins, G. W., Gold, D. M., Dunn, J., Celliers, P., Da Silva, L. B., Foord, M. E., Wallace, R. J., Stewart, R. E., and Woolsey, N. C., "Absolute Equation-of-State Data in the 10–40 Mbar (1–4 TPa) Regime," *Phys. Rev. Lett*. **80**(6), 1248–1251 (1998).

Chang, J. J., Bass, I. L., Cochran, C. W., Dragon, E. P., and Ebbers, C. A., *Efficient Diode-Pumped Nd:YAG Laser with 451 W of CW IR and 182 W of Pulsed Green Output*, Lawrence Livermore National Laboratory, Livermore, CA, UCRL-JC-129421 ABS&SUM. Prepared for *Advanced Solid-State Lasers 13th Topical Mtg*, Coeur d'Alene, ID, Feb 2, 1998.

Chrien, R. E., Hoffman, N. M., Colvin, J. D., Keane, C. J., Landen, O. L., and Hammel, B. A., "Fusion Neutrons from the Gas-Pusher Interface in Deuterated-Shell Inertial Confinement Fusion Implosions," *Phys. Plasmas* **5**(3), 768–774 (1998).

Cohen, B. I., Baldis, H. A., Labaune, C., Langdon, A. B., Lasinski, B. F., and Williams, E. A., *Suppression of Stimulated Brillouin Scattering by Seeded Ion Wave Mode Coupling*, Lawrence Livermore National Laboratory, Livermore, CA, UCRL-JC-129490. Submitted to *Phys. of Plasmas.*

Cohen, B. I., Estabrook, K. G., Kirkwood, R. K., Langdon, A. B., Lasinski, B. F., Wharton, K. B., and Williams, E. A., *Resonant Stimulated Brillouin Interaction of Opposed Laser Beams in a Drifting Plasma*, Lawrence Livermore National Laboratory, Livermore, CA, UCRL-JC-129491. Submitted to *Phys. of Plasmas.*

Collins, G. W., Bernat, T. P., Bittner, D. N., Letts, S., Moll, G., Monsler, E., Sater, J. D., and Stevens, R., *Forming and Smoothing D_2 and HD Layers for ICF by Infra-Red Heating*, Lawrence Livermore National Laboratory, Livermore, CA, UCRL-JC-124255 ABS Rev. Prepared for *Target Fabrication Mtg '98*, Jackson Hole, WY, Apr 19, 1998.

Collins, G. W., Bernat, T., Bittner, D., Sanchez, J. J., and Sater, J. D., *Forming Uniform DT and D_2 Layers for Cryogenic NIF Targets*, Lawrence Livermore National Laboratory, Livermore, CA, UCRL-JC-129969 ABS. Prepared for *25th European Conf on Laser Interaction with Matter*, Formia, Italy, May 4, 1998.

Collins, G. W., Budil, K. S., Cauble, R., Celliers, P., Da Silva, L. B., Foord, M., Gold, D., Holmes, N. C., Ross, M., and Stewart, R.., *Pressure, Density, Temperature, and Reflectivity Measurements of Deuterium up to 3 Mbar on the Principle Hugoniot*, Lawrence Livermore National Laboratory, Livermore, CA, UCRL-JC-129967 ABS. Prepared for *2nd Intl Workshop on Laboratory Astrophysics with Intense Lasers*, Tucson, AZ, Mar 19, 1998.

Collins, G. W., Budil, K. S., Cauble, R., Celliers, P., Da Silva, L. B., Foord, M., Gold, D., Holmes, N. C., Ross, M., and Stewart, R., *Equation of State Measurements of Deuterium up to 3 Mbar*, Lawrence Livermore National Laboratory, Livermore, CA, UCRL-JC-129968 ABS. Prepared for *25th European Conf on Laser Interaction with Matter*, Formia, Italy, May 4, 1998.

Cook, R., Fearon, E., McEachern, R. L., and Stephens, R. B., *Representative Surface Profile Power Spectra from Capsules Used in Nova and Omega Implosion Experiments*, Lawrence Livermore National Laboratory, Livermore, CA, UCRL-JC-129961 ABS. Prepared for *Target Fabrication Mtg '98*, Jackson Hole, WY, Apr 19, 1998.

Crane, J. K., Browning, D., Dane, C. B., Henesian, M., Hopps, N. W., Martinez, M. D., Moran, B., Penko, F., Rothenberg, J. E., and Wilcox, R. B., *Integrated Operations of the National Ignition Facility (NIF) Optical Pulse Generation Development System*, Lawrence Livermore National Laboratory, Livermore, CA, UCRL-JC-129871 ABS. Prepared for *Solid State Lasers for Application (SSLA) to Inertial Confinement Fusion (ICF) 3rd Annual Intl Conf*, Monterey, CA, Jun 7, 1998.

D

Decker, C. D., and London, R. A., *Designs for a Compact Ni-Like-Tungsten X-Ray Laser*, Lawrence Livermore National Laboratory, Livermore, CA, UCRL-JC-126334; *Phys. Rev. A* **57** (2), 1395–1399 (1998).

Decker, D., Knopp, C., and Thompson, C., *Optics Damage Inspection for the NIF*, Lawrence Livermore National Laboratory, Livermore, CA, UCRL-JC-130034 ABS. Prepared for *Solid State Lasers for Application (SSLA) to Inertial Confinement Fusion (ICF) 3rd Annual Intl Conf, Monterey*, CA, Jun 7, 1998.

Dittrich, T. R., Bradley, P. A., Haan, S. W., Marinak, M. M., McEachern, R. L., Pollaine, S. M., Varnum, W. S., and Wilson, D. C., *Capsule Design for the National Ignition Facility*, Lawrence Livermore National Laboratory, Livermore, CA, UCRL-JC-130102 ABS. Prepared for *25th European Conf on Laser Interaction with Matter*, Formia, Italy, May 4, 1998.

Dittrich, T. R., Haan, S. W., Marinak, M. M., McEachern, R., and Pollaine, S. M., *Reduced Scale NIF Capsule Design*, Lawrence Livermore National Laboratory, Livermore, CA, UCRL-JC-130134. Submitted to *Physics of Plasmas*.

Dixit, S. N., and Sanchez, J., *Color Separation Grating Designs for the National Ignition Facility*, Lawrence Livermore National Laboratory, Livermore, CA, UCRL-JC-129815 ABS. Prepared for *Solid State Lasers for Application (SSLA) to Inertial Confinement Fusion (ICF) 3rd Annual Intl Conf*, Monterey, CA, Jun 7, 1998.

Dixit, S. N., Auyang, L., Britten, J., Parham, T., Rushford, M., and Summers, L., *Fabrication of Large Aperture Color Separation Grating for Beamlet Laser*, Lawrence Livermore National Laboratory, Livermore, CA, UCRL-JC-129816 ABS. Prepared for *Solid State Lasers for Application (SSLA) to Inertial Confinement Fusion 3rd Annual Intl Conf*, Monterey, CA, Jun 7, 1998.

E

Everett, M. J., Schoenenberger, K., Colston, Jr., B. W., and Da Silva, L. B., *Birefringence Characterization of Biological Tissue by Use of Optical Coherence Tomography*, Lawrence Livermore National Laboratory, Livermore, CA, UCRL-JC-128617; *Optics Lett.* **23**(3), 228–230 (1998).

F

Farmer, J. C., Erlandson, A., Gregg, H., Honea, E., Marshall, C., Parham, T., Payne, S., Pedrotti, L., Siekhaus, W., and Thomas. N., *Atmospheric Corrosion of Silver Flashlamp Reflectors in the National Ignition Facility*, Lawrence Livermore National Laboratory, Livermore, CA, UCRL-ID-128775.

Fernandez, A., and Phillion, D. W., "Effects of Phase Shifts on Four-Beam Interference Patterns," *Appl. Optics* **37**(3), 474–478 (1998).

G

Gerassimenko, M., Burnham, A., *Studies of First Wall Contamination and Mobilization of Contaminants*, Lawrence Livermore National Laboratory, Livermore, CA, UCRL-ID-129975.

Glendinning, S. G., Amendt, P., Cline, B. D., Ehrlich, R. B., Hammel, B. A., Kalantar, D. H., Landen, O. L., Richard, A., Wallace, R. J., and Weiland, T. J., *Hohlraum Symmetry Measurements with Surrogate Solid Targets*, Lawrence Livermore National Laboratory, Livermore, CA, UCRL-JC-129773 ABS. Prepared for *12th Topical Conf of High-Temperature Plasma Diagnostics*, Princeton, NJ, Jun 7, 1998.

Glendinning, S. G., Dixit, S. N., Hammel, B. A., Kalantar, D. H., Key, M. H., Kilkenny, J. D., Knauer, J. P., Pennington, D. M., Remington, B. A., Rothenberg, J., Wallace, R. J., and Weber, S. V., *Comparison of Drive-Seeded Modulations in Planar Foils for 0.35- and 0.53-µm Laser Drive*, Lawrence Livermore National Laboratory, Livermore, CA, UCRL-JC-127617; *Phys. Rev. Lett.* **80**(9), 1904–1907 (1998).

Glenzer, S. H., Back, C. A., Estabrook, K. G., Kirkwood, R. K., Lee, R. W., MacGowan, B. J., Moody, J. D., Suter, L. J., and Weiland, T. W., *Benchmarking X-Ray Spectroscopic Temperature Measurements from Fusion Plasmas with Thomson Scattering*, Lawrence Livermore National Laboratory, Livermore, CA, UCRL-JC-129508 ABS. Prepared for *14th Intl Conf on Spectral Line Shapes, State College*, PA, Jun 22, 1998.

Glenzer, S. H., Blain, M. A., Dixit, S. N., Estabrook, K. G., Hammel, B. A., Kauffman, R. L., Kirkwood, R. K., MacGowan, B. J., Suter, L. J., and Turner, R. E., *Hohlraum Energetics with Smoothed Laser Beams*, Lawrence Livermore National Laboratory, Livermore, CA, UCRL-JC-129862 ABS. Prepared for *25th European Conf on Lasers with Matter*, Formia, Italy, May 4, 1998.

Glenzer, S. H., Bower, J., MacGowan, B. J., MacKinnon, A. J., and Weiland, T. L., *High-Energy 4ω Probe Laser for Laser-Plasma Experiments at Nova*, Lawrence Livermore National Laboratory, Livermore, CA, UCRL-JC-129603 ABS. Prepared for *12th Intl Conf on High Temperature Plasma Diagnostics*, Princeton, NJ, Jun 7, 1998.

Glenzer, S. H., Suter, L. J., Turner, R. E., MacGowan, B. J., Estabrook, K. G., Bain, M. A., Dixit, S. N., Hammel, B. A., Kauffman, R. L., Kirkwood, R. K., Landen, O. L., Monteil, M.-C., Moody, J. D., Orzechowski, T. J., Pennington, D. M., Stone, G. F., and Weiland, T. L., *Energetics of Inertial Confinement Fusion Hohlraum Plasmas*, Lawrence Livermore National Laboratory, Livermore, CA, UCRL-JC-129236; *Phys. Rev. Lett.* **80**(13), 2845–2848 (1998).

Gold, D. M., Budil, K. S., Cauble, R., Celliers, P., Collins, G. W., Da Silva, L. B., Foord, M. E., Stewart, R. E., and Wallace, R. J., *Interferometric Laser Probe Diagnostic for High-Pressure, Shock-Driven Experiments at Nova*, Lawrence Livermore National Laboratory, Livermore, CA, UCRL-JC-129851 ABS. Prepared for *12th Topical Conf on High-Temperature Plasma Diagnostics*, Princeton, NJ, Jun 7, 1998.

Gresho, P. M., and Cook, R., *Some Aspects of the Hydrodynamics of the Microencapsulation Route to NIF Mandrels*, Lawrence Livermore National Laboratory, Livermore, CA, UCRL-JC-129963 ABS. Prepared for *Target Fabrication Mtg '98*, Jackson Hole, WY, Apr 19, 1998.

H

Haan, S. W., Dittrich, T. R., Marinak, M. M., Varnum, W. S., and Wilson, D. C., *NIF Ignition Target Specifications and Requirements*, Lawrence Livermore National Laboratory, Livermore, CA, UCRL-JC-129866 ABS. Prepared for *Target Fabrication Mtg 1998*, Jackson Hole, WY, Apr 19, 1998.

Hamilton, K. E., Buckley S. R., and Cook, R. R., *NIF Science of NIF Scale Capsule Development (Activities for FY'97)*, Lawrence Livermore National Laboratory, Livermore, CA, UCRL-ID-129331.

Henesian, M., Crane, J. K., Dane, B., Davin, J., Kott, L., Laumann, C., Lawson, J., Martinez, M., Miller, J., and Moran, B., *Diffraction Modeling of the National Ignition Facility (NIF) Optical Pulse Generation (OPG) System and Integration into the End-to-End System Model*, Lawrence Livermore National Laboratory, Livermore, CA, UCRL-JC-130041 ABS. Prepared for *Solid State Lasers for Application (SSLA) to Inertial Confinement Fusion (ICF) 3rd Annual Intl Conf*, Monterey, CA, Jun 7, 1998.

Hinkel, D. E., Berger, R. L., Langdon, A. B., Lasinski, B. F., Still, C. H., and Williams, E. A., *Numerical Simulations of Stimulated Brillouin Backscatter in the Presence of Transverse Plasma Flow*, Lawrence Livermore National Laboratory, Livermore, CA, UCRL-JC-129320 ABS. Prepared for *16th Intl Conf on the Numerical Simulation of Plasmas*, Santa Barbara, CA, Feb 9, 1998.

I

Isakov, A. I., Lebedev Physical Institut, *The* Project *Progress Report*, Lawrence Livermore National Laboratory, Livermore, CA, UCRL-CR-129411.

K

Kalantar, D. H., Amendt, P., Cable, M. D., Cline, B. D., Decker, C., Ehrlich, R. B., Glendinning, S. G., Hammel, B. A., Kilkenny, J. D., and Landen, O. L., *Time-Dependent Indirect-Drive Symmetry Control on the Nova and Omega Laser Facilities*, Lawrence Livermore National Laboratory, Livermore, CA, UCRL-JC-130109 ABS. Prepared for *25th European Conf on Laser Interaction with Matter*, Formia, Italy, May 4, 1998.

Kalantar, D. H., Chandler, E. A., Colvin, J. D., Failor, B. H., Hauer, A., Lee, R., Remington, B. A., Wark, J. S., Weber, S. V., and Wiley, L G., *Transient X-Ray Diffraction Used to Diagnose Shock Compressed Si Crystals on the Nova Laser*, Lawrence Livermore National Laboratory, Livermore, CA, UCRL-JC-129861 ABS. Prepared for *12th Topical Conf on High-Temperature Plasma Diagnostics*, Princeton, NJ, Jun 7, 1998.

Kalantar, D. H., Chandler, E. A., Colvin, J. D., Failor, B., Hauer, A., Meyers, M. A., Remington, B. A., Wark, J. S., Weber, S. V., and Wiley, L. G., *Transient X-Ray Diffraction Used to Diagnose Shock Compressed Si Crystals on the Nova Laser*, Lawrence Livermore National Laboratory, Livermore, CA, UCRL-JC-129861 ABS Rev. Prepared for *25th European Conf on Laser Interaction with Matter*, Formia, Italy, May 4, 1998.

Kalantar, D. H., Chandler, E. A., Colvin, J. D., Hauer, A. A., Meyers, M. A., Remington, B. A., Wark, J. S., Weber, S. V., and Wiley, L. G., *High Pressure Solid State Experiments on the Nova Laser*, Lawrence Livermore National Laboratory, Livermore, CA, UCRL-JC-129810 ABS. Prepared for *1998 Hypervelocity Impact Symp*, Huntsville, AL, Nov 16, 1998.

Kalantar, D. H., Chandler, E. A., Colvin, J. D., Remington, B. A., Weber, S. V., and Wiley, L. G., *X-Ray Driven Solid State Hydrodynamic Instability Experiments on the Nova Laser*, Lawrence Livermore National Laboratory, Livermore, CA, UCRL-JC-130110 ABS. Prepared for *25th European Conf on Laser Interaction with Matter*, Formia, Italy, May 4, 1998.

Kania, D. R., Be1l, P., and Trebes, J. E., *The Application of Photoconductive Detectors to the Measurement of X-Ray Production in Laser Produced Plasmas*, Lawrence Livermore National Laboratory, Livermore, CA, UCRL-JC-96269 ABS. Prepared for *Society of Photo-Optical Instrumentation, Technical Symp*, San Diego, CA, Aug 16–21, 1987.

Kauffman, R. L., Dixit, S. N., Glendinning, S. G., Glenzer, S. H., Kirkwood, R. K., Landen, O. L., MacGowan, B. J., Moody, J. D., Orzechowski, T. J., and Powers, L. V., *Improved Gas-Filled Hohlraum Performance on Nova with Beam Smoothing*, Lawrence Livermore National Laboratory, Livermore, CA, UCRL-JC-128004 Rev 1. Submitted to *Phys. of Plasmas*.

Key, M. H., Cable, M. D., Cowan, T. E., Estabrook, K. G., Hamel, B. A., Hatchett, S. P., Henry, D. E., Henry, E. A., Hinkel, D. E., and Kilkenny, J. D., *Atomic and Nuclear Processes Produced in Ultra-Intensity Laser Irradiation of Solid Targets*, Lawrence Livermore National Laboratory, Livermore, CA, UCRL-JC-129974 ABS. Prepared for *11th American Physical Society Topical Conf on Atomic Processes in Plasmas*, Auburn, AL, Mar 22, 1998.

Kilkenny, J. D., Bernat, T. P., Hammel, B. A., Lindl, J. D., Paisner, J. A., and Powell, H. T., *Update on the LLNL Activities to Achieve Ignition on the National Ignition Facility*, Lawrence Livermore National Laboratory, Livermore, CA, UCRL-JC-130139 ABS. Prepared for *25th European Conf on Laser Interaction with Matter*, Formia, Italy, May 4, 1998.

Kilkenny, J. D., Lindl, J. D., Paisner, J. A., and Powell, H. T., *Laser-Driven Thermonuclear Ignition*, Lawrence Livermore National Laboratory, Livermore, CA, UCRL-JC-130311 ABS. Prepared for *Royal Society Discussion Mtg*, London, England, Jul 15, 1998.

Kirkwood, R. K., Berger, R. L., Dague, N. A., Decker, C., Estabrook, K. G., Glenzer, S. H., MacGowan, B. J., Moody, J. D., Wharton, K. B., and Williams, E. A., *Scaling of Saturated Stimulated Raman Scattering in Large Scale Plasmas*, Lawrence Livermore National Laboratory, Livermore, CA, UCRL-JC-129857 ABS. Prepared for *25th European Conf on Laser Interaction with Matter*, Formia, Italy, May 4, 1998.

Koch, J. A., Back, C. A., Brown, C., Estabrook, K., Hammel, B. A., Hatchett, S. P., Key, M. H., Kilkenny, J. D., Landen, O. L., Lee, R. W., Moody, J. D., Offenberger, A. A., Pennington, D., Perry, M. D., Tabak, M., Yanovsky, V., Wallace, R. J., Wharton, K. B., and Wilks, S. C., *Time-Resolved X-Ray Spectroscopy of Deeply Buried Tracer Layers as a Density and Temperature Diagnostic for the Fast Ignitor*, Lawrence Livermore National Laboratory, Livermore, CA, UCRL-JC-126309; *Laser and Particle Beams* **16**(1), 225–232 (1998).

Koch, J. A., Barbee, T., Bennett, G., Brown, C., Celliers, P., Da Silva, L., Glendinning, S., Hammel, B., Landen, O., and Seely, J., *High-Energy High-Resolution X-Ray Imaging Applications and Techniques for the National Ignition Facility*, Lawrence Livermore National Laboratory, Livermore, CA, UCRL-JC-129869 ABS. Prepared for *12th Topical Conf on High-Temperature Plasma Diagnostics*, Princeton, NJ, Jun 7, 1998.

Kozioziemski, B. J., Bernat, T. P., and Collins, G. W., *D_2 Crystal Growth and Surface Energy*, Lawrence Livermore National Laboratory, Livermore, CA, UCRL-JC-130037 ABS. Prepared for *Target Fabrication Mtg '98*, Jackson Hole, WY, Apr 19, 1998.

Kozioziemski, B. J., Bernat, T. P., Collins, G. W., and Sater, J., *Helium Bubble Dynamics in D-T Layers*, Lawrence Livermore National Laboratory, Livermore, CA, UCRL-JC-130038 ABS. Prepared for *Target Fabrication Mtg '98*, Jackson Hole, WY, Apr 19, 1998.

Kozlowski, M. R., Campbell, J. H., Maricle, S., Mouser, R., Schwartz, S., Wegner, P., and Weiland, T., *3ω Damage Threshold Evaluation of Final Optics Components Using Beamlet Mule and Off-Line Testing*, Lawrence Livermore National Laboratory, Livermore, CA, UCRL-JC-129721 ABS. Prepared for *Solid State Lasers for Application (SSLA) to Inertial Confinement Fusion (ICF) 3rd Annual Intl Conf*, Monterey, CA, Jun 7, 1998.

L

Labaune, C., Baldis, H. A., Bauer, B. S., Tikhonchuk, V. T., and Laval, G., *Time-Resolved Measurements of Secondary Langmuir Waves Produced by the Langmuir Decay Instability in a Laser-Produced Plasma*, Lawrence Livermore National Laboratory, Livermore, CA, UCRL-JC-127432; *Phys. Plasmas* **5**(1), 234–242 (1998).

Landen, O. L., Amendt, P. A., Cable, M. D., Glendinning, S. G., Hammel, B. A., Kalantar, D. H., Kecker, C. D., Suter, L. J., Turner, R. E., and Wallace, R., *Time-Dependent, Indirect-Drive Symmetry Control on the Nova and Omega Laser Facilities*, Lawrence Livermore National Laboratory, Livermore, CA, UCRL-JC-130109 ABS Rev. Prepared for *17th Intl Atomic Energy Agency Fusion Energy Conf*, Yokohama, Japan, Oct 19, 1998.

Langdon, A. B., Berger, R., Dixit, S., Feit, M., Hendrix, J., Hinkel, D., Kirkwood, R., MacGowan, B., Manes, K., and Miller, J., *Significance of Stimulated Brillouin and Raman Backscatter from the Target as a Source for Optics Damage*, Lawrence Livermore National Laboratory, Livermore, CA, UCRL-JC-129765 ABS. Prepared for *Solid State Lasers for Application (SSLA) to Inertial Confinement Fusion (ICF) 3rd Annual Intl Conf*, Monterey, CA, Jun 7, 1998.

Lasinski, B. F., and Langdon, A. B., *PIC Simulations of Hole-Boring for Fast-Ignitor Applications*, Lawrence Livermore National Laboratory, Livermore, CA, UCRL-JC-129304 ABS. Prepared for *16th Intl Conf on the Numerical Simulation of Plasmas*, Santa Clara, CA, Feb 9, 1998.

Latkowski, J. F., and Sanchez, J. J., *Neutronics and Activation Analysis for the National Ignition Facility Cryogenic Target Positioner*, Lawrence Livermore National Laboratory, Livermore, CA, UCRL-JC-129954 ABS. Prepared for *Target Fabrication Mtg '98*, Jackson Hole, WY, Apr 19, 1998.

Latkowski, J. F., and Vujic, J. L., *Neutronics Issues and Inertial Fusion Energy: a Summary of Findings*, Lawrence Livermore National Laboratory, Livermore, CA, UCRL-JC-129625 ABS. Prepared for *13th Topical Mtg on the Technology of Fusion Energy*, Nashville, TN, Jun 7, 1998.

Lerche, R. A., and Ognibene, T. J., *Error Analysis for Fast Scintillator-Based ICF Burn History Measurements*, Lawrence Livermore National Laboratory, Livermore, CA, UCRL-JC-129701 ABS. Prepared for *12th Topical Conf on High-Temperature Plasma Diagnostics*, Princeton, NJ, Jun 7, 1998.

Lerche, R. A., Ellis, R. J., Lane, S. M., and Ress, D., *Neutron Penumbral Aperture Images of ICF Targets Achieve 60-µm Resolution*, Lawrence Livermore National Laboratory, Livermore, CA, UCRL-JC-129700 ABS. Prepared for *12th Topical Conf on High-Temperature Plasma Diagnostics*, Princeton, NJ, Jun 7, 1998.

Letts, S., Buckley, S., Burmann, J., Fearon, E., Roberts, C., and Saculla, M., *Physical Properties of Films Used in ICF Targets*, Lawrence Livermore National Laboratory, Livermore, CA, UCRL-JC-129957 ABS. Prepared for *Target Fabrication Mtg '98*, Jackson Hole, WY, Apr 19, 1998.

Letts, S., Buckley, S., Cook, R., Fearon, E., and Saculla, M., *New Approaches in the Preparation of Pα MS Beads as Mandrels for NIF-Scale Target Capsules*, Lawrence Livermore National Laboratory, Livermore, CA, UCRL-JC-129955 ABS. Prepared for *Target Fabrication Mtg '98*, Jackson Hole, WY, Apr 19, 1998.

Logan, B. G., Anderson, O., Ditmire, T., Kuehl, T., and Perry, M., *Highly-Charged Heavy-Ion Production with Short Pulse Lasers*, Lawrence Livermore National Laboratory, Livermore, CA, UCRL-JC-129617. Prepared for *High Power Laser Study Group Workshop*, Darmstadt, Germany, Jan 29, 1998.

London, R. A., Amendt, P. A., Bailey, D. S., Esch, V., and Visuri, S., *Scaling Model for Laser-Produced Bubbles in Soft Tissue*, Lawrence Livermore National Laboratory, Livermore, CA, UCRL-JC-128034. Prepared for *Intl Symp on BiOS '98 Intl Biomedical Optics Symp*, San Jose, CA, Jan 24, 1998.

M

Marinak, M. M., Dittrich, T. R., Haan, S. W., Tipton, R. E., and Zimmerman, G. B., *Comparison of Three-Dimensional Multimode Hydrodynamic Instability Growth on Various National Ignition Facility Capsule Designs with HYDRA Simulations*, Lawrence Livermore National Laboratory, Livermore, CA, UCRL-JC-128862 Rev 1. Submitted to *Phys. of Plasmas.*

Martinez, M. D., Braucht, J., Browning, D., Crawford, J., Deadrick, F. J., Hawkins, S., Jones, B., Skulina, K. M., Tilley, R., and Wing, R., *High Gain Preamplifier Module (PAM) Engineering Prototype for the National Ignition Facility (NIF) Laser System*, Lawrence Livermore National Laboratory, Livermore, CA, UCRL-JC-129872 ABS. Prepared for *Solid State Lasers for Application (SSLA) to Inertial Confinement Fusion (ICF) 3rd Annual Intl Conf*, Monterey, CA, Jun 7, 1998.

Milam, D., Afeyan, B. B., Boley, C. D., Estabrook, K. G., Kirkwood, R. K., Murray, J. E., Nielsen, N. D., Sell, W. D., and Zakharenkov, Y. A., *Pinhole Closure Measurements*, Lawrence Livermore National Laboratory, Livermore, CA, UCRL-JC-129864 ABS. Prepared for *Solid State Lasers for Application (SSLA) to Inertial Confinement Fusion (ICF) 3rd Annual Intl Conf*, Monterey, CA, Jun 7, 1998.

Miller, D. A., and Tabak, M., *Distributed Radiator, Heavy Ion Driven Inertial Confinement Fusion Target with Realistic, Multibeam Illumination Geometry*, Lawrence Livermore National Laboratory, Livermore, CA, UCRL-JC-130312 ABS. Prepared for *17th Intl Atomic Energy Agency Fusion Energy Conf*, Yokohama, Japan, Oct 19, 1998.

Moody, J. D., Afeyan, B. B., Glenzer, S. H., Kirkwood, R. K., Kruer, W. L., MacGowan, B. J., Montgomery, D. S., Schmitt, A. J., Stone, G. F., and Williams, E. A., *First Measurement of Near Forward Scattering from a Smoothed Laser in a Large ICF Plasma*, Lawrence Livermore National Laboratory, Livermore, CA, UCRL-JC-129510. Submitted to *Phys. Rev. Lett*.

Moody, J. D., Afeyan, B. B., Glenzer, S. H., Kirkwood, R. K., Kruer, W. L., MacGowan, B. J., Montgomery, D. S., Schmitt, A. J., Stone, G. F., and Williams, E. A., *Measurements of Near Forward Scattered Laser Light in a Large ICF Plasma*, Lawrence Livermore National Laboratory, Livermore, CA, UCRL-JC-129774 ABS. Prepared for *12th Topical Conf on High-Temperature Plasma Diagnostics*, Princeton, NJ, Jun 7, 1998.

Moody, J. D., Afeyan, B. B., Glenzer, S. H., Kirkwood, R. K., Kruer, W. L., MacGowan, B. J., Montgomery, D. S., Schmitt, A. J., Stone, G. F., and Williams, E. A., *Measurements of Near Forward Scattered Laser Light from a Smoothed Probe Beam in a Large ICF Plasma*, Lawrence Livermore National Laboratory, Livermore, CA, UCRL-JC-129858 ABS. Prepared for *25th European Conf on Laser Interaction with Matter*, Formia, Italy, May 4, 1998.

Mourou, G. A., Barty, C. P., and Perry, M. D., *Ultrahigh-Intensity Laser: Physics of the Extreme on a Tabletop*, Lawrence Livermore National Laboratory, Livermore, CA, UCRL-ID-128698; *Physics Today* **51**(1), 22–28 (1998).

Murray, J. E., and Milam, D., *Spatial Filter Issues*, Lawrence Livermore National Laboratory, Livermore, CA, UCRL-JC-129751 ABS. Prepared for *Solid State Lasers for Application (SSLA) to Inertial Confinement Fusion (ICF) 3rd Annual Intl Conf*, Monterey, CA, Jun 7, 1998.

N

Nikitenko, A. I., Cook, R. R., Tolokonnikov, S. M., *Recent Shell Formation Experiments with Upgraded Ballistic Furnace*, Lawrence Livermore National Laboratory, Livermore, CA, UCRL-JC-129960 ABS. Prepared for *Target Fabrication Mtg '98*, Jackson Hole, WY, Apr 19, 1998.

Nikitenko, A. I., Tolokonnikov, S. M., and Cook, R. C., "Large Shell Fabrication Results Using the Ballistic Furnace," *J. Moscow Phys. Soc.* **8**, 63–69 (1998).

Norton, M. A., Boley, C. D., Murray, J. E., Neeb, K., and Sinz, K., *Long-Lifetime Low-Contamination Metal Beam Dumps for NIF Spatial Filters*, Lawrence Livermore National Laboratory, Livermore, CA, UCRL-JC-129768 ABS. Prepared for *Solid State Lasers for Application (SSLA) to Inertial Confinement Fusion (ICF) 3rd Annual Intl Conf*, Monterey, CA, Jun 7, 1998.

P

Page, R. H., Schaffers, K. L., Waide, P. A., Tassano, J. B., Payne, S. A., Krupke, W. F., and Bischel, W. K., *Upconversion-Pumped Luminescence Efficiency of Rare-Earth-Doped Hosts Sensitized with Trivalent Ytterbium*, Lawrence Livermore National Laboratory, Livermore, CA, UCRL-JC-128099; *J. Opt. Soc. Am. B* **15**(3), 996–1008 (1998).

Pennington, D. M., Britten, J. A., Brown, C. G., Herman, S., Miller, J. L., Perry, M. D., Stuart, B. C., Tietbohl, G., and Yanovsky, V., *Petawatt Class Laser Irradiation System for Laser–Matter Interactions*, Lawrence Livermore National Laboratory, Livermore, CA, UCRL-JC-129808 ABS&SUM. Prepared for *Conf on Lasers and Electro-Optics/European Quantum Electronics Conf '98*, Glasgow, Scotland, UK, Sept 13, 1998.

Perry, M. D., Britten, J. A., Brown, C., Herman, S., Miller, J., Pennington, D. M., Powell, H. T., Stuart, B. C., Tietbohl, G., and Vergino, M., *Petawatt Laser Pulses*, Lawrence Livermore National Laboratory, Livermore, CA, UCRL-JC-129414. Submitted to *Opt. Lett.*

Perry, M. D., Britten, J., Brown, C., Herman, S., Miller, J., Pennington, D. M., Powell, H. T., Shore, B. W., Stuart, B. C., and Tietbohl, G., *Production of Petawatt Laser Pulses*, Lawrence Livermore National Laboratory, Livermore, CA, UCRL-JC-129760. Prepared for *Applications of High Field and Short-Wavelength Sources*, Santa Fe, NM , Mar 19, 1998.

Phillips, T. W., Cable, M. D., Cowan, T. E., Henry, E. A., Key, M. H., Perry, M. D., Sangster, T. C., and Stoyer, M. A., *Diagnosing Hot Electron Production by Short Pulse, High Intensity Lasers Using Photonuclear Reaction*, Lawrence Livermore National Laboratory, Livermore, CA, UCRL-JC-129813 ABS. Prepared for *12th Topical Conf on High-Temperature Plasma Diagnostics*, Princeton, NJ, Jun 7, 1998.

Pipes, J. W., and Sanchez, J. J., *Hohlraum Test Apparatus Modifications to Accommodate High Resolution Measurements on the Thermally Shimmed Hohlraum*, Lawrence Livermore National Laboratory, Livermore, CA, UCRL-JC-129953 ABS. Prepared for *Target Fabrication Mtg '98*, Jackson Hole, WY, Apr 19, 1998.

Pittenger, L. C., Latkowski, J., and Sanchez, J., *Considerations for the Preliminary Design of the NIF Target Insertion Cryostat*, Lawrence Livermore National Laboratory, Livermore, CA, UCRI-JC-130135 ABS. Prepared for *Target Fabrication Mtg '98*, Jackson Hole, WY, Apr 19, 1998.

R

Remington, B. A., Arnett, D., Budil, K. S., Drake, R. P., Estabrook, K., Glendinning, S., Gold, D., Kane, J., Ryutov, D., and Smith, T., *Astrophysically Relevant Hydrodynamics Experiments Using Intense Lasers*, Lawrence Livermore National Laboratory, Livermore, CA, UCRL-JC-129512 ABS. Prepared for *1998 Joint American Physical Society/American Association of Physics Teachers Mtg*, Columbus, OH, Apr 18, 1998.

Remington, B. A., Arnett, D., Budil, K. S., Drake, R. P., Estabrook, K., Glendinning, S. G., Gold, D., Kane, J., Ryutov, D., and Smith, T., *Astrophysically Relevant Hydrodynamics Experiments Using Intense Lasers*, Lawrence Livermore National Laboratory, Livermore, CA, UCRL-JC-129512 ABS Rev. Prepared for *25th European Conf on Laser Interaction with Matter*, Formia, Italy, May 4, 1998.

Roberts, C. C., Cook, R. C., Letts, S. A., and Saculla, M. D., *High Performance Polyimide Coating Technology FY97 Summary*, Lawrence Livermore National Laboratory, Livermore, CA, UCRL-ID-129313.

Roberts, C., Cook, R., Letts, S., and Saculla, M., *Science of Polyimide Film Deposition*, Lawrence Livermore National Laboratory, Livermore, CA, UCRL-JC-129962 ABS. Prepared for *Target Fabrication Mtg '98*, Jackson Hole, WY, Apr 19, 1998.

Roberts, C., Letts, S., and Saculla, M., *Polyimide Coatings from AB Monomers*, Lawrence Livermore National Laboratory, Livermore, CA, UCRL-JC-129958 ABS. Prepared for *Target Fabrication Mtg '98*, Jackson Hole, WY, Apr 19, 1998.

Rotter, M., Erlandson, A., Jancaitis, K., Le Touze, G., Marshall, C., Seznec, S., and Zapata, L., *Pump-Induced Wavefront Distortion in Prototype NIF/LMJ Amplifiers—Modeling and Comparison with Experiments*, Lawrence Livermore National Laboratory, Livermore, CA, UCRL-JC-130044 ABS. Prepared for *Solid State Lasers for Application (SSLA) to Inertial Confinement Fusion (ICF) 3rd Annual Intl Conf*, Monterey, CA, Jun 7, 1998.

Ryutov, D., and Toor, A., *Enhanced Thermal Dissipation and the Rayleigh–Taylor Instability in Emulsion-Like Media*, Lawrence Livermore National Laboratory, Livermore, CA, UCRL-JC-127007; *Phys. Plasmas* **5**(1), 22–35 (1998).

Ryutov, D., Drake, R. P., Kane, J., Liang, E., Remington, B., and Wood-Vasey, W. M., *Similarity Criteria for the Laboratory Simulations of Supernova 1987A Hydrodynamics*, Lawrence Livermore National Laboratory, Livermore, CA, UCRL-JC-129420. Submitted to *Astrophys. J.*

S

Saculla, M. D., Hsieh, E., Letts, S., Roberts, C., and Rogers, G., *Strength Measurements of Polyimide Coatings*, Lawrence Livermore National Laboratory, Livermore, CA, UCRL-JC-129964 ABS. Prepared for *Target Fabrication Mtg '98*, Jackson Hole, WY, Apr 19, 1998.

Sanchez, J. J., and Giedt, W. H., *Temperature Control Sensitivity Variation of Cylindrical Hohlraums with Capsule Thermal Conductivity*, Lawrence Livermore National Laboratory, Livermore, CA, UCRL-JC-130035 ABS. Prepared for *Target Fabrication Mtg '98*, Jackson Hole, WY, Apr 19, 1998.

Sanz, J., and Latkowski, J., *Activation Analysis of Target Debris in the National Ignition Facility*, Lawrence Livermore National Laboratory, Livermore, CA, UCRL-JC-129514 ABS. Prepared for *13th Topical Mtg on Fusion Energy*, Nashville, TN, Jun 7, 1998.

Sater, J. D., Collins, G. W., and Pipes, J., *Cryogenic D-T Fuel Layers Formed in 1 mm Spheres by Beta-Layering*, Lawrence Livermore National Laboratory, Livermore, CA, UCRL-JC-128031 ABS Rev. Prepared for *Target Fabrication Mtg '98*, Jackson Hole, WY, Apr 19, 1998.

Schwartz, S., Campbell, J. H., Kimmons, J. F., Kozlowski, M. R., Sheehan, L. M., and Stolz, C. J., *Vendor-Based Laser Damage Metrology Equipment Supporting the National Ignition Facility*, Lawrence Livermore National Laboratory, Livermore, CA, UCRL-JC-129719 ABS. Prepared for *Solid State Lasers for Application (SSLA) to Inertial Confinement Fusion (ICF) 3rd Annual Intl Conf*, Monterey, CA, Jun 7, 1998.

Sheehan, L. M., Battersby, C., Kozlowski, M., Maricle, S., and Mouser, R., *Inspection and Laser Induced Damage Diagnostics for Large Aperture Ultraviolet Optics*, Lawrence Livermore National Laboratory, Livermore, CA, UCRL-JC-129720 ABS. Prepared for *Solid State Lasers for Application (SSLA) to Inertial Confinement Fusion (ICF) 3rd Annual Intl Conf*, Monterey, CA, Jun 7, 1998.

Still, C. H., Berger, R. L., Cohen, B. I., Hinkel, D. E., Langdon, A. B., Lasinski, B. F., and Williams, E. A., *Extending Laser–Plasma Interaction Simulations with MPP-F3D*, Lawrence Livermore National Laboratory, Livermore, CA, UCRL-JC-129321 ABS. Prepared for *16th Intl Conf on the Numerical Simulation of Plasmas*, Santa Barbara, CA, Feb 9, 1998.

Stolz, C., Hue, J., Jennings, R. T., Kozlowski, M. R., Maricle, S. M., Schwartz, S., and Sheehan, L. M., *Laser Conditioning Methods of Hafnia Silica Multilayer Mirrors*, Lawrence Livermore National Laboratory, Livermore, CA, UCRL-JC-129318. Prepared for *Intl Society for Optical Engineering, High Power Lasers and Applications*, San Jose, CA, Jan 24, 1998.

Stowers, I. F., and Horvath, J. A., *Achieving and Maintaining Cleanliness in NIF Amplifiers*, Lawrence Livermore National Laboratory, Livermore, CA, UCRL-JC-130040 ABS. Prepared for *Solid State Lasers for Application (SSLA) to Inertial Confinement Fusion (ICF) 3rd Annual Intl Conf*, Monterey, CA, Jun 7, 1998.

Suratwala, T. I., Campbell, J. H., Steele, R. A., and Steene, W. A., *Fail-Safe Design for Square Vacuum-Barrier Windows*, Lawrence Livermore National Laboratory, Livermore, CA, UCRL-JC-129805 ABS. Prepared for *Solid State Lasers for Application (SSLA) to Inertial Confinement Fusion (ICF) 3rd Annual Intl Conf*, Monterey, CA, Jun 7, 1998.

T

Tabak, M., and Callahan–Miller, D., *Design of a Distributed Radiator Target for Inertial Fusion Driven from Two Sides with Heavy Ion Beams*, Lawrence Livermore National Laboratory, Livermore, CA, UCRL-JC-128366 Rev 4. Submitted to *Phys. of Plasmas*.

Tabak, M., and Callahan–Miller, D., *Design of a Distributed Radiator Target for Inertial Fusion Driven from Two Sides with Heavy Ion Beams*, Lawrence Livermore National Laboratory, Livermore, CA, UCRL-JC-128366 Rev 5. Prepared for *12th Intl Symp on Heavy Ion Fusion*, Heidelberg, Germany, Sept 24, 1997.

Takagi, M., Buckley, S., and Cook, R., *Recent Progress in the Area of Microencapsulation at LLNL*, Lawrence Livermore National Laboratory, Livermore, CA, UCRL-JC-129959 ABS. Prepared for *Target Fabrication Mtg '98*, Jackson Hole, WY, Apr 19, 1998.

Tokheim, R. E., Anderson, A. T., Burnham, A., Cooper, T., Courchinoux, R., Curran, D. R., Jequier, F., Schirmann, D., Scott, J. M., and Seaman, L., *Hypervelocity Shrapnel Damage Assessment in the NIF Target Chamber*, Lawrence Livermore National Laboratory, Livermore, CA, UCRL-JC-129516 ABS. Prepared for *1998 Hypervelocity Impact Symp*, Huntsville, AL, Nov 16, 1998.

Tokheim, R. E., Curran, D. R., and Seaman, L., *Damage and Hardening Assessments for the National Ignition Facility Target Chamber Design*, Lawrence Livermore National Laboratory, Livermore, CA, UCRL-CR-128686.

Trenholme, J., Auerbach, J., Henesian, M., Jancaitis, K., Lawson, J., Orth, C., and Sacks, R., *Integrated NIF Propagation Modeling Prop92 Simulation of the Integrated NIF Laser System for the ICF Mission*, Lawrence Livermore National Laboratory, Livermore, CA, UCRL-MA-129811.

Turner, R. E., Bell, P., Costa, R., Hargrove, D., and Landen, O L., *Comparison of Diamond Photoconductive Detectors with Vacuum Diodes on Nova for Fast Soft X-Ray Power Measurements*, Lawrence Livermore National Laboratory, Livermore, CA, UCRL-JC-129713 ABS. Prepared for *12th Topical Conf on High-Temperature Plasma Diagnostics*, Princeton, NJ, Jun 7, 1998.

U

Unites, W. G., Burmann, J., Cellier, P., Collins, G. W., Da Silva, L., Jones, R., and Pipes, J., *Cryogenic Cell Target for Equation of State Measurements in Deuterium*, Lawrence Livermore National Laboratory, Livermore, CA, UCRL-JC-129952 ABS. Prepared for *Target Fabrication Mtg '98*, Jackson Hole, WY, Apr 19, 1998.

W

Wegner, P. J., Auerbach, J. M., Barker, C. E., Couture, S. A., De Yoreo, J. J., Hibbard, R. L., Liou, L. W., Norton, M. A., Burkhart, S. C., and Whitman, P. A., *Frequency Converter Development for the National Ignition Facility*, Lawrence Livermore National Laboratory, Livermore, CA, UCRL-JC-129725 ABS. Prepared for *Solid State Lasers for Application (SSLA) to Inertial Confinement Fusion (ICF) 3rd Annual Intl Conf*, Monterey, CA, Feb 7, 1998.

Wegner, P. J., Henesian, M. A., Salmon, J. T., Van Wonterghem, B. M., Weiland, T. L., and Williams, W. H., *Wavefront and Divergence of the Beamlet Prototype Laser*, Lawrence Livermore National Laboratory, Livermore, CA, UCRL-JC-129724 ABS. Prepared for *Solid State Lasers for Application (SSLA) to Inertial Confinement Fusion (ICF) 3rd Annual Intl Conf*, Monterey, CA, Jun 7, 1998.

Wharton, K. B., Afeyan, B. B., Cohen, B. I., Estabrook, K. G., Glenzer, S. H., Joshi, C., Kirkwood, R. K., and Moody, J. D., *Observation of Energy Transfer between Identical-Frequency Laser Beams in a Flowing Plasma*, Lawrence Livermore National Laboratory, Livermore, CA, UCRL-JC-129856. Submitted to *Phys. Rev. Letters*.

Wharton, K. B., Afeyan, B. B., Cohen, B. I., Estabrook, K. G., Glenzer, S. H., Joshi, C., Kirkwood, R. K., and Moody, J. D., *Observation of Energy Transfer between Laser Beams in Flowing Plasmas*, Lawrence Livermore National Laboratory, Livermore, CA, UCRL-JC-129856 ABS. Prepared for *25th European Conf on Laser Interaction with Matter*, Formia, Italy, May 4, 1998.

Wharton, K. B., Afeyan, B. B., Cohen, B. I., Estabrook, K. G., Glenzer, S. H., Joshi, C., Kirkwood, R. K., and Moody, J. D., *Observation of Resonant Energy Transfer between Identical-Frequency Laser Beams*, Lawrence Livermore National Laboratory, Livermore, CA, UCRL-JC-130320 ABS. Prepared for *28th Annual Anomalous Absorption Conf*, Bar Harbor, ME, Jun 14, 1998.

Wharton, K. B., Brown, C., Hammel, B., Hatchett, S., Key, M., Moody, J., Offenberger, A., Perry, M., Wilks, S., and Yanovsky, V., *Laser–Plasma Interactions in the 100-TW Regime: Critical Density and Overdense Phenomena*, Lawrence Livermore National Laboratory, Livermore, CA, UCRL-JC-129324 ABS. Prepared for *1998 Joint American Physical Society/American Association of Physics Teachers Mtg*, Columbus, OH, Apr 18, 1998.

Whitman, P., Anderson, A., Bletzer, K., Burnham, A., Genin, F., Hibbard, W., Norton, M., and Scott, J., *Management of Unconverted Light for the National Ignition Facility Target Chamber*, Lawrence Livermore National Laboratory, Livermore, CA, UCRL-JC-129706 ABS. Prepared for *Solid State Lasers for Application (SSLA) to Inertial Confinement Fusion (ICF) 3rd Annual Intl Conf*, Monterey, CA, Jun 7, 1998.

Wilcox, R., Browning, D., Dreifuerst, G., Padilla, E., and Penko, F., *Development System Performance of the NIF Master Oscillator and Pulse Forming Network*, Lawrence Livermore National Laboratory, Livermore, CA, UCRL-JC-129870 ABS. Prepared for *Solid State Lasers for Application (SSLA) to Inertial Confinement Fusion (ICF) 3rd Annual Intl Conf*, Monterey, CA, Jun 7, 1998.

Wolfrum, E., Wark, J., Zhang, J., Kalantar, D., Key, M. H., Remington, B. A., Weber, S. V., Neely, D., Rose, S., Warwick, J., MacPhee, A., Lewis, C. L. S., Demir, A., Lin, J., Smith, R., and Tallents, G. J., "Measurement of Single Mode Imprint in Laser Ablative Drive of a Thin Al Foil by Extreme Ultraviolet Laser Radiography," *Phys. Plasmas* **5**(1), 227–233 (1998).

Wrubel, Th., Ahman, I., Buscher, S., Glenzer, S. H., and Kunze, H.-J., *Stark Broadening Along the Berylliumlike Sequence*, Lawrence Livermore National Laboratory, Livermore, CA, UCRL-JC-129509. Submitted to *Phys. Rev. E*.

Wu, Z. L., Salleo, A., Stolz, C. J., and Yoshiyama, J. M., *Characterization of Fluence Limiting Defects in Hafnia/Silica Multilayer Coatings Manufactured for the National Ignition Facility*, Lawrence Livermore National Laboratory, Livermore, CA, UCRL-JC-129756. Prepared for *Optical Interference Coatings Topical Mtg*, Tucson, AZ, Jun 7, 1998.

Y

Yan, M., Kozlowski, M., Mohideen, U., Siekhaus, W., Wang, L., and Yang, J., *Defect Study in Fused Silica Using Near Field Scanning Optical Microscopy*, Lawrence Livermore National Laboratory, Livermore, CA, UCRL-JC-129506. Prepared for *29th Annual Symp on Optical Materials for High Power Lasers*, Boulder, CO, Oct 6, 1997.

Z

Zaitseva, N., Atherton, J., Bell, W., Carmen, M. L., Couture, S., De Yoreo, J., DeHaven, M. R., James, L., Martin, M., and Robey, H., *Rapid Growth of Large KDP and DKDP Crystals: the Connection between Growth and Conditions, Size and Crystal Quality*, Lawrence Livermore National Laboratory, Livermore, CA, UCRL-JC-129709 ABS. Prepared for *Solid State Lasers for Application (SSLA) to Inertial Confinement Fusion (ICF) 3rd Annual Intl Conf*, Monterey, CA, Jun 7, 1998.

Zapata, L., Beuillier, J., Erlandson, A., Grebot, E., Guenet, J., Jancaitis, K., Marshall, C., Rotter, M., and Seznec, S., *Gain and Wavefront Measurements Performed on the NIF/LMJ Prototype Amplifiers*, Lawrence Livermore National Laboratory, Livermore, CA, UCRL-JC-130045 ABS. Prepared for *Solid State Lasers for Application (SSLA) to Inertial Confinement Fusion (ICF) 3rd Annual Intl Conf*, Monterey, CA, Jun 7, 1998.

Ze, F., Alvarez, S., Bell, P. M., Costa, R. L., Landen, O. L., Turner, R. E., and Tut, T., *Investigation of X-Ray Quantum Efficiencies in Multilayered Photocathodes for Micro Channel Plate (MCP) Applications*, Lawrence Livermore National Laboratory, Livermore, CA, UCRL-JC-129620 ABS. Prepared for *12th Topical Conf on High Temperature Plasma Diagnostics*, Princeton, NJ, Jun 7, 1998.

Zweiback, J., Ditmire, T., Komashko, A., Perry, M. D., and Rubenchik, A. M., *Experimental Observation of Resonance Effects in Intensely Irradiated Atomic Clusters*, Lawrence Livermore National Laboratory, Livermore, CA, UCRL-JC-129764 ABS&SUM. Prepared for *Ultrafast Phenomena '98*, Germany.

ICF/NIF/HEDES Program
Lawrence Livermore National Laboratory
P.O. Box 808, L-475
Livermore, California 94551

Address Correction Requested